Towards Ion Stopping Power Experiments with the Laser-Driven LIGHT Beamline

Auf dem Weg zu Energieverlustexperimenten mit der Lasergetriebenen LIGHT Beamline
Zur Erlangung des Grades eines Doktors der Naturwissenschaften (Dr. rer. nat.)
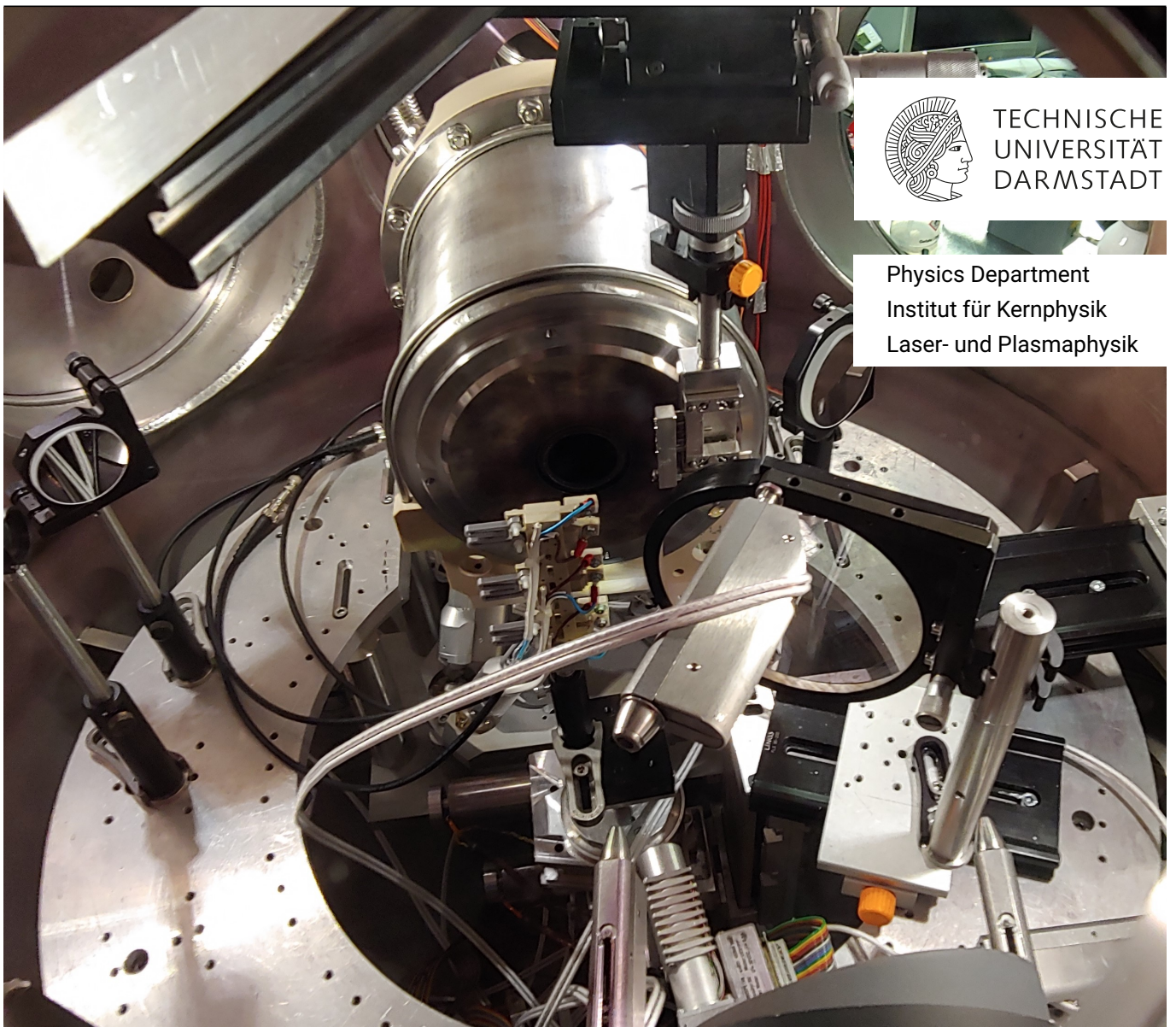Genehmigte Dissertation von Haress Nazary aus Seligenstadt
Tag der Einreichung: 13.05.2024, Tag der Prüfung: 10.07.2024

1. Gutachten: Prof. Dr. Markus Roth
2. Gutachten: Prof. Dr. Vincent Bagnoud
Darmstadt, Technische Universität Darmstadt

TECHNISCHE UNIVERSITÄT DARMSTADT

Physics Department
Institut für Kernphysik
Laser- und Plasmaphysik

Towards Ion Stopping Power Experiments with the Laser-Driven LIGHT Beamline
Auf dem Weg zu Energieverlustexperimenten mit der Lasergetriebenen LIGHT Beamline

Accepted doctoral thesis by Haress Nazary

Date of submission: 13.05.2024
Date of thesis defense: 10.07.2024

Darmstadt, Technische Universität Darmstadt

Erklärungen laut Promotionsordnung

§ 8 Abs. 1 lit. c PromO

Ich versichere hiermit, dass die elektronische Version meiner Dissertation mit der schriftlichen Version übereinstimmt.

§ 8 Abs. 1 lit. d PromO

Ich versichere hiermit, dass zu einem vorherigen Zeitpunkt noch keine Promotion versucht wurde. In diesem Fall sind nähere Angaben über Zeitpunkt, Hochschule, Dissertationsthema und Ergebnis dieses Versuchs mitzuteilen.

§ 9 Abs. 1 PromO

Ich versichere hiermit, dass die vorliegende Dissertation selbstständig und nur unter Verwendung der angegebenen Quellen verfasst wurde.

§ 9 Abs. 2 PromO

Die Arbeit hat bisher noch nicht zu Prüfungszwecken gedient.

Darmstadt, 13.05.2024

_____

H. Nazary

Kurzfassung

Ziel dieser Arbeit war es, ein Energieverlustexperiment mit der Laser Ion Generation Handling and Transport (LIGHT) Strahlführung, einer lasergetriebenen Ionenstrahlführung am Helmholtzzentrum für Schwerionenforschung (GSI), zu planen und vorzubereiten. Dafür wurde eine detaillierte Modellierung sowie die Demonstration der Machbarkeit des Experiments durchgeführt. In dem von mir geplanten Experiment wird die LIGHT-Strahlführung so konfiguriert, dass sie Kohlenstoffionenstrahlen (C^{4+}) und Protonenstrahlen mit einem Energie-zu-Masse-Verhältnis von 0,6 MeV/u selektiert und transportiert. Diese Ionen werden mit dem Petawatt High Energy Laser for Ion eXperiments (PHELIX) beschleunigt und über zwei Solenoide transportiert. Im Anschluss erfolgt eine zeitliche Kompression der Projektilpakete mittels einer Radiofrequenz-Kavität (RF), um die kürzest mögliche Paketlänge zu erreichen, um das transiente Plasma so exakt wie möglich zu untersuchen. Die Erzeugung des Plasmatargets erfolgt mit dem im Rahmen dieser Arbeit neu entwickelten und verbesserten Nanosecond High Energy Laser for Ion eXperiments (nhelix). Der nhelix-Laser wird eine Kohlenstofffolie mit einer Flächendichte von 100 μg/cm^2 von beiden Seiten mit einer Energie von jeweils 30 J bestrahlen. Die Pulslänge beträgt 7 ns und die Wellenlänge ist 527 nm. Das resultierende Plasma wird eine Dichte freier Elektronen von $3 \cdot 10^{20}$ cm^{-3} und eine Temperatur von 180 eV aufweisen, was zu einer Projektilgeschwindigkeit nahe der thermischen Geschwindigkeit der Plasmaelektronen führt ($v_{\mathrm{p}} \approx v_{\mathrm{th}}$). In diesem Bereich liegt das maximale Bremsvermögen, und die theoretischen Beschreibungen des Bremsvermögens weisen die größten Diskrepanzen auf. Das lasererzeugte Plasma wird mit einer interferometrischen Messung der Dichte der freien Elektronen diagnostiziert. Die Entwicklung, der Bau und die erfolgreiche Erprobung des interferometrischen Aufbaus wurden während dieser Arbeit von mir beaufsichtigt.

Ich habe das geplante Energieverlustexperiment modelliert, beginnend mit dem Transport des Ionenstrahls, über die Simulation des laserbeheizten Plasmatargets bis zur Wechselwirkung des Ionenstrahls mit dem Plasma, sowohl in Bezug auf den Energieverlust als auch auf den Ladungszustand. Zur Vorhersage der resultierenden Strahlcharakteristiken und der erforderlichen Strahlführungseinstellungen wurden Strahlführungssimulationen durchgeführt. Die endgültigen simulierten Strahlbündel wiesen eine zeitliche Bündelbreite von 300–340 ps und eine Fokusgröße von 4,5–5,5 mm am Plasmatarget auf. Das Plasma wurde mit dem hydrodynamischen Code MULTI2D modelliert. Eine maximale Temperatur von 180 eV und eine Dichte freier Elektronen in der Größenordnung von 10^{20} cm^{-3} wird nach 7,75 ns erreicht. Hier ist das Plasma longitudinal homogen. Im innersten Bereich, wo der Projektilstrahl das Plasma durchquert, wird nach 8 ns eine transversale Homogenität erreicht. Die Wechselwirkung des Ionenstrahls mit dem Plasmatarget wurde dann auf der Grundlage verschiedener theoretischer Modelle zur Beschreibung des Bremsvermögens modelliert. Eine zweidimensionale Simulation des gesamten Experiments wurde erfolgreich durchgeführt. Im Stoppmaximum sagen die Modelle für das Bremsvermögen einen erhöhten Energieverlust von 185–230 % für Protonen und 230–290 % für Kohlenstoffionen im Vergleich zum Energieverlust in einem festen Target voraus. Um zwischen fünf verschiedenen theoretischen Modellen für das Bremsvermögen zu unterscheiden, wurde bestimmt, dass eine erforderliche Energieauflösung von 11 % ausreicht, um aussagekräftige Ergebnisse zu erzielen. Die zweidimensionalen Simulationen wurden

eingesetzt, um die optimale Blendengröße für den Projektilstrahl in den Energieverlustexperimenten zu ermitteln, was zu einem Durchmesser von 0,5 mm führte.

Die Leistungsfähigkeit der Strahlführung wurde durch den Transport und die zeitliche Kompression von Kohlenstoffionen (C^{4+}) mit einer Energie von $(7,2 \pm 0,2)$ MeV auf eine Bündeldauer von $(1,23 \pm 0,04)$ ns (Halbwertsbreite) experimentell nachgewiesen. Der Durchmesser des Fokus betrug $(4,11 \pm 0,02)$ mm, während das komprimierte Bündel abgeschätzt $(2,0 \pm 0,6) \cdot 10^8$ Ionen umfasste. Des Weiteren wurden Protonen mit einer Energie von $(0,63 \pm 0,01)$ MeV transportiert und zeitlich auf eine Bündeldauer von $(0,76 \pm 0,04)$ ns komprimiert. Der Fokus hatte einen Durchmesser von $(2,82 \pm 0,03)$ mm und das Bündel enthielt abgeschätzt $(5,9 \pm 0,4) \cdot 10^8$ Protonen. Im Rahmen dieser Studie wurden Projektilstrahlen mit einer Länge verwendet, die fünf bis sieben Mal kürzer ist als die in früheren Experimenten mit Linearbeschleunigern. Dies führt zu einer kürzeren Mittelungszeit über sich in Nanosekunden ändernde Plasmaparameter. Die abgeschätzte Teilchenzahl liegt um zwei bis drei Größenordnungen höher als in ähnlichen Experimenten. Dies führt zu einer höheren möglichen Flugzeitdistanz in der Energiemessung und damit zu einer höheren Energieauflösung. Die transportierten Strahlen wurden zur Durchführung von Energieverlustexperimenten in einer festen Kohlenstofffolie verwendet, um die Durchführbarkeit des geplanten Experiments zu demonstrieren. Der gemessene Energieverlust für Protonen betrug $dE = (29 \pm 6)$ keV, während der gemessene Energieverlust für Kohlenstoffionen $dE = (61 \pm 10)$ keV betrug. Die beiden Werte stimmen mit den vorhergesagten Werten des SRIM-Codes (Stopping and Range of Ions in Matter) überein. Die Messungen lassen auf eine Unsicherheit von 7 % für Protonen und 6 % für Kohlenstoffionen in den Energieverlustmessungen mit dem Plasmatarget schließen. Die vorbereitenden Experimente demonstrieren die Durchführbarkeit des geplanten Energieverlustexperiments, welches aussagekräftige Daten für den Vergleich von Theorien zum Bremsvermögen liefern wird.

Abstract

The objective of this thesis was to plan and prepare for a stopping power experiment with the Laser Ion Generation Handling and Transport (LIGHT) beamline, which is a laser-driven ion beamline at Helmholtzzentrum für Schwerionenforschung (GSI). To this end, detailed modeling and a demonstration of the feasibility of the experiment were carried out. In the experiment I planned, the LIGHT beamline will be configured to select and transport carbon ion beams (C^{4+}) and proton beams with an energy-to-mass ratio of 0.6 MeV/u. These ions will be accelerated using the Petawatt High Energy Laser for Ion eXperiments (PHELIX) and transported via two solenoids. The projectile bunches will then be temporally compressed with a radio-frequency (RF) cavity to achieve the shortest possible bunch length, to examine the transient plasma as precisely as possible. The plasma target will be generated using the Nanosecond High Energy Laser for Ion eXperiments (nhelix), which was newly designed and upgraded within the scope of this work. The nhelix laser will irradiate a carbon foil with an areal density of $100 \, \mu g/cm^2$ from both sides with an energy of 30 J each. The pulse length is 7 ns and the wavelength is 527 nm. The resulting plasma is designed to have a free electron density of $3 \times 10^{20} \, cm^{-3}$ and a temperature of 180 eV, which results in a projectile velocity close to the thermal velocity of the plasma electrons ($v_p \approx v_{th}$). In this regime, the stopping maximum is located, and the stopping theories show their highest discrepancies. The laser-generated plasma will be diagnosed with an interferometric measurement of the free electron density. The development, construction, and successful testing of the interferometric setup were overseen by me throughout this work.

I modeled the planned stopping power experiment, encompassing the ion beam transport, the simulation of the laser-heated plasma target, and the interaction of the ion beam with the plasma, both in terms of energy loss and charge state. Beamline simulations were conducted to predict the resulting beam characteristics and requisite beamline settings. The final simulated bunches exhibited a temporal bunch width of 300–340 ps and focal spot size of 4.5–5.5 mm at the plasma target. The plasma was modeled using the MULTI2D hydrodynamic code. A maximum temperature of 180 eV and a free electron density in the order of $10^{20} \, cm^{-3}$ is reached after 7.75 ns. Here, the plasma is longitudinally homogeneous. In the innermost region, where the projectile beam passes through the plasma, transverse homogeneity is achieved after 8 ns. The ion beam's interaction with the plasma target was then modeled based on different theoretical models describing the stopping power. A two-dimensional simulation of the entire experiment was successfully conducted. In the stopping maximum, the stopping power models predict an increased energy loss of 185–230 % for protons and 230–290 % for carbon ions compared to the energy loss in a solid target. In order to differentiate between five different theoretical stopping power models, it was determined that a required energy resolution of 11 % is sufficient to yield meaningful results. The two-dimensional simulations were employed to identify the optimal pinhole size for the projectile beam in the stopping power experiments, resulting in a diameter of 0.5 mm.

The performance of the beamline was demonstrated experimentally by transporting and temporally compressing carbon ions (C^{4+}) with an energy of (7.2 ± 0.2) MeV to a bunch duration of (1.23 ± 0.04) ns (full width half maximum). The focal spot size was (4.11 ± 0.02) mm in diameter, and the compressed bunch was estimated to contain (2.0 ± 0.6) $\times 10^8$ ions. In addition, protons with an energy of (0.63 ± 0.01) MeV

were transported and temporally compressed to a bunch duration of (0.76 ± 0.04) ns. The focal spot size was (2.82 ± 0.03) mm in diameter, and the bunch was estimated to contain (5.9 ± 0.4) × 10^8 protons. The projectile beams utilized in this study are five to seven times shorter than those employed in previous experiments with linear accelerators, resulting in a shorter time averaging over plasma parameters that change in nanoseconds. The estimated particle numbers were two to three orders of magnitude higher than in similar experiments, resulting in a higher possible time of flight (ToF) distance when measuring the energy and therefore a higher energy resolution. The transported beams were used to conduct stopping power experiments in a solid carbon foil, to demonstrate the feasibility of the planned experiment. The measured energy loss for protons was $dE = (29 \pm 6)$ keV, while the measured energy loss for carbon ions was $dE = (61 \pm 10)$ keV. Both values are in agreement with the predicted values of the SRIM code (Stopping and Range of Ions in Matter). These measurements indicate an uncertainty of 7 % for protons and 6 % for carbon ions in the stopping power experiments with the plasma target. The preparatory experiments demonstrate the feasibility of the planned stopping power experiment, which will yield meaningful data for benchmarking stopping power theories.

Contents

1 Introduction

This doctoral thesis was conducted as part of the LIGHT (Laser Ion Generation, Handling and Transport) project. The project investigates the combination of a laser-generated ion source with conventional accelerator components to produce high-intensity ion bunches. This thesis aims to design and prepare a stopping power experiment using laser-accelerated ions in a laser-driven plasma with the LIGHT beamline. The introduction begins with a brief historical overview of stopping power research, followed by a presentation of selected applications of ion stopping in plasma (refer to Section 1.1). Subsequently, the physics and its current challenges are described (refer to Section 1.2). Finally, this work is placed within the context of experimental studies on stopping power (refer to Section 1.3).

The study of the interaction between ions and matter has been a subject of scientific investigation for over a century. Bohr's groundbreaking work in 1913 explored the deceleration of alpha particles in matter (Bohr 1913). Since then, researchers worldwide have conducted extensive theoretical, experimental, and numerical studies to comprehend and quantify the energy deposition of charged particles in matter. Although the stopping of ions in cold matter has been extensively examined using a wide range of experimental data (Bethe 1930; Bloch 1933; James F. Ziegler et al. 1985), there are still numerous unanswered questions when it comes to ion stopping in ionized matter, particularly in plasma. The theoretical description of this interaction remains a significant challenge, and only a limited amount of experimental data has been gathered thus far. The interaction between ions and plasma is of great importance in various fields of modern physics, including plasma physics. Understanding this interaction is particularly crucial for the realization of the Inertial Fusion Energy (IFE) concept, which aims to harness the energy generated by nuclear fusion reactions in plasma.

1.1 Applications of Ion Stopping in Plasma

This section emphasizes the significance of research on stopping power and its diverse applications. It initially concentrates on inertial confinement fusion (ICF) as a prospective energy source. Subsequently, the relevance of stopping power in plasma is explored in various applications.

1.1.1 Inertial Confinement Fusion

The loss of energy by ions in plasmas is a crucial factor in current research areas, such as inertial confinement fusion. This method is being studied as a potential candidate for future fusion power plants (Hurricane et al. 2019; Rosen 1999; A. B. Zylstra et al. 2019a). In this process, a small amount of fuel, consisting of a mixture of deuterium and tritium, is heated and compressed by a spherical implosion to ignite a thermonuclear burn wave (Haan et al. 1995; Lindl 1995; NUCKOLLS et al. 1972). This releases energy through the deuterium-tritium fusion reaction (^{2}H+^{3}H $\rightarrow n+^4$He), which heats the plasma through the

kinetic energy of the α-particles. The transferred energy rate is equal to the energy loss of the α-particles in the plasma. To maintain the fusion reaction, the energy loss of the 3.5 MeV α-particles produced in deuterium-tritium fusion reactions must dominate all loss processes. This causes the target to self-heat, ultimately leading to further fusion reactions. To accurately model ignition experiments at the National Ignition Facility (NIF) (Abu-Shawareb et al. 2024; Hurricane et al. 2014; Miller et al. 2004; A B Zylstra et al. 2022a,b) and future ignition experiments, it is necessary to understand the transport of α-particles in plasma.

The NIF laboratory achieved the burning plasma state with current stopping power descriptions and decades of fusion research (A B Zylstra et al. 2022a). In an indirect drive fusion implosion 2.05 MJ of laser light produced 3.1 MJ of total fusion yield, resulting in a target gain of 1.5 (Abu-Shawareb et al. 2024). This marks the first laboratory demonstration of exceeding "scientific breakeven". This achievement demonstrates that laboratory fusion, based on fundamental principles of physics, is possible.

The transport and energy deposition of charged particles in plasmas, as well as the heating of dense plasmas, are crucial for developing alternative designs of inertial confinement fusion with particle beams. Two examples of fusion designs are heavy ion fusion (Callahan-Miller et al. 2000; Hofmann 2018; Humphries 1980), in which a stream of high-energy ions from a particle accelerator rapidly heats and compresses a small pellet of fusion fuel, and proton fast ignition (Fernández et al. 2014; Roth et al. 2001; Tabak et al. 1994), in which the cold fuel is precompressed and subsequently ignited with a separate short-pulse high-intensity proton pulse.

1.1.2 Diverse Relevancy of Ion Stopping in Plasma

In addition to fusion, ion stopping in plasma is a critical factor in various other contexts. One specific application of ion stopping in plasma is in electron cooling systems. These systems employ cold electron plasmas, i.e., monoenergetic electron beams, as a stopping medium to reduce the emittance of heavy ion beams in storage rings (Poth 1990; Winkler et al. 1997).

In accelerator physics, plasmas can serve as ion strippers (Alton et al. 1992; K.-G. Dietrich et al. 1992; Loisch et al. 2015) or ion focusing lenses (Chiadroni et al. 2018; Panofsky et al. 1950; Pompili et al. 2017; Yan et al. 2023). A comprehensive understanding of ion-plasma interaction is necessary for these applications.

Ion stopping is crucial for astrophysical phenomena where plasma is the fundamental state of matter. Understanding ion stopping mechanisms in plasma is essential for various processes, including the transport and interaction of cosmic-ray particles (Ferrari 1998), stellar transport, and the rapid neutron capture process (r-process), which is a nucleosynthesis mechanism in astrophysics that occurs in supernovae and neutron star mergers, where heavy atomic nuclei are formed.

This is just a small selection of applications, but it still demonstrates the importance of providing stopping power descriptions in a wide range of regimes. The following section presents the progress and challenges of achieving this objective.

1.2 Physics Case

The theoretical treatment of ion stopping remains a challenging problem despite decades of extensive analytical and numerical studies. Interactions between projectiles and plasma can involve very different and rapidly changing plasma conditions, resulting in very different ion stopping behaviors.

The ion stopping power has various theoretical descriptions, which depend on the projectile and plasma characteristics, ion-plasma coupling, and the balance between collisional and collective phenomena. Therefore, developing a unified picture of the ion stopping process in plasma is a challenging task. Also, the projectile's charge-state value in the plasma is an important but not yet fully established quantity. It depends on atomic cross sections, charge-transfer processes, and plasma parameters.

The interaction between ions and plasma is well understood for high projectile ion velocities v_{p}, typically measured in units of the thermal velocity of free plasma electrons v_{th}. When $\frac{v_{\text{p}}}{v_{\text{th}}} \gg 1$, the ion energy deposition can be described using a Bethe formula (Bethe 1930, 1932). However, in the low-velocity regime, the stopping process is influenced by factors such as close collisions and plasma polarization, which require adapted correction terms. As the projectile ion velocity approaches $\frac{v_{\text{p}}}{v_{\text{th}}} \approx 1$, the theoretical description becomes increasingly complex due to the region of maximum stopping power. In this velocity range, both close particle collisions and collective plasma oscillations significantly affect the stopping power, and the projectile charge state may exhibit important non-equilibrium behavior. The Coulomb coupling between the projectile and plasma electrons is maximized, making it difficult to describe the interaction using perturbation theory.

In ICF, predicting α-particle heating precisely is challenging due to theoretical uncertainties. This is because the velocity of the α-particles v_{α} is either lower or equal to the thermal velocity of the plasma electrons ($v_{\alpha} \leq v_{\text{e,th}}$) for most of the fusion process. A decrease in α-particle stopping causes a nearly equal increase in range. This may impact the thermonuclear burn wave's ignition threshold in the dense main fuel, as well as the energy deposition inside the hot spot of a burning deuterium-tritium plasma (Edie et al. 2013).

Accurate measurements of ion stopping near the stopping maximum are crucial for directing theoretical efforts. Theoretical descriptions of ion stopping in plasmas have been proposed by Deutsch et al. 2010; D. O. Gericke et al. 1999; Li et al. 1993a; G. Maynard et al. 1985; Peter et al. 1991b; Zimmerman 1997 and BROWN et al. 2005. Although several attempts have been made to theoretically describe ion stopping behavior in plasmas, there is only a limited amount of experimental evidence to support these theories (W. Cayzac et al. 2017; S. N. Chen et al. 2018; Frenje et al. 2019; Hayes et al. 2020; Malko et al. 2022; A. Zylstra et al. 2020). Suitable laser-generated plasmas for these measurements are typically very small and highly transient. This places significant demands on the experimental equipment, especially on the ion beam used for plasma probing. Previous experiments are summarized and categorized in the following section.

1.3 Context of the Work

This section reviews the experimental landscape of ion stopping power in plasma. Figure 1.1 displays the parameter domain examined in previous experiments as a function of the velocity ratio v_p/v_{th} and the electron coupling parameter Γ, which quantifies the strength of electron-electron coupling in the probed plasma. Initial experiments have been conducted in cold hydrogen plasmas generated by either electric gas-discharge (Belyaev et al. 1996; Gardes et al. 1992; Jacoby et al. 1995) or by Z-pinch targets (Dietrich et al. 1990; Flierl et al. 1998; Hoffmann et al. 1990) with low plasma density ($n_e \approx 10^{17}$–10^{18} cm^{-3}) and high-energy probe ion beams on a MeV/u scale. In order to access regimes of higher temperature and higher density that are relevant to ICF, experiments using laser-generated plasmas had to be carried out. Laser-generated plasma (S. N. Chen et al. 2018; Couillaud et al. 1994; A. Frank et al. 2013; Malko et al. 2022; Roth et al. 2000; Sakumi et al. 2001) and exploding-pusher experiments (Frenje et al. 2015, 2019; Hicks et al. 2000) can reach lower to moderate velocity ratios (v_p/v_{th}) up to 6 but are often limited to hot, ideal plasmas. X-ray-driven targets can be used to achieve cold and dense plasma conditions (Lahmann et al. 2023; Ortner 2015; Ren et al. 2020; A. B. Zylstra et al. 2015).
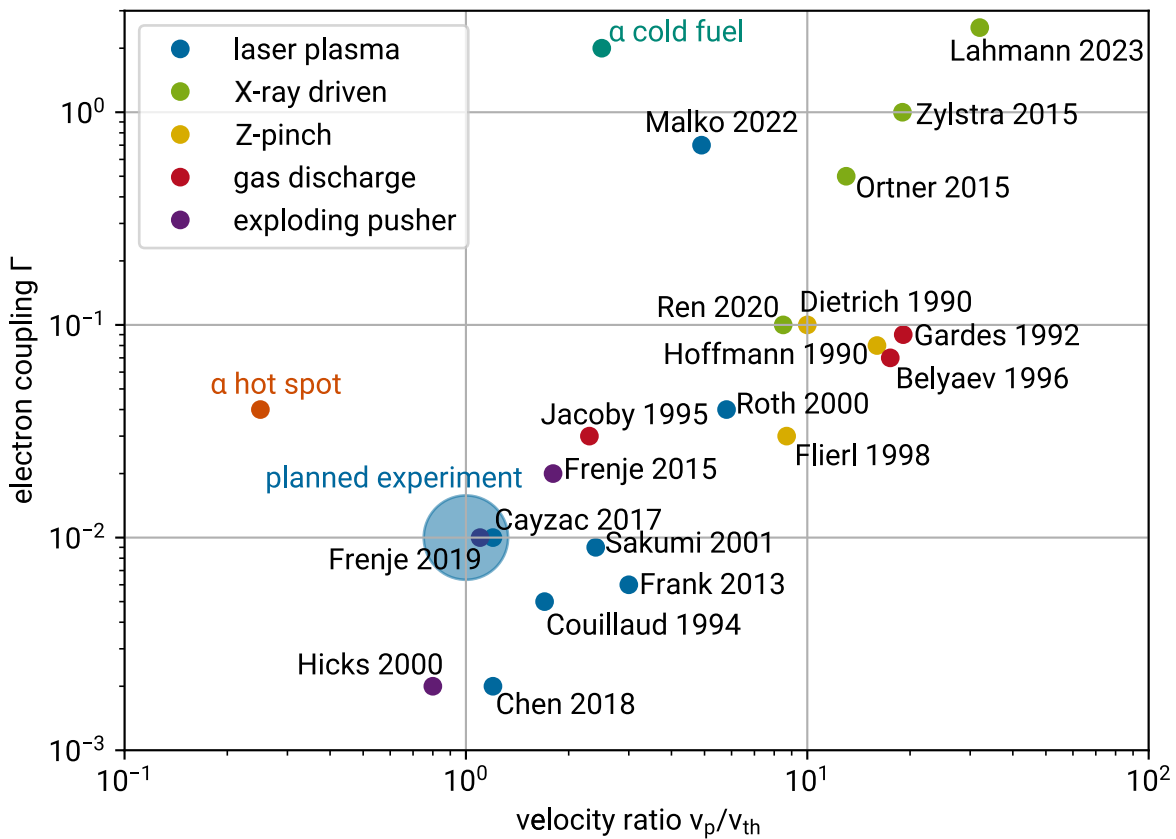

Figure 1.1: Reported ion stopping experiments displayed in the parameter space of the velocity ratio v_p/v_{th} of the beam plasma interaction and the electron coupling Γ.

This thesis extends the legacy of ion stopping power research through an experimental investigation using the LIGHT beamline. The experiment presented in this thesis aims to study the maximum stopping velocity ($v_\mathrm{p} \approx v_\mathrm{th}$) in an ideal plasma ($\Gamma \approx 0.01$). This experiment is designed to validate the results of W. Cayzac et al. 2017 and Frenje et al. 2019 with higher accuracy. It will be the first of many stopping power experiments utilizing the infrastructure and platform built at the experimental area Z6 at Helmholtzzentrum für Schwerionenforschung (GSI). The LIGHT beamline can cover a wide parameter space for stopping power experiments by employing various configurations of different targets, plasma parameters, and ion beams.

1.4 Structure of the Thesis

This thesis aims to design an experimental campaign to measure stopping power using the LIGHT beamline. Chapter 2 presents a comprehensive description of the theoretical foundation required for this work, including general plasma physics, laser-plasma interaction, and ion-plasma interaction. This chapter covers important features of ion stopping and provides a summary of modern stopping power theories and models. Chapter 3 outlines the planned experiment and explains the role of the LIGHT beamline in generating the projectile beam, as well as the role of the Nanosecond High Energy Laser for Ion eXperiments (nhelix) in plasma generation. Chapter 4 details the modeling of the planned experiment using the concepts and theories discussed in Chapter 2. The simulation incorporates the corresponding plasma, projectile, and stopping properties. Chapter 5 presents the preparatory experimental campaigns, which demonstrate the generation of desired projectile beams with the LIGHT beamline and stopping experiments in solid targets. Finally, Chapter 6 summarizes the thesis and provides an outlook on the research field of ion stopping in plasma.

2 Stopping Theory

This chapter introduces the physical concepts necessary to describe the planned stopping power experiment in this work (see Chapter 3). Its purpose is to provide a comprehensive theoretical understanding of ion-plasma interaction, which is essential for the modeling of the proposed stopping power experiment in Chapter 4.

Before discussing ion-plasma interaction, it is crucial to describe the plasma itself, including its essential parameters and properties. The first part of this chapter introduces plasma physics and emphasizes its important properties and characteristics (refer to Section 2.1). The second part provides a detailed study of the interaction of ions with plasma and presents a comprehensive overview of the theory of ion stopping in plasma (refer to Section 2.2). The theoretical portion of this work expresses all physical quantities in the cgs unit system (centimeter, gram, second), while numerical values are given in SI base units.

2.1 Plasma Physics Fundamentals

This section is based on well-known standard works of plasma physics unless otherwise referenced (Atzeni et al. 2004; Drake 2006; Mulser et al. 2010; Piel 2017).

A plasma is a gas composed of ionized atoms, consisting of positively charged ions and negatively charged free electrons. The motion of these charged particles is primarily influenced by local electric and magnetic fields, which the particles themselves generate. Describing plasma dynamics can be complex due to the interplay between these fields. Although a plasma is electrically neutral overall due to the mutual screening of the electric potential of the ions and free electrons, it cannot be considered locally neutral. Therefore, the term quasi-neutrality is used. To better understand a plasma, it can be analogized to a two-component fluid comprising of free electrons with a mass of m_e and ions with a mass of m_i. In this context, it is possible to define the electron density n_e, ionic density n_i, electron temperature T_e, ion temperature T_i, and mean ionization degree Z_T. The **kinetic energy** E_{kin} of the particles in the plasma is defined by:

$$E_{kin,i,e} = k_B T_{e,i} = m_{e,i} v_{th,e,i}^2 \tag{2.1}$$

Here, k_B is the Boltzmann constant and $v_{th,e,i}$ is the thermal velocity of the particles. In the remainder of this work, v_{th} always is the thermal velocity of the plasma electrons ($v_{th} = v_{th,e}$). In the context of the three-dimensional Maxwellian speed distribution of electrons, $E_{kin,i,e} = \frac{3}{2} k_B T_{e,i} = \frac{1}{2} m_{e,i} v_{th,e,i}^2$ and $v_{th} = \sqrt{\frac{3k_B T_e}{m_e}}$, and Equation 2.1 is the standard deviation of this distribution. Nevertheless, the simplified formula (see Equation 2.1) is frequently utilized in the literature for stopping power calculations, as will also be the case in this thesis unless otherwise stated. In this work, a hot and dense laser-induced plasma is planned for energy loss measurements, with $n_{e,max} = 3 \times 10^{20} \, \text{cm}^{-3}$ and $T_{e,max} = 180 \, \text{eV}$.

Locally, Coulomb scattering dominates particle collisions, while on a larger scale, collective plasma effects may become apparent. The interaction strength between two particles in the plasma can be estimated using different characteristic parameters, which also describe the collisional and collective aspects of plasma interactions.

Free electrons in the plasma that are repelled by an electric field generate a positive space charge, which acts as a restoring force on the electrons. The plasma's collective effects are characterized by the resulting oscillation of the plasma electrons, denoted by the **plasma frequency** ω_p:

$$\omega_\mathrm{p} = \sqrt{\frac{4\pi n_\mathrm{e} e^2}{m_\mathrm{e}}}. \tag{2.2}$$

Here, n_e represents the electron density, and m_e represents the electron mass. The contribution of plasma ions can be disregarded because $m_\mathrm{i} \gg m_\mathrm{e}$. The plasma frequency in this study is $\omega_\mathrm{p} = 10^{15}$ rad/s.

A characteristic length is the **Wigner-Seitz radius** a which describes the mean distance between two plasma electrons:

$$a = \left(\frac{4\pi n_\mathrm{e}}{3}\right)^{-\frac{1}{3}}. \tag{2.3}$$

In this work for a free electron density of $n_\mathrm{e} = 3 \times 10^{20}$ cm^{-3} this distance is around 9×10^{-10} m.

The **Landau length** r_0 is the classical distance of minimal approach between two plasma electrons. This corresponds to the distance where the kinetic and potential energies are equal. The term is defined as:

$$r_0 = \frac{e^2}{m_\mathrm{e} v_\mathrm{th}^2}. \tag{2.4}$$

For a temperature of $T_\mathrm{e} = 180$ eV, r_0 is estimated to be 8×10^{-12} m. A generalized Landau length can be defined for the interaction of any two particles in a plasma. It is determined by the charges of the particles (Z_α and Z_β), their relative velocity ($v_\mathrm{r} = |v_\alpha - v_\beta|$), and their reduced mass ($\mu = m_\alpha m_\beta / (m_\alpha + m_\beta)$):

$$r_{\alpha\beta} = \frac{Z_\alpha Z_\beta}{\mu v_\mathrm{r}^2}. \tag{2.5}$$

The **De Broglie wavelength** $\lambda_{\alpha\beta}$ is the wavelength associated with a moving body. It can be interpreted as the distance below which quantum diffraction effects between two particles begin to appear. For particles α and β it can be written as:

$$\lambda_{\alpha\beta} = \frac{\hbar}{\mu v_\mathrm{r}}, \tag{2.6}$$

For the plasma electrons, it is defined as:

$$\lambda_\mathrm{e} = \frac{\hbar}{m_\mathrm{e} v_\mathrm{th}}. \tag{2.7}$$

For $T_\mathrm{e} = 180$ eV the electron De Broglie wavelength is 2×10^{-11} m.

A plasma is considered nondegenerate when the kinetic energy of the electrons (see Equation 2.1) dominates over their **Fermi energy** E_F:

$$E_\mathrm{F} = \frac{\hbar^2}{2m_\mathrm{e}} \left(3\pi^2 n_\mathrm{e}\right)^{\frac{2}{3}} \tag{2.8}$$

and it obeys the classical Maxwell-Boltzmann statistic, which means the Pauli exclusion rule can be ignored. To measure the degree of plasma degeneracy a **degeneracy parameter** Θ is defined as the ratio between the kinetic energy of the plasma electrons (see Equation 2.1) and their Fermi energy (see Equation 2.8):

$$\Theta = \frac{k_{\mathrm{B}} T_{\mathrm{e}}}{E_{\mathrm{F}}} = 2\alpha^2 \left(\frac{a}{\lambda_e} \right)^2 \tag{2.9}$$

with $\alpha = \left(\frac{4}{9\pi} \right)^{\frac{1}{3}}$. For $\Theta \gg 1$, the plasma is nondegenerate. However, for $\Theta \leq 1$, the plasma becomes degenerate, and the Pauli exclusion rule cannot be ignored. In this case, the electrons obey the Fermi-Dirac statistics, and their kinetic energy is expressed as the sum of the thermal energy (see Equation 2.1) and the Fermi energy (see Equation 2.8). The plasma in this work is nondegenerate, as $\Theta \approx 1100$.

The plasma's quasi-neutrality results in the presence of collective effects. A local perturbation of the electric field causes a redistribution of charged particles to neutralize the generated electric potential. This phenomenon is known as screening or shielding of the electric potential of charged particles in a plasma. As a result, the electric potential of a particle has a strong local influence, but its range of influence is limited to a region described by the **screening length** λ. A typically used screening length is the **Debye length** λ_{D}:

$$\lambda_{\mathrm{D}} = \frac{v_{\mathrm{th}}}{\omega_{\mathrm{p}}} = \sqrt{\frac{k_{\mathrm{B}} T_{\mathrm{e}}}{4\pi e^2 n_{\mathrm{e}}}}. \tag{2.10}$$

It describes a case of static and linear screening. The first condition implies that the velocity of the screened particle does not affect it. The second condition implies that the potential energy of the interaction between the plasma particles is negligible compared to their kinetic energy. Thus, the Debye length is only applicable when there are a sufficient number of electrons within the Debye sphere ($N_{\mathrm{D}} = \frac{4}{3}\pi n_{\mathrm{e}} \lambda_{\mathrm{D}}^3 \gg 1$). The Debye sphere is a sphere with a radius equal to the Debye length. In the plasma discussed in this work, $N_{\mathrm{D}} \approx 240$ and $\lambda_{\mathrm{D}} \approx 6\,\mathrm{nm}$. When N_{D} is small, the screening effect becomes nonlinear and cannot be accurately described using the Debye length. This is the case for an ICF plasma where $N_{\mathrm{D}} \approx 2$. For an external particle interacting with the plasma at a high enough velocity, it is necessary to consider a dynamic screening length $\lambda = \lambda(v_{\mathrm{p}})$. In the case of a nondegenerate plasma, the velocity dependant screening length can be written as:

$$\lambda(v_{\mathrm{p}}) = \lambda_{\mathrm{D}} \left(1 + \left(\frac{v_{\mathrm{p}}}{v_{\mathrm{th}}} \right)^2 \right)^{\frac{1}{2}}. \tag{2.11}$$

Collective effects in plasma interaction processes occur at a length scale larger than the screening length λ. These effects include the excitation of plasmons or dynamic screening. However, in a plasma with a small screening length ($\lambda < a$), collective effects are defined for interaction distances larger than the Wigner-Seitz radius a (see Equation 2.3). Interaction processes occurring over distances below the screening length are direct particle interactions, such as particle collisions or Coulomb scattering. The dominant effect is determined by the minimal distance between the initial trajectories of two interacting particles, which is referred to as the **impact parameter** b of the interaction.

The **plasma coupling parameter** Γ is used to measure the strength of electron-electron coupling in a plasma:

$$\Gamma = \frac{E_{\mathrm{C}}}{E_{\mathrm{kin}}} = \frac{e^2}{a k_{\mathrm{B}} T_{\mathrm{e}}} = \frac{1}{3} \left(\frac{a}{\lambda} \right)^2. \tag{2.12}$$

Γ, also called the nonideality parameter, is calculated by dividing the Coulomb energy $E_{\mathrm{C}} = \frac{e^2}{a}$, which is the potential interaction energy of the electrons, by their thermal kinetic energy (see Equation 2.1).

It is directly related to the Wigner-Seitz radius (see Equation 2.3) and the screening length λ. A value of $\Gamma \ll 1$ indicates that the kinetic energy of the electrons is greater than their potential energy, which suggests that the plasma is ideal, collisionless, and characterized by long-range collective plasma effects. As a result, $N_{\mathrm{D}} \gg 1$ and the Debye length is well defined and relatively large. In this work, the plasma is ideal because $\Gamma \approx 0.01$. If $\Gamma > 0.1$, the plasma is considered moderately nonideal, and if $\Gamma > 1$, it is nonideal and dominated by collisions between the electrons. In highly nonideal plasmas, the concept of Debye screening becomes ill-defined as plasma collisions become more prevalent than collective effects. A similar coupling parameter, Γ_{ei}, can also be used to characterize the strength of correlations between electrons and ions in the plasma. The expression for Γ is valid only if the plasma being considered is nondegenerate.

Table 2.1 summarizes all presented plasma characteristics for the plasma target in the planned stopping power experiment (refer to Chapter 3). The plasma is a fully ionized carbon plasma with a temperature of $T_{\mathrm{e}} = 180\,\mathrm{eV}$ and a free electron density of $n_{\mathrm{e}} = 3 \times 10^{20}\,\mathrm{cm}^{-3}$. It is an ideal and nondegenerate plasma.

Table 2.1: Plasma parameters for the fully ionized carbon plasma target of the planned stopping power experiment ($T_{\mathrm{e}} = 180\,\mathrm{eV}$ and $n_{\mathrm{e}} = 3 \times 10^{20}\,\mathrm{cm}^{-3}$).

a	r_0	λ_{e}	λ_{D}	N_{D}	Γ	Θ	ω_{p}
$9 \times 10^{-10}\,\mathrm{m}$	$8 \times 10^{-12}\,\mathrm{m}$	$2 \times 10^{-11}\,\mathrm{m}$	$6 \times 10^{-9}\,\mathrm{m}$	240	0.01	1100	$10^{15}\,\mathrm{rad/s}$

This description of plasma enables the description of the interaction of an ion beam with plasma.

2.2 Stopping Power

The purpose of this section is to introduce various ion stopping theories for stopping in plasma that will be used to make predictions for the planned experiments in Chapter 4. Before delving into these theories, a broad overview of ion stopping is given, outlining the general features of ion-target interactions and the processes involved. In a typical energy loss experiment, the kinetic energy of ions is compared before and after passing through matter. The energy loss of ions refers to the transfer of energy from ions to the matter they pass through. Charge exchange processes between the ion and the matter can also occur, leading to a variation in the charge state, which in turn affects the energy loss. In plasma, both the energy loss and the charge state differ from those in cold matter. The energy loss and evolution of the charge state are determined by the cross-sections of microscopic Coulomb processes. In this context, the energy loss in plasma is explained based on the energy loss in cold matter. First, a fundamental stopping power model for cold matter is presented. The modifications of stopping power in plasma are then explained, and a basic model of ion stopping in plasma is described. However, to account for the stopping maximum, more advanced theoretical considerations are required. A description of the different perturbation regimes of ion-plasma interaction and the distinct theoretical treatments required for different impact parameter regimes is necessary. Therefore, a characterization of the beam-plasma interaction is conducted. Different theoretical approaches to ion stopping power in plasma are presented. These include dielectric theory, binary collision theory, and kinetic plasma theory. Approaches aimed at providing a unified stopping description are also discussed. The following section discusses the stopping power induced by bound electrons and various methods for calculating it. Additionally, the charge state of the projectile ions and models used to estimate its evolution are presented.

2.2.1 Stopping Power in Cold Matter

When ions pass through matter, they can lose energy in several ways, including excitation and ionization of target electrons, excitation and ionization of the projectile, capture of target electrons, nuclear energy loss, and electromagnetic radiation (Sigmund 2004).

The ions lose energy through inelastic collisions with target electrons and elastic collisions with target ions, resulting in corresponding electronic and nuclear energy loss. Excitation and ionization of target electrons are dominant over a wide range of speeds, while nuclear energy loss is only significant for projectile energies below 0.2 MeV/u (James F. Ziegler et al. 1985). This occurs as the projectile velocity becomes comparable to or lower than typical atomic velocities in the target material. Excitation and ionization of projectile ions, as well as the capture of target electrons, are relevant for energies below 1 MeV/u. At high velocities, electromagnetic radiation becomes more significant. The target energy for measuring the energy loss of carbon ions and protons is 0.5 MeV/u, which allows for examination of the region of the stopping maximum ($\frac{v_p}{v_{th}} \approx 1$). In this non-relativistic range, nuclear energy loss and electromagnetic radiation can be disregarded. Within the non-relativistic frame, the stopping power in matter can be divided into three main regimes, each requiring a different stopping power description. The borders of these regimes vary from case to case, particularly for the plasma case. (Bimbot et al. 2005; Sigmund 2004)

For low velocities (< 0.1 MeV/u), a simple model is available where the stopping power is proportional to the projectile velocity (J. Lindhard et al. 1961).

For high velocities (> 10 MeV/u), a description based on the Bethe formula can be used (Bethe 1930, 1932). This has been confirmed in numerous experiments (James F. Ziegler et al. 1985). The Bethe formula is presented in the following.

The transfer of energy ΔE from a pointlike ionized projectile with charge number Z_p and velocity v_p to electrons in a target can be expressed as:

$$\Delta E(b) = \frac{(\Delta p)^2}{2m_e} = 2\frac{Z_p^2 e^4}{b^2 v_p^2} \tag{2.13}$$

with an impact parameter b which describes the minimal distance between trajectories of the projectile ion and a target electron during the interaction (see Section 2.1). The nuclear stopping power is neglected due to the large mass of the target ion compared to the target electron ($m_i \gg m_e$). The projectile interacts with $2\pi b\, db\, n_b\, dx$ electrons at impact parameter b after traveling a path length dx in a medium with electron density n_b. The integration over all impact parameters b leads to the stopping power:

$$\frac{dE}{dx} = -\frac{4\pi Z_p^2 e^4 n_b}{m_e v_p^2} \int \frac{db}{b}. \tag{2.14}$$

To prevent the divergence of the integral and an unphysical infinite stopping power, it is necessary to establish a minimum and maximum impact parameter. The minimum impact parameter, b_{min}, is defined as the generalized Landau length $r_{i,e}$ (see Equation 2.5), which is the classical distance of minimum approach between the projectile ion and an electron. The relationship $m_i \gg m_e$ and $v_p \gg v_e$ holds, leading to $r_{i,e} = \frac{Z_p e^2}{m_e v_p^2}$. The maximum value of b, denoted as b_{max}, is limited by the collision duration $\Delta t \approx \frac{b}{v_p}$, which must be smaller than the oscillation period of the bound electrons characterized by the frequency ω.

Therefore, b must be smaller than $b_{\max} = \frac{v_{\mathrm{p}}}{\omega}$. By calculating the integral, one obtains the Bohr classical stopping power expression:

$$\frac{dE}{dx} = -\frac{4\pi Z_{\mathrm{p}}^2 e^4 n_{\mathrm{b}}}{m_{\mathrm{e}} v_{\mathrm{p}}^2} \cdot \mathcal{L} \tag{2.15}$$

with the Coulomb logarithm (Bohr 1913):

$$\mathcal{L}_{\mathrm{Bohr}} = \ln\left(\frac{m_{\mathrm{e}} v_{\mathrm{p}}^3}{Z_{\mathrm{p}} e^2 \omega}\right). \tag{2.16}$$

The Coulomb logarithm quantifies the relative importance of weak collisions ($b \approx b_{\max}$) to strong collisions ($b \approx b_{\min}$). This is a classically described Coulomb logarithm for small impact parameters, which overestimates the stopping power for large impact parameters. The Coulomb logarithm by Bethe is derived through a perturbative quantum mechanical calculation and is valid for large impact parameters (Bethe 1930, 1932):

$$\mathcal{L}_{\mathrm{Bethe}} = \ln\left(\frac{2m_{\mathrm{e}} v_{\mathrm{p}}^2}{\bar{I}}\right). \tag{2.17}$$

Here, $\bar{I}$ represents the average ionization potential of the atoms.

In the intermediate velocity regime, excitation and ionization of both the target electrons and the projectile, as well as electron capture, are expected to be important. Multiple mechanisms result in a maximum in the intermediate-velocity section of the stopping power curve. The theoretical stopping description of this part is complex. The velocity at which the maximum is reached is the characteristic velocity of the target electrons. In cold matter, it is that of the bound target electrons. It can be estimated from the Bohr velocity v_0, the atomic number Z_{an}, and the electron orbital n: $v_{\mathrm{b,e}} = v_0 \frac{Z_{\mathrm{an}}}{n}$. In plasma, the characteristic velocity is the thermal velocity of the free electrons, v_{th}. To describe this regime in cold matter, several corrections have been added to the Bethe formula. All of these corrections in cold matter are summarized in detail in J. F. Ziegler 1999 and Sigmund et al. 2002.

The Bloch correction adds closer collisions (Bloch 1933) to the Bethe formula to account for the intermediate regime between the quantum mechanical description, where the projectile ions are a small perturbation on the target electrons, and the classical description, where the perturbation cannot be considered small. The corrective Bloch term is:

$$\mathcal{L}_{\mathrm{Bloch}} = \psi(1) - \mathrm{Re}\left(\psi(1 + Z_{\mathrm{p}} v_0/v_{\mathrm{p}})\right) = \sum_{k=1}^{\infty} \frac{1}{k} \frac{(Z_{\mathrm{p}} v_0/v_{\mathrm{p}})^2}{k^2 + (Z_{\mathrm{p}} v_0/v_{\mathrm{p}})^2}. \tag{2.18}$$

The Digamma function, denoted by ψ, is the logarithmic derivative of the Gamma function. The Bloch correction enables access to a quantum stopping power description beyond basic perturbation theory. The Bethe and Bethe-Bloch formulas are valid at high projectile velocities but cannot describe the stopping maximum. Both formulas were implemented and used for comparison in the theoretical predictions (see Chapter 4).

A second correction needs to be considered to account for the Barkas effect (Barkas et al. 1963). The Barkas effect is a polarization effect that causes charged particles to have different stopping powers than their antiparticles. Positively charged particles attract target electrons, which causes the local electron density to rise and thus enhances the stopping power. This effect is significant for projectile velocities below 1 MeV/u. The corrective Barkas term can be written as (Jens Lindhard 1976):

$$\mathcal{L}_{\mathrm{Barkas}} = \frac{3\pi Z_{\mathrm{p}} e^2 \omega}{2m_{\mathrm{e}} v_{\mathrm{p}}^3} \mathcal{L}_{\mathrm{Bethe}} \tag{2.19}$$

where ω represents the resonance frequency that characterizes the target electrons. For more information on the Barkas correction, refer to Sigmund et al. 2003.

The shell correction, which takes the movement of target electrons into account, is only relevant for projectile velocities below $0.3\,\text{MeV/u}$ (Bimbot et al. 2005) and is therefore neglected in this work.

Projectile Charge State

The energy loss is significantly affected by the charge state of the projectile ions. This effect is modified when the projectile ion undergoes ionization or recombination due to collisions. In cold matter, the three major charge-exchange processes are ionization by Coulomb collision with target atoms, non-radiative electron capture (NREC), and radiative electron capture (REC). NREC has a relatively high cross section and involves the transfer of a bound electron from the target to the projectile, with the target atom taking over the excess energy and momentum. Recombination by radiative electron capture is the second most dominant process. In this mechanism, a target atom is ionized, and the resulting free electron is subsequently captured by the projectile. To conserve energy and momentum, a photon is emitted.

Charge exchange mechanisms are statistical and their cross sections depend on the projectile ion, its charge state, its velocity, and the target material. The projectile beam reaches an equilibrium charge state distribution after a brief period, which depends on these parameters. This equilibrium charge state represents the average charge state:

$$Z_{\text{eq}} = \sum_i f_i Z_i. \tag{2.20}$$

Z_i represents the different charge states, and f_i represents the corresponding statistical weights. Solids generally have a higher Z_{eq} value than gases due to the density effect (Gilles Maynard et al. 2000; SHEVELKO et al. 2010). This is because solids have a higher density than gases, resulting in more collisions between projectile ions and the atoms of the medium in a shorter time. As a result, projectile electrons have less time to de-excite before the next collision, making the ionization of a projectile ion more likely in solids than in gases.

Describing the charge transfer cross sections completely is a challenging task, which is why the equilibrium mean charge state is typically estimated using empirical models. One of the most commonly used models is the Northcliffe model (Northcliffe 1960):

$$Z_{\text{eq}} = \sqrt{1 - 1.85 e^2 \frac{v_{\text{p}}}{v_k}} Z_{\text{an}} \tag{2.21}$$

where v_k represents the orbital velocity of the first k electron according to Bohr's model, and Z_{an} represents the atomic number of the projectile. There are also several more recent semi-empirical scaling laws (Schiwietz et al. 2001; Shima et al. 1989; James F. Ziegler et al. 1985).

The evolution of the charge state in the target material can also be described and simulated using rate equations, provided that the effective cross-sections of the individual processes leading to the charge transfer are known. Various codes have been developed to estimate the mean charge state, with the ETACHA code being one of the most commonly used (Lamour et al. 2015; Rozet et al. 1996).

In reality, the core potential of an ionized projectile ion is partially shielded by the bound electrons. To account for this effect, an effective charge state, Z_{eff}, can be introduced. This charge state cannot be physically traced back to the real one and is therefore only useful as a fit parameter.

A full theoretical description of ion stopping in cold matter is not available and some uncertainties still exist in cold matter due to the complexity of the physics involved. However, there is a relatively good understanding established, and numerous experiments have been conducted, enabling the establishment of reliable data tables (Paul 2006). Calculations are generally based on approximate data tables or semi-empirical approaches found in the literature. In this work, the well-known SRIM (Stopping and Range of Ions in Matter) code (James F. Ziegler et al. 1985) is used to calculate the stopping power in cold matter.

2.2.2 Standard Stopping Model in Plasma

In plasma, the interaction between projectile ions and matter is complex due to the presence of free electrons. This results in rapidly changing plasma densities, temperatures, and ionization conditions, which can lead to varying energy loss behaviors. To obtain a comprehensive physical description, it is necessary to consider both collisions and collective effects, such as the excitation of plasmons or dynamic shielding of the projectile charge by plasma electrons. Various theories exist to describe energy loss depending on the properties of the projectile and plasma.

The loss of energy is influenced by both the free electrons and the partially or fully ionized target atoms. It is important to consider plasma ions with different charge states separately, as they have different average ionization potentials. Additionally, it is worth noting that projectile ions can transfer energy to the free electrons. The Coulomb logarithm of free electrons, and therefore the mean energy transfer, is affected by plasmons. A plasmon is a quantized oscillation of electrons relative to positively charged ions. The transfer is determined by the energy of the plasmon, which is accounted for in the Bethe formula for free electrons:

$$\frac{dE}{dx}_{\text{free}} = -\frac{4\pi Z_p^2 e^4 n_e}{m_e v_p^2} \cdot \mathcal{L} = -\frac{Z_p^2 e^2 \omega_p^2}{v_p^2} \cdot \mathcal{L}. \tag{2.22}$$

It is derived by replacing the bound electron density n_b of Equation 2.15 with the free electron density n_e. The plasma frequency for free electrons ω_p in a plasma given by Equation 2.2 and the Coulomb logarithm for free electrons in the Bethe formalism is given by:

$$\mathcal{L}_{\text{Bethe, free}} = \ln\left(\frac{2m_e v_p^2}{\hbar \omega_p}\right). \tag{2.23}$$

The plasmon energy, $\hbar \omega_p$, falls within the range of a few electron volts, whereas the ionization potential $\bar{I}$ in the cold state ranges from 50 to 200 eV. Thus, the energy loss in the plasma exceeds that in cold matter.

To derive a stopping power model for plasma, a final correction must be made. Specifically, the thermal correction must be added when considering projectile ion velocities near or below the thermal velocity of the free plasma electrons v_{th}. The adapted Bethe formalism, with the Bloch and Barkas corrections, diverges for low velocities. To account for this, a correction function called the Chandrasekhar function (Spitzer Jr. 1956) is introduced and expressed as:

$$G(x) = \text{erf}\left(\frac{x}{\sqrt{2}}\right) - \sqrt{\frac{2}{\pi}} x \exp(-x^2/2). \tag{2.24}$$

Here, erf is the error function and x is substituted with $\frac{v_p}{v_{\text{th}}}$. The Bethe formula is modified by $G\left(\frac{v_p}{v_{\text{th}}}\right)$ to account for the distribution of velocities resulting from the thermal energy of electrons in the target. This is especially important at lower projectile speeds, where the relative motion between the electrons and

the projectile can significantly affect the energy transfer process. The function is derived from statistical mechanics and considers a Maxwellian distribution of electron velocities in the target material.

The Bethe formula can be applied to the entire velocity spectrum once all corrections have been incorporated. The resulting expression is known as the **Standard Stopping Model (SSM)**, which has been utilized to interpret numerous experiments:

$$\frac{dE}{dx}_{\text{free}} = -\frac{Z_{\text{p}}^2 e^2 \omega_{\text{p}}^2}{v_{\text{p}}^2} G\left(\frac{v_{\text{p}}}{v_{\text{th}}}\right) \left(\mathcal{L}_{\text{Bethe, free}} + \mathcal{L}_{\text{Bloch}} + \mathcal{L}_{\text{Barkas}}\right). \tag{2.25}$$

For high projectile velocities, the Bloch, Barkas, and thermal corrections become negligible. The SSM is a phenomenological model based on a stopping formulation in cold matter with corrections for the plasma case. At high projectile velocities, the method is accurate, but it is inappropriate to use it around the stopping maximum. It is not expected to predict correct stopping results in the stopping maximum. Equation 2.25 was implemented for theoretical predictions.

A basic description of the stopping power of ions in plasma has been presented. The following section addresses a theoretical description of the stopping power, depending on the plasma and beam-plasma parameters. Based on this, more advanced theoretical approaches are presented.

2.2.3 Beam Plasma Interaction

The following sections are primarily derived from Günter Zwicknagel et al. 1999. The stopping power of ions in plasma is typically described theoretically using two parameter scales. The first is the regime of ion-plasma interaction, which is determined by the strength of the beam plasma correlations. The impact parameter domain is the second parameter scale, which distinguishes between short-range collisions, such as elastic or inelastic Coulomb scattering, and long-range collective effects, such as plasmon excitation, plasma polarization, and dynamic screening. This section explains the first parameter scale, which refers to the interaction between ions and plasma, and defines the different regimes of this interaction.
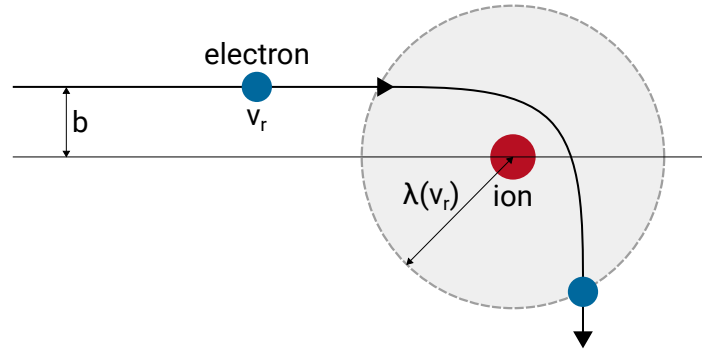

Figure 2.1: Schematic overview of the projectile-plasma interaction. A plasma electron with a thermal velocity of v_{th} is scattered by a projectile ion with a velocity of v_{p} and a charge state of Z_{p} at an impact parameter of b. v_{r} represents the relative velocity between the projectile and plasma electron.

A schematic overview of the interaction between a projectile ion and a free plasma electron is depicted in Figure 2.1. The ion has a velocity of v_{p} and a charge state of Z_{p}. The plasma has an electron temperature of T_{e}, and the electrons have a thermal velocity of v_{th}. The De Broglie wavelength (see Equation 2.7)

associated with this interaction is $\lambda_r = \frac{\hbar}{m_e v_r}$ with the relative velocity between the projectile and the plasma electrons v_r. The De Broglie wavelength describes the distance in plasma under which quantum effects play a dominant role in the interaction. The projectile ion is screened by the plasma electrons, characterized by the velocity-dependent screening length $\lambda(v_r)$ (refer to Section 2.1). The Coulomb scattering process uses the impact parameter, denoted as b. An important parameter is the impact parameter corresponding to a Coulomb deflection of 90°, namely b_0:

$$b_0 = \frac{Z_p e^2}{m_e v_r^2} = r_{i,e} \tag{2.26}$$

It represents the classical distance of minimal approach between the projectile and a free electron and is equivalent to the Landau length (see Equation 2.5).

To describe the transition from the classical to the quantum mechanical regime, a non-dimensional **Coulomb parameter** η is introduced:

$$\eta = \frac{V}{E_{kin}} = \frac{b_0}{\lambda_r} = \frac{Z_p e^2}{\hbar v_r}. \tag{2.27}$$

The Coulomb parameter is the ratio between the potential and kinetic energy of the projectile-electron system with the Coulomb potential between the projectile and the electron at a distance λ_r:

$$V = \frac{Z_p e^2}{\lambda_r} \tag{2.28}$$

and the associated kinetic energy:

$$E_{kin} = m_e v_r^2. \tag{2.29}$$

Therefore the Coulomb parameter measures the strength of the projectile-electron coupling similar to how the coupling parameter Γ (see Equation 2.12) describes the strength of electron-electron coupling. For low charges and high projectile velocities ($\eta \ll 1$), the interaction must be treated quantum mechanically. For higher charges and lower projectile velocities ($\eta > 1$), the interaction can be described classically (Günter Zwicknagel et al. 1999).

For $\eta \ll 1$, the projectile's perturbation on the plasma electron is negligible, and the interaction can be analyzed using perturbative quantum mechanics. This type of ion-plasma interaction is referred to as **linear**. Here, linear is synonymous with perturbative. However, for $\eta \geq 1$, the perturbation induced on the plasma electrons is significant, and the perturbative approach is no longer appropriate. The linear regime corresponds to the Bethe regime (see Equation 2.17), while the Bohr regime (see Equation 2.16) corresponds to a stronger perturbation beyond the linear regime. The Coulomb parameter depends only on the relative velocity v_r and the plasma electron temperature T_e, not the electron density, and therefore has no dependence on the electron-electron coupling Γ. This means that the Coulomb parameter only represents the perturbation on one plasma electron, which is adequate as long as the perturbation stays localized. For significant perturbations, the influence extends beyond the single projectile electron system and affects a spatial zone around the projectile. The plasma screening length λ (refer to Section 2.1) estimates the characteristic length of the perturbation. If λ becomes larger than the De Broglie wavelength λ_r, it must be replaced in the expression of the potential energy (Equation 2.28). This creates a new parameter that describes ion-plasma coupling:

$$\gamma = \frac{b_0}{\lambda}. \tag{2.30}$$

This parameter is called the **nonlinearity parameter** of the interaction. It is defined as the borderline between localized perturbations confined in a region smaller than the screening length, known as the
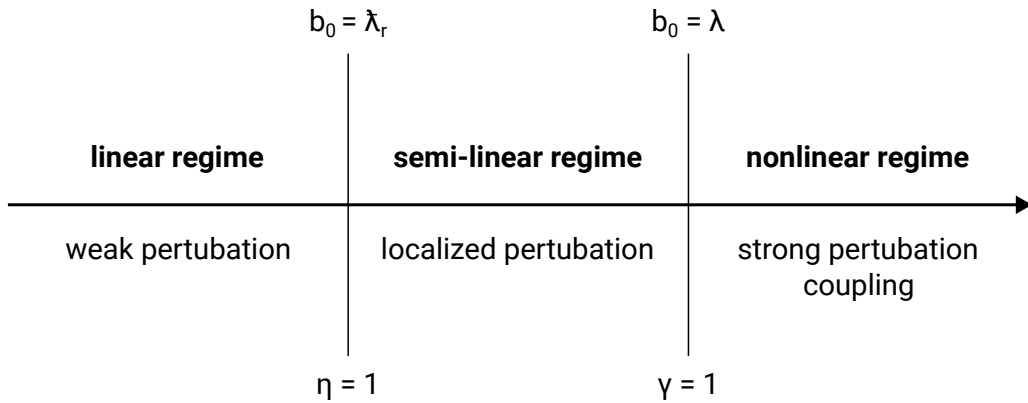
Figure 2.2: Characteristic regimes of the projectile plasma interaction, defined by the Coulomb parameter η and the nonlinearity parameter γ.

semi-linear regime ($\gamma < 1$ and $\eta > 1$), and spatial perturbations in a region larger than the screening length, known as the **nonlinear** regime ($\gamma > 1$). Figure 2.2 illustrates the different regimes.

The distance of minimal approach b_0 (see Equation 2.26) between the projectile and a free electron can be used to characterize different regimes. According to Equations 2.27 and 2.30, $b_0 < \lambda_r$ holds for the linear regime, $\lambda_r < b_0 < \lambda$ holds for the semi-linear regime, and $b_0 > \lambda$ is true for the nonlinear regime.

In the linear regime, a perturbative analysis based on the first Born approximation in the quantum mechanical theoretical framework can be applied, neglecting the perturbation on the target electrons. This is where the Bethe formula becomes relevant. However, when $\eta \approx 1$, the first Born approximation and the Bethe formula lose their validity, and corrections need to be added, as in the SSM. In the semi-linear regime, corrections alone are insufficient for perturbative approaches to succeed when $\eta \geq 1$. More advanced theoretical models are necessary, especially in the nonlinear regime where strong coupling effects must be considered.

It is important to consider each regime of interaction for various impact parameters since all impact parameters contribute to the stopping process. The impact parameter is statistically larger in ideal plasmas than in nonideal plasmas. However, a comprehensive description of the stopping power is still necessary. Both linear and nonlinear effects as well as short-range and long-range projectile-electron encounters must be taken into account. Currently, each parameter region has its own model, and unifying all of these parameter ranges within one theory remains a significant challenge.

2.3 Theoretical Models for Stopping Power of Ions in Plasma

This section discusses various approaches to the stopping of ions by free electrons and a brief overview of models for stopping by bound electrons. Finally, theoretical models for the charge state of the projectile in the plasma are presented.

2.3.1 Stopping Power for Free Electrons

First, this section presents different approaches to ion stopping by free electrons, depending on the range of impact parameters, which is the second parameter scale mentioned in Section 2.2.3. Then, combined approaches are presented to provide a complete description of the stopping power.

Impact Parameter Dependant Approaches

At low projectile velocity, binary collisions are the predominant factor, while at high projectile velocity, collective effects become more important due to a lower-coupled regime. It is important to take into account both close collisions and collective effects around the stopping maximum.

Long-range interactions or collective effects in plasmas include plasmon excitation, dynamic screening, and plasma polarization. Dynamic screening refers to the velocity-dependent screening of the projectile charge by the surrounding plasma electrons, which results in a lower ionization energy of the projectile at higher velocities (Nardi et al. 2009). Plasma polarization describes the local modification of the electron density in the vicinity of the projectile ion and corresponds to the Barkas term (see Equation 2.19) in the Bethe formula (see Equation 2.25). To describe these effects, a formalism that incorporates the necessary many-body physics must be used. The linear response approach is based on a continuous medium description that utilizes a dielectric function. The projectile ion generates an electrostatic perturbation on the plasma target, which in turn generates an electric potential on the ion that corresponds to the stopping force. The stopping power is proportional to Z_p^2 in this frame due to the linear response by the target. If the dielectric function of the target material is available and the projectile potential can be treated as a small perturbation, the dielectric formalism can be applied. Therefore, this approach cannot account for nonlinear (refer to Section 2.2.3) collective effects.

To describe close collisions, a particle-oriented approach is used instead of a medium-oriented approach. The stopping power is the accumulation of energy transfers from binary ion-electron collisions, averaged over all possible scattering events and relative velocities.

These approaches are limited to either collective effects or close collisions. Modifying the dielectric function of the medium can be attempted to include close collisions in the dielectric linear response approach (Barriga-Carrasco 2010). Additionally, collective effects can be artificially added to the binary collision approach by selecting an appropriate ion-electron effective interaction potential.

In the context of kinetic plasma theory, it is possible to generalize. Each species of plasma particle is described by a different distribution function, $f(r, v, t)$, in this theory. The temporal evolution of each species is determined by a kinetic equation. These kinetic equations are then combined with the Maxwell

equations. When considering only the mean electromagnetic fields, the plasma is collisionless. The kinetic equation that describes a given species in the plasma is a Vlasov kinetic equation:

$$\frac{\partial f}{\partial t} + \vec{v} \cdot \frac{\partial f}{\partial \vec{r}} + \frac{q}{m}\left(\vec{E} + \vec{v} \times \vec{B}\right)\frac{\partial f}{\partial \vec{v}} = 0 \tag{2.31}$$

where q is the particle charge and $\vec{E}$ and $\vec{B}$ are the electric and magnetic field respectively. To introduce collisions into the Vlasov description, collision integrals I_c must be added to the right side. For a homogeneous plasma without external fields, the kinetic equation of the ion beam in plasma can be written as:

$$\frac{\partial f}{\partial t} = \sum_c I_c. \tag{2.32}$$

The collision integrals, represented by I_c, describe the interaction between the beam's projectile ions and the plasma species c. This only encompasses collisions with the plasma electrons in this case. The stopping power is given by:

$$\frac{dE}{dx} = \frac{1}{n_e}\int \frac{dp}{(2\pi\hbar)^3}\frac{\vec{p}\cdot\vec{v}}{v}\frac{\partial f}{\partial t} \tag{2.33}$$

where $\vec{p}$ and $\vec{v}$ are the projectile velocity and momentum. There are various approximations for the collision integrals, which are presented below.

The **Lenard-Balescu** collision integral is derived using the Random Phase Approximation (**RPA**) (Balescu 1960; Lenard 1960). The RPA dielectric function enables a description of collective effects, as well as soft to moderate close collisions. The Lenard-Balescu stopping power is calculated in the first Born approximation and is therefore limited to the linear regime of the beam-plasma interaction (refer to Section 2.2.3). It is also referred to as the Born-RPA stopping power and is expressed as follows:

$$\frac{dE}{dx} = -\frac{2Z_p^2 e^2}{\pi v_p^2}\int_0^\infty \frac{dk}{k}\int_{\frac{\hbar k^2}{2me}-kv}^{\frac{\hbar k^2}{2me}+kv} d\omega \left(\omega - \frac{\hbar k^2}{2me}\right)\mathrm{Im}\left(\frac{1}{\epsilon_{\mathrm{RPA}}}(k,\omega)\right)n_B(\omega) \tag{2.34}$$

where k and ω are the wave number and circular frequency of the scattered wave of the projectile ion. The RPA dielectric plasma function is represented by ϵ_{RPA} and the Bose distribution function of the plasmons is represented by n_B. This description applies to linear ion plasma interactions in an ideal plasma. To calculate the RPA stopping power, a parameterization by Zimmerman 1997 was used.

The simplified **linear Vlasov** stopping power results from neglecting plasma collisions in the Born-RPA description (Peter et al. 1991a):

$$\frac{dE}{dx} = -\frac{2Z_p^2 e^2 \omega_p^2}{v_p^2}\left[G\left(\frac{v_p}{v_{th}}\right)\ln\left(\frac{\lambda_D}{b_0}\right) + H\left(\frac{v_p}{v_{th}}\right)\ln\left(\frac{v_p}{v_{th}}\right)\right]. \tag{2.35}$$

Here G is the Chandresekhar function (see Equation 2.24) and H is approximated by:

$$H(v) \approx -\frac{v^3}{3\sqrt{2\pi}\ln v}e^{-\frac{v^2}{2}} + \frac{v^4}{v^4 + 12}. \tag{2.36}$$

Both the Lenard-Balescu (RPA) and linear Vlasov stopping powers can be simplified to the Bethe formula for high velocities. Equation 2.35 is used for calculations in Chapter 4.

To describe short-range interactions between projectile ions and plasma electrons, a Boltzmann collision integral is utilized. The integral is derived using a binary collision approximation in the general kinetic

equation. This scheme is implemented with a transport matrix (**T-Matrix**) used to calculate the cross sections of Coulomb interactions in the Lippmann-Schwinger equation. The T-Matrix stopping power is given by (D. O. Gericke et al. 1999; Morawetz et al. 1996):

$$\frac{dE}{dx} = -\frac{m_e}{\mu^3}\frac{n_e\lambda_e^3}{(2\pi)^2\hbar^3}\frac{k_BT_e}{v_p}\int_0^\infty dp\,p^3 Q_{pe}^T(p)\cdot\left[p_-\exp\left(-\frac{m_ev_-^2}{2k_BT_e}\right) - p_+\exp\left(-\frac{m_ev_+^2}{2k_BT_e}\right)\right] \qquad (2.37)$$

with $p_\pm = 1 \pm \frac{\mu k_BT_e}{m_epv_p}$ and $v_\pm = \frac{p}{\mu} \pm v_p$, where p is the projectile momentum. $Q_{pe}^T(p)$ represents the transport cross section of the scattering process between the projectile ions and the electrons. The T-Matrix calculations are limited to a statically screened Coulomb potential of the projectile, disregarding collective plasma effects. Unlike Lenard-Balescu, the T-Matrix formalism is a nonlinear description (refer to Section 2.2.3) with no limitations on the coupling strength.

If only the first Born approximation is considered in the transport cross section $Q_{pe}^T(p)$, the **Landau** collision integral is derived (D. O. Gericke et al. 1999; Morawetz et al. 1996). The Landau equation is a perturbative stopping power description dealing with binary collisions in the static screening case. It is valid only for intermediate impact parameters and cannot deal with collective effects and strong collisions.

All of the presented approaches are summarized in Figure 2.3, which shows their range of validity in the impact parameter frame.
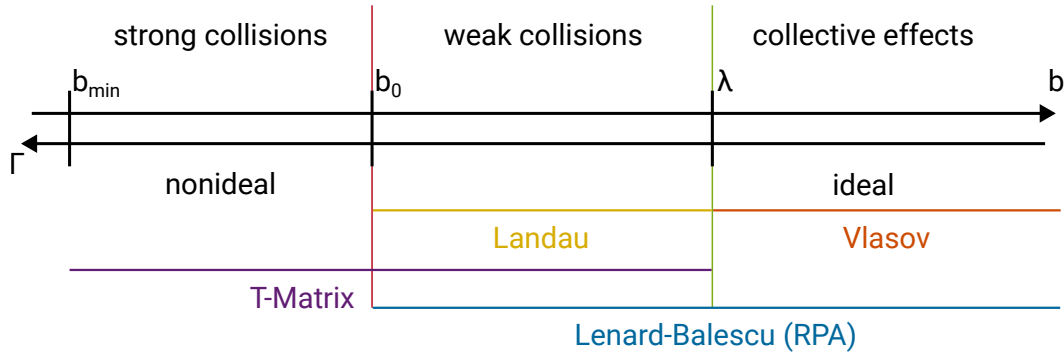

Figure 2.3: T-Matrix, Landau, RPA and Vlasov approaches shown in the impact parameter space.

Unified Stopping Power Descriptions

To obtain a comprehensive description of the energy loss required in the region of the stopping maximum ($v_p \approx v_{th}$), the contributions of short-range and long-range effects must be taken into account. There are several approaches to such descriptions.

The **Gould-DeWitt scheme** or combined scheme sums the collision integrals in the frame of kinetic theory, accounting for both short and long-range interactions, to determine the stopping power (Gould et al. 1967):

$$\frac{dE}{dx} = \frac{dE}{dx}^{\text{T-Matrix}} + \frac{dE}{dx}^{\text{RPA}} - \frac{dE}{dx}^{\text{Landau}}. \qquad (2.38)$$

The Lenard-Balescu (RPA) stopping power ($b \geq b_0$) is supplemented with the T-Matrix stopping power ($b \leq \lambda$). To account for the intermediate regime appearing twice (see Figure 2.3), the Landau stopping is subtracted ($b_0 \geq b \geq \lambda$). More elaborate schemes have been proposed based on this idea, including some presented in D. Gericke et al. 1996; Morawetz et al. 1996 and Gilles Maynard et al. 2001.

The **T-Matrix with** $\lambda(v)$ incorporates dynamic shielding using a velocity-dependent screening length $\lambda(v_{\mathrm{p}})$ (refer to Section 2.1), thereby adding a description of collective plasma effects to the T-Matrix formalism (D. O. Gericke et al. 2003, 2002; Günter Zwicknagel et al. 1999). The screening length $\lambda(v_{\mathrm{p}})$ for nondegenerate plasma was adopted (see Equation 2.11). The transport cross section of Equation 2.37 becomes $Q_{\mathrm{pe}}^{\mathrm{T}}(p, \lambda(v))$. The T-Matrix theory with $\lambda(v)$ is calculated using an approximate fit formula described in GERICKE 2002. This combined scheme, which covers the entire spectrum of impact parameters and is non-perturbative (refer to Section 2.2.3), is expected to accurately describe this physical case.

The **Li-Petrasso** approach adds a collision term and a collective term to the Landau description to expand it (Li et al. 1993a,b):

$$\frac{dE}{dx} = -\frac{Z_{\mathrm{p}}^2 e^2 \omega_{\mathrm{p}}^2}{v_{\mathrm{p}}^2} \left[G^* \left(\left(\frac{v_{\mathrm{p}}}{v_{\mathrm{th}}}\right)^2 \right) \ln\left(\frac{\lambda_{\mathrm{D}}}{b_{\mathrm{min}}}\right) + \Theta\left(\left(\frac{v_{\mathrm{p}}}{v_{\mathrm{th}}}\right)^2 \right) \ln\left(1.123 \frac{v_{\mathrm{p}}}{v_{\mathrm{th}}}\right) \right]. \tag{2.39}$$

Here G^* is a modified version of the Chandrasekhar function (Li et al. 1993a). The logarithmic term, added with the step function Θ, is used to model collective effects. This model is valid for fully ionized plasmas and is used for ICF calculations. Its validity is limited to small perturbations, i.e., the linear regime (refer to Section 2.2.3) of ion-plasma coupling (Günter Zwicknagel et al. 1999). To calculate the Li-Petrasso stopping power, a modified parameterization (A. B. Zylstra et al. 2019b) is used. As close collisions are not significant, the results are expected to be comparable to the RPA and SSM stopping power.

Another theory, known as **BPS** (Brown, Preston, Singleton) (BROWN et al. 2005; Singleton 2008), combines the Lenard-Balescu description with Boltzmann equations to provide results for linear coupling in highly ionized plasmas. This approach is valid only for ideal plasmas. R. L. Singleton provided a Fortran code for calculating the BPS stopping power.

None of the theories presented so far adequately address strong perturbances and collective effects. **Numerical simulations** can be used to describe parameter ranges beyond the scope of existing theories. Particle in Cell (**PIC**) simulations can solve the Vlasov-Poisson (**VP**) equations (Boine-Frankenheim 1996; Peter et al. 1991a; Günter Zwicknagel et al. 1999) and are suitable for this purpose (D'Avanzo et al. 1998). These simulations are effective for collective effects, such as ideal plasmas, and weak collision modules (Sentoku et al. 2008) can be added. The validity of the simulations coincides with the semi-linear regime (refer to Section 2.2.3). To include strong collisions, Molecular Dynamic (**MD**) simulations must be performed (Allen et al. 2017; G. Zwicknagel et al. 1997). These simulations have no restrictions on the ideality of the plasma. When leaving the nonlinear regime and entering the regime where the Bethe formula (see Equation 2.15) is valid, computation becomes impossible.

The validity ranges of the various theoretical approaches to energy loss are summarized schematically in Figure 2.4 as a function of the ion-plasma coupling and the impact parameter.

All of these approaches describe the stopping power of free plasma electrons. However, they only accurately describe the stopping power for highly ionized plasmas. Although the stopping power of free electrons is much higher, the stopping power of bound electrons cannot be neglected.
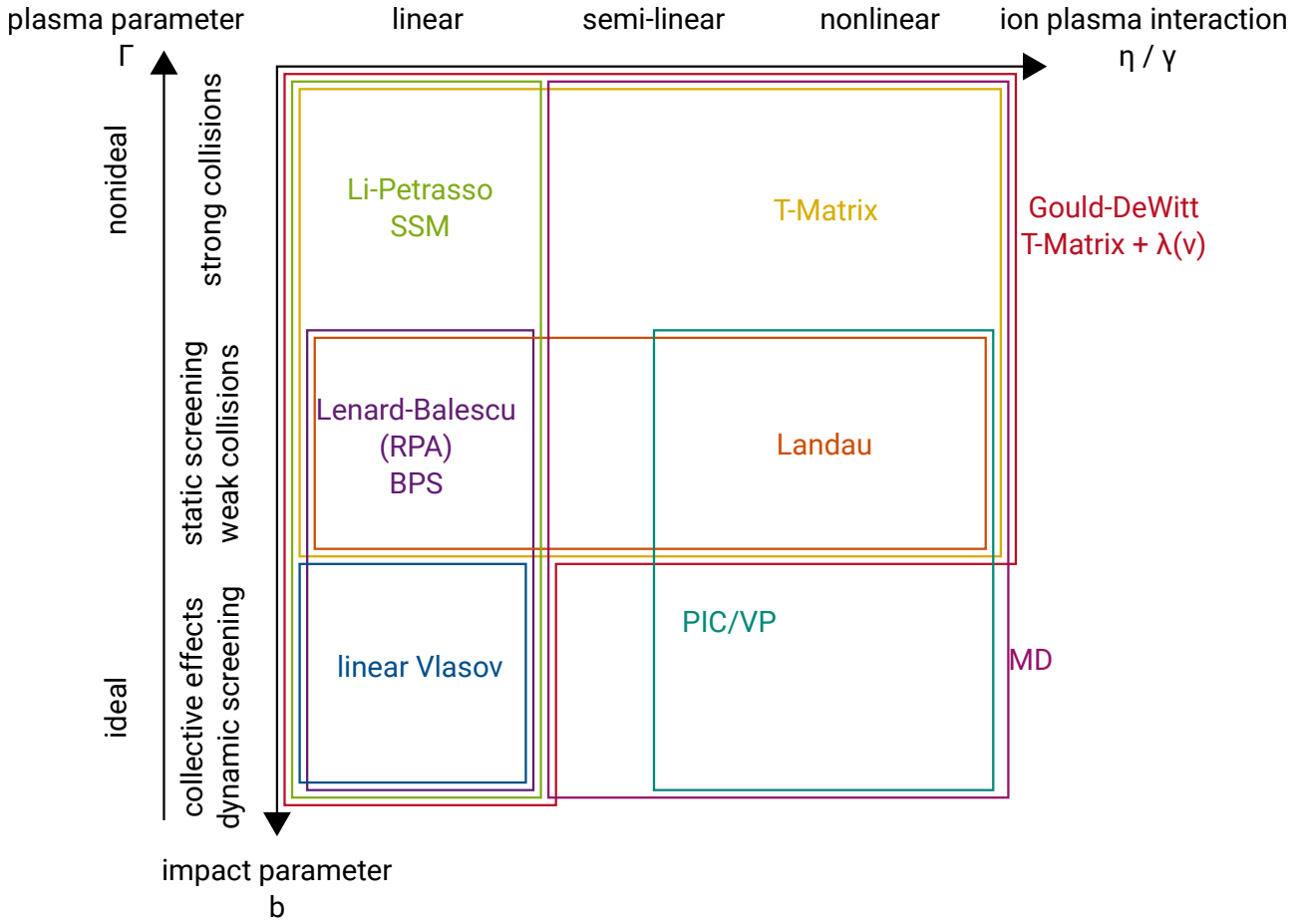
Figure 2.4: Overview of the validity of the presented stopping power theories in the impact parameter and linearity space.

2.3.2 Stopping Power for Bound Electrons

If the plasma is not fully ionized, the bound electrons contribute to the stopping power of ions.

To account for the stopping of bound electrons, the Bethe formula (see Equation 2.15) can be used by summing up the contribution of each single plasma ion charge state that contains bound electrons. It is important to note that the Bethe formula is only valid for high projectile velocities.

To account for low velocities, another stopping model presented in Barriga-Carrasco et al. 2005 and Casas et al. 2013 can be used. Analytical formulas were used to interpolate an expression for intermediate velocities, based on the limit of low and high projectile velocities. The Coulomb logarithm is calculated separately for each shell:

$$\mathcal{L}_{\text{bound}} = \begin{cases} \ln\left(\dfrac{2v_p}{\bar{I}}\right) - \dfrac{2E_{\text{kin,e}}}{v^2} & v > v_{\text{int}} \\ \dfrac{\alpha v^3}{1 + Gv^2} & v \le v_{\text{int}} \end{cases} \tag{2.40}$$

with $v_{\text{int}} = \sqrt{3E_{\text{kin,e}} + 1.5\bar{I}}$. G is given by $\mathcal{L}_{\text{bound}}(v_{\text{int}})$ where both cases need to be equal. Here, $E_{\text{kin,e}}$ represents the electron kinetic energy, $\bar{I}$ represents the mean excitation energy, and α represents the friction

coefficient, which can be approximated by $\alpha = 1.067\sqrt{E_{kin,e}}/\bar{I}$. For the calculations in Chapter 4, the values of $E_{kin,e}$ and $\bar{I}$ for the carbon plasma are sourced from Casas et al. 2013. There, the mean excitation energies $\bar{I}$ are determined on the assumption that the ions are not affected by the environment. In reality, the plasma density and plasma temperature can change the population and energies of its atomic levels. To account for these effects, a lower potential must be used, where $\bar{I}$ is reduced by the Coulomb potential of surrounding ions (Stewart et al. 1966).

2.3.3 Charge State Estimation of Ions in Plasma

The investigation of the evolution of the projectile charge state while traveling through a plasma is crucial due to the dependence of the stopping power of ions on the projectile charge state. The distribution of charge states in an ion beam interacting with a plasma differs from that in cold matter (refer to Section 2.2.1). The presence of free electrons not only alters the cross sections for ionization and recombination but also enables new ionization and recombination processes.

The cross section for ionization by Coulomb collision with target ions is enhanced due to the reduced screening of the electrical potential of the target ions by bound electrons. In a fully ionized plasma, the cross section of REC surpasses that of NREC. REC's cross section increases with the presence of more free electrons that can be captured, while NREC's cross section decreases with the lower number of bound electrons in the inner shell, which are the dominant contributions to NREC.

Additionally, ionization by free plasma electrons occurs in a plasma. To occur, there must be a sufficiently high relative velocity between the projectile and the free electron. Therefore, a higher plasma temperature increases the probability of this process. Dielectronic recombination occurs when the excess energy from the capture of a free electron by the projectile is not converted into radiation but instead transferred to a bound electron, exciting it in the process. This process occurs only when the excess energy is equal to the excitation energy of the electron. The excited state decays by emitting a photon or ejecting a secondary electron from the ion in an Auger process. In the latter case, no recombination occurs in totality. The dielectronic recombination dominates in hot, highly ionized plasmas (Peter et al. 1991b), while the three-body recombination becomes significant in dense plasmas. In this scenario, a third free electron is present in the vicinity during the recombination with a free electron. The third electron serves as a third collision partner, ensuring momentum and energy conservation. Despite being present in very dense plasmas, the cross section for this recombination process is significantly smaller than that of other processes. Due to the reduced cross section of NREC and the increased cross section of ionization by Coulomb collision with the target atoms, the equilibrium charge state of the projectile Z_{eq} increases in relation to cold matter (K.-G. Dietrich et al. 1992; Nardi et al. 1982).

Equlibrium Charge State

Similarly to the cold matter case (see Section 2.2.1), semi-empirical models are used to calculate the equilibrium charge state. The **Kreussler** model (Kreussler et al. 1981) is based on the equilibrium charge state model in solid targets by Northcliffe 1960 (refer to Equation 2.21). The equilibrium charge state, according to Kreussler, is provided as follows:

$$\frac{Z_{eq}}{Z_{an}} = 1 - \exp\left(-v_r/Z_{an}^{2/3}v_0\right) \tag{2.41}$$

where v_r is the relative velocity between the projectile and the plasma electrons and Z_{an} represents the atomic number of the projectile ion. In the Thomas-Fermi model, $Z_{an}^{2/3} v_0$ represents the velocity of the electrons that are bound to the projectile.

Gus'kov et al. 2009 developed a similar model based on Ziegler's semi-empirical model for a solid target (James F. Ziegler et al. 1985). The **Gus'kov** model estimates the equilibrium charge state as follows:

$$\frac{Z_{eq}}{Z_{an}} = 1 - \exp\left(-0.92\left[(v^*)^2 + \frac{3}{5}T^*\left(\frac{E_F}{k_B T} + \frac{5\pi^2/12}{\frac{E_F}{k_B T} + \pi^2/6}\right)\right]^{1/2}\right) \tag{2.42}$$

where $v^* = v_p/v_0 Z_{an}^{2/3}$ and $T^* = k_B T/E_0 Z_{an}^{4/3}$ are the projectile velocity and the plasma temperature normalized to the characteristic velocity of electrons in the Thomas-Fermi atom. E_F is the Fermi energy and $E_0 = 13.6\,\text{eV}$ is the Bohr binding energy.

Nonequlibrium Charge State

While in cold matter the characteristic timescale of the charge transfer processes is well below the timescale of the stopping process, in a highly ionized plasma the characteristic time of the charge transfer is increased and is on the same level as the timescale of the stopping process. This is mainly due to the decreased cross section of the NREC mechanism. Therefore, the projectile may not always reach its equilibrium charge state (Peter et al. 1991b). There are several ways to account for this non-equilibrium charge state.

In Morales 2022, a model was proposed to estimate the dynamic evolution of the projectile charge derived from the semi-empirical framework. The model describes an ion with an initial charge state Z_0 traveling a distance x with velocity v_p in a plasma with a free electron density n_e and predicts a non-equilibrium charge state:

$$Z_{neq} = Z_{eq} - (Z_{eq} - Z_0)\exp\left(-\frac{x}{\lambda_{ion}}\right) \tag{2.43}$$

with the equilibrium charge state Z_{eq} and the ionization length:

$$\lambda_{ion} = \frac{v_p}{n_e \alpha_{ion}}. \tag{2.44}$$

An estimation of the typical ionization rate was calculated using the ionization cross sections in plasma: $\alpha_{ion} \approx 5 \times 10^{-10}\,\text{cm}^3/\text{s}$. This model is used in conjunction with either the Kreussler model (refer to Equation 2.41) or the Gus'kov model (refer to Equation 2.42).

Morales 2022 also presented a more elaborate cross-sectional model (CSM). It uses the charge-exchange cross sections of the ionization and recombination processes in a plasma to calculate the mean charge state of the projectile ions. Various factors that affect these cross sections were taken into account, including the density effect (refer to Section 2.2.1).

The different non-equilibrium charge state models were compared with the results of five different experiments with different parameter ranges (Morales 2022). As a general result, the CSM code is in good agreement with all the experiments analyzed, whereas the nonequilibrium Kreussler and the Gus'kov models predict results close to data but their applicability is limited to stopping power calculations; that is, they are less accurate for a precise charge-state prediction, but they are sufficiently accurate for a reasonable energy-loss calculation at intermediate and low projectile velocities. The results support the use of the

nonequilibrium Kreussler model for energy loss calculations at intermediate velocities ($1 \lesssim v_\mathrm{p}/v_\mathrm{th} \lesssim 10$) and the nonequilibrium Gus'kov model for predictions at low projectile velocities ($v_\mathrm{p}/v_\mathrm{th} \lesssim 1$) (Morales 2022). The CSM framework is a complex and computationally intensive model that is more time-consuming than semi-empirical models and the nonequilibrium Gus'kov model. However, the Gus'kov model with the nonequilibrium extension is in good agreement with previous experiments with similar parameters. Therefore, this work employs the Gus'kov model with the nonequilibrium extension to calculate the projectile ion charge state.

This chapter presented theoretical models for modeling the stopping power of an ion beam in a plasma with given parameters. The next chapter will present a planned stopping power experiment to benchmark these different theoretical models. Chapter 4 will present the modeling of the planned experiment using the presented theoretical models.

3 Planned Stopping Power Experiment with the LIGHT Beamline

The upcoming chapter outlines my proposed experiment on the energy loss of laser-accelerated ions in a laser-generated plasma. The experiment will be conducted as part of the LIGHT project in the Z6 experimental area at Helmholtzzentrum für Schwerionenforschung (GSI).

Firstly, two different approaches of recent stopping power experiments are presented (refer to Section 3.1) before the methodology of this work is outlined (refer to Section 3.2). Then a brief overview of the experiment is given. The following sections explain the LIGHT beamline and the generation of the plasma target using the Nanosecond High Energy Laser for Ion eXperiments (nhelix). Additionally, a diagnostic is included to characterize the plasma.

3.1 State of the Art

This section presents two stopping power experiments. The first experiment was conducted at GSI using ions generated by a linear accelerator. The second experiment involved laser-generated ions. The purpose of this section is to illustrate the typical procedures and difficulties of current energy loss experiments in plasma and to place this work in the context of current research.

3.1.1 Previous Stopping Power Experiment with a Linear Accelerator

Most of the experiments mentioned in Section 1.2 used conventional particle accelerators, such as the one conducted by W. Cayzac et al. 2017 (refer to Figure 3.1). In this experiment, nitrogen ions were accelerated to an energy of 3.6 MeV/u using the UNIversal Linear ACcelerator (UNILAC) at GSI. To reduce the transverse size of the beam, a pinhole with a diameter of 0.5 mm was used. This ensured that the ion beam interacted exclusively with the innermost region of the plasma, where it exhibited a high degree of transverse homogeneity. The ions are decelerated by passing through a degrader foil to match the velocity of the thermal plasma electrons. This elongates the temporal bunch width due to straggling. The final ion beam had an energy of 0.6 MeV/u and was delivered in bunches lasting a full width half maximum (FWHM) of $\tau = 5.5$ ns with approximately 1000 ions per bunch. These ions probed a carbon plasma generated by two nanosecond lasers, namely the Petawatt High Energy Laser for Ion eXperiments (PHELIX) and the Nanosecond High Energy Laser for Ion eXperiments (nhelix). Random phase plates (RPP) generated smooth laser focal spots with a diameter of 1 mm, which ensured a high degree of transverse homogeneity of the plasma in the innermost part of the plasma where the ions passed. The plasma was characterized through the use of interferometric measurements of the free electron density and hydrodynamic simulations. The free electron density was observed to reach a maximum of $n_{e,max} = 5 \times 10^{20}$ cm^{-3}, while the maximum
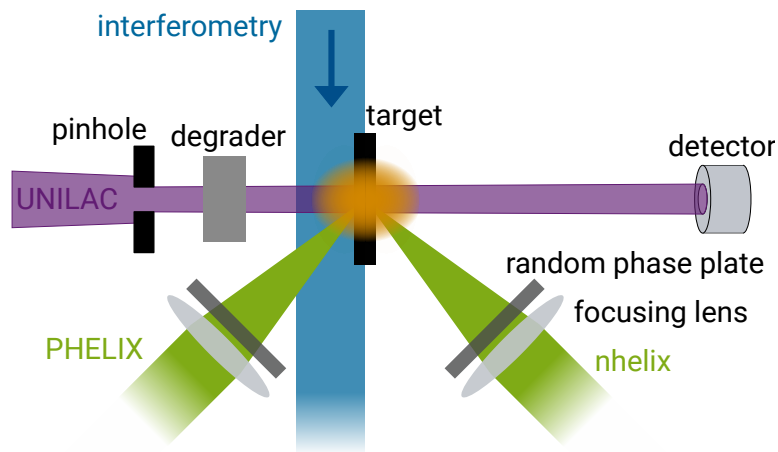
Figure 3.1: Schematic illustration of the previous stopping power experiment conducted by W. Cayzac et al. 2017.

temperature was recorded at $T_{\mathrm{max}} = 150\,\mathrm{eV}$. (W. Cayzac et al. 2015; A. Frank et al. 2013). These parameters result in projectile ion velocities close to the stopping maximum, where their velocity is close to the thermal velocity of the plasma electrons ($v_{\mathrm{p}} \approx v_{\mathrm{th}}$). The discrepancies between the theoretical models are highest at this point (W. Cayzac et al. 2015). The energy was measured using a diamond detector and the time of flight (ToF) method. The time difference between the initial ions and the ions slowed down by the plasma was used to determine the energy loss. The energy loss during plasma expansion was measured at various times, as shown in Figure 3.2. The data is normalized to the energy loss through the solid target. The energy loss in plasma is increased by up to 150 % compared to the solid state. This is due to a more efficient momentum transfer of the projectile ions to the plasma free electrons, as well as an increase in the beam charge state.
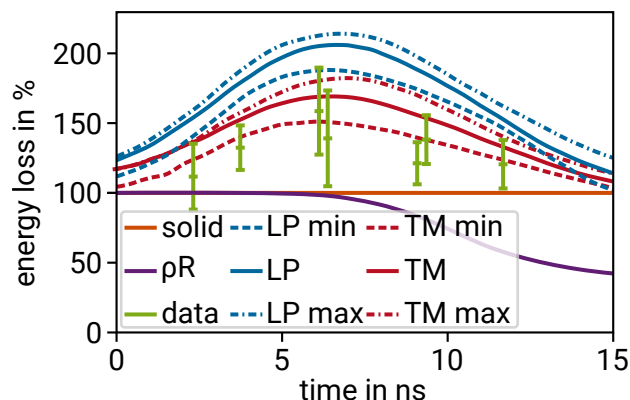

Figure 3.2: Measured energy loss compared with theoretical calculations using the Li-Petrasso (LP) and T-Matrix with $\lambda(v)$ (TM) models. The dashed and dotted dashed lines show the maximum error in the energy loss calculation due to uncertainties in the plasma parameters. Figure adapted from W. Cayzac et al. 2017.

In Figure 3.2, the data is compared with the predictions of the Li-Petrasso (LP) (Li et al. 1993a) stopping model (see Equation 2.39), which represents the standard stopping approaches and yields similar results (W. Cayzac et al. 2015) to the SSM (see Equation 2.25) or the dielectric approaches (refer to Chapter 2). Furthermore, this study also compares the T-Matrix formulation that employs a velocity-dependent screening length (TM) (D. O. Gericke et al. 2003), which includes a detailed treatment of close binary collisions as well as quantum diffraction effects, to the data. The results show that the T-Matrix with $\lambda(v)$ formalism (TM) cannot be excluded. On the other hand, the Li-Petrasso model (LP), and other perturbative models, overestimate the energy loss by 20–25 %.

Although the experiment was successful, the results showed significant temporal uncertainties due to the 5.5 ns ion bunch length used. The plasma parameters underwent rapid changes on the nanosecond timescale as shown in Figure 3.3, which displays simulated temperature profiles at various times during the expansion. Consequently, the leading ions within the probing ion bunch encounter different plasma conditions than the trailing ions, resulting in temporal uncertainties.
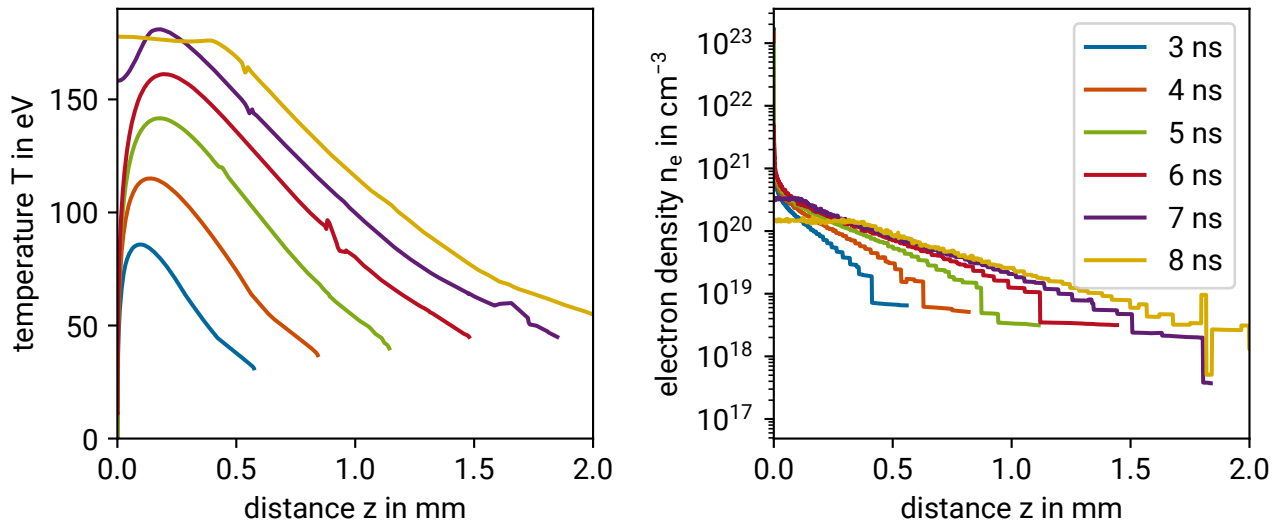

Figure 3.3: Two-dimensional hydrodynamic simulations of a laser-generated plasma conducted with MULTI2D (Ramis et al. 2009) along the laser axis z: a carbon foil with an areal density of 100 µg/cm^2 is irradiated by two lasers beams from both sides (right side of the expansion is shown) with a pulse length of 7 ns (FWHM), a wavelength of 526.5 nm, a focal spot size of 1 mm (supergauss) and energy of 30 J each. The left-hand side displays the simulated plasma temperature at different times during the expansion process. On the right, the simulated free electron density in the plasma at different times of the expansion is depicted.

To mitigate this issue, shorter ion bunches can be implemented. One way to achieve this is through the use of laser-generated ions, which have a lower emittance (Cowan et al. 2004). Emittance refers to the volume of the particle beam in the phase space and is an important measure of the manageability and focusability of a particle beam (Edwards et al. 1993). Another important advantage is the increase in the number of ions within a probing bunch, resulting in a higher signal-to-noise ratio. This enables a more accurate measurement of the stopping power. A stopping power experiment with laser-driven projectiles is presented in the following section.

3.1.2 Previous Stopping Power Experiment with a Laser-Accelerator

The laser-generated beams have fundamentally different characteristics from traditional ion sources, which could expand the range of the accelerator's potential for research and applications. Malko et al. 2022 expanded the data set of stopping power experiments in plasma by using ions generated by a laser-driven beamline as a probe beam. These ions have favorable properties for stopping power experiments compared to ions accelerated by traditional linear accelerators. Laser-plasma accelerators can produce intense multi-MeV ion bunches with brief durations on a µm-scale. These beams can deliver ions with energies above 100 MeV (Higginson et al. 2018; Kim et al. 2016; Wagner et al. 2016; T. Ziegler et al. 2024) in picoseconds at the source (Dromey et al. 2016). The target normal sheath acceleration (TNSA) mechanism represents the most researched and frequently used laser-driven ion acceleration technique. This process involves the interaction of a high-intensity laser pulse with a thin target, resulting in the generation of a dense plasma and a sheath of electrons on the target's rear side. This electron sheath then generates a strong electric field, which rapidly accelerates the ions to high velocities (Wilks et al. 2001). However, the initial TNSA beam is not suitable for most applications due to its broad energy spread, large divergence, and the presence of background radiation in the form of electromagnetic pulses (EMP), X-rays, and electrons close to its origin. Nevertheless, it is possible to produce ion bunches from TNSA sources, which are very well suited for stopping power experiments, by the targeted arrangement of magnets and apertures (Apiñaniz et al. 2021). Malko et al. 2022 successfully conducted a stopping power experiment with laser-generated protons by using magnetic filtering for energy selection, taking advantage of the benefits of laser-driven ions.
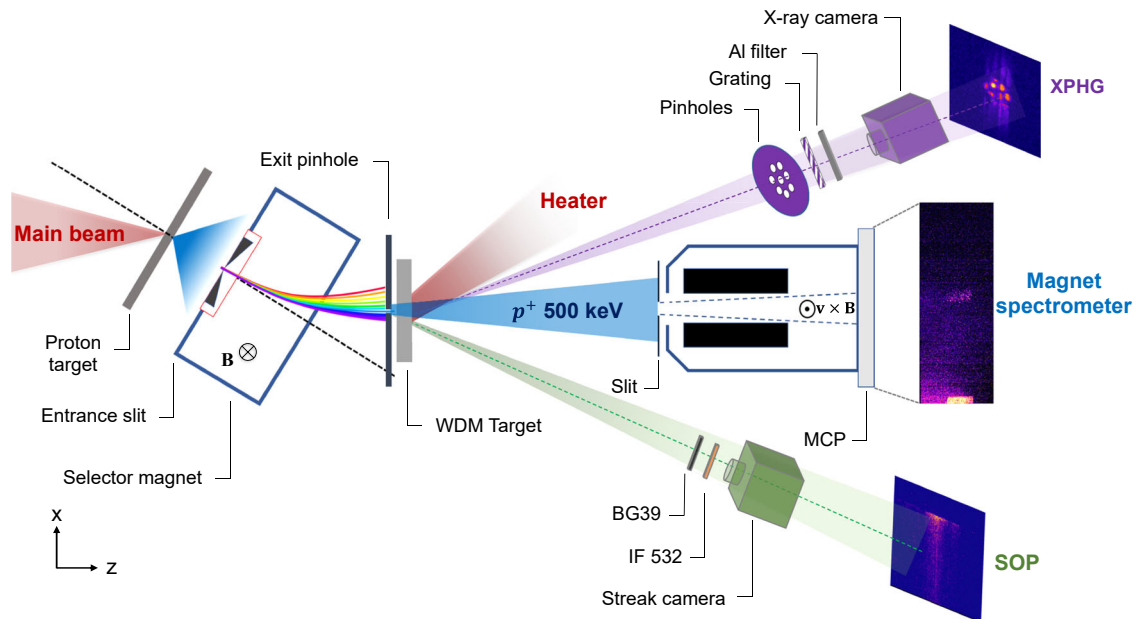

Figure 3.4: Schematic illustration of the previous stopping power experiment conducted by Malko et al. 2022.

The experiment conducted by Malko et al. 2022 took place at the PW-class VEGA laser facility located at the Centro de Láseres Pulsados (CLPU) in Salamanca, Spain. Figure 3.4 displays the experimental setup. The VEGA2 laser was divided into two beams: one for accelerating protons using the TNSA method ($E = 4\,\mathrm{J}, \tau = 30\,\mathrm{fs}$), and the other for creating a warm dense matter (WDM) target ($E = 0.5\,\mathrm{J}, \tau = 200\,\mathrm{fs}$). The WDM state is characterized by densities in the order of or higher than those of the solid state and

temperatures below 100 eV. In this parameter range, the plasma is usually partially ionized, moderately nonideal, and degenerate ($\Gamma \geq 0.1$ and $\Theta \leq 10$). The proton beam was generated by the accelerating beam and had a broadband spectrum with a cutoff energy of approximately 4 MeV. To extract a monoenergetic pencil-like proton beam with an energy of approximately 500 keV from the initial spectrum, a compact magnet-based energy selector (Apiñaniz et al. 2021) was employed. This beam was then used to probe a target sample positioned near the exit of the energy selector, which could be in a solid or WDM state. The proton beam had an energy spread of 44 keV and an estimated bunch length of 400 ps, containing around 1500 protons. A carbon foil was irradiated by the second laser beam to create the WDM target. The WDM target was characterized by temperatures T_e ranging from a few eV to a few tens of eV, with a mass density of $\rho \geq 0.1\,\mathrm{g/cm^3}$ and a velocity ratio v_p/v_{th} ranging between 2 and 10. The energy of the protons was measured using a magnet spectrometer in three different scenarios: without any target, with a solid target, and with the WDM target. Figure 3.5 shows the measured energy loss at different times during the expansion.
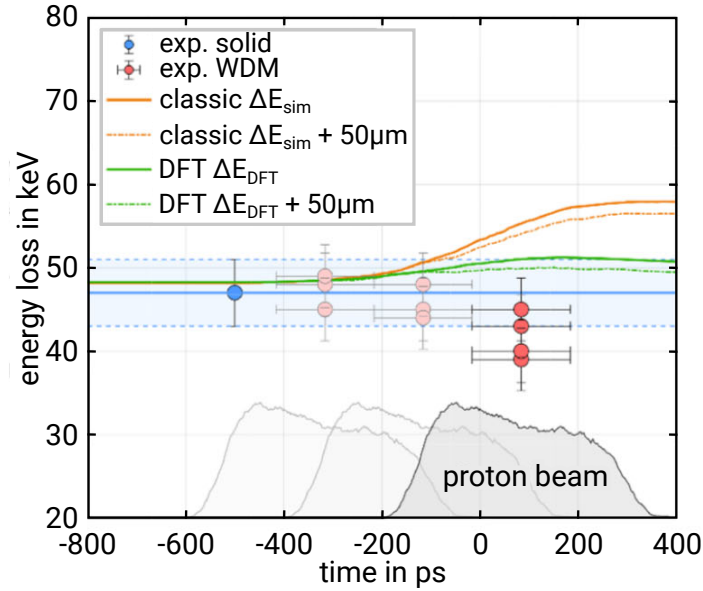

Figure 3.5: Energy-loss data of protons over time. $t = 0$ ps represents the start of the laser beam on the carbon target. The shaded grey profile shows the temporal shape of the probing proton bunch, obtained through a FLUKA Monte-Carlo simulation. The blue solid line displays the average measured energy loss in the solid target, ΔE_{sol}, while the light blue band indicates the error. The energy-loss calculations for classical theories and a time-dependent density functional theory (DFT) are represented by the orange and green curves, respectively. The target was probed by the proton beam along its central axis (solid lines) and with a 50 µm offset (dashed lines). The plot is taken from Malko et al. 2022.

The experimental data is compared to various theoretical models (refer to Chapter 2), including RPA (Zimmerman 1997), Li-Petrasso (Li et al. 1993b) and T-Matrix with $\lambda(v)$ (D. O. Gericke et al. 2003). These models predict similar values and are classified as classical calculations (ΔE_{sim}). Additionally, an approach based on recently developed time-dependent density functional theory (DFT) (White et al. 2020) is also utilized (ΔE_{DFT}). The classical calculations overestimate the energy loss by 40 %, while the DFT approach overestimates it by only 23 %. Therefore, more detailed calculations based on first principles methods, such as density functional theory, are necessary in this stopping regime.

The experimental platform presented here shows promise as a tool for measuring ion stopping power in WDM. It can cover a wide range of proton energies (100 keV and 2 MeV), pulse durations, and target temperatures and densities. However, it is important to note that the number of protons is limited (approximately 1500) and only protons can be used as the projectile ion species at this time (Apiñaniz et al. 2021). An increased number of projectile ions enhances the signal-to-noise ratio, improving the accuracy of the measured stopping power. This work pursues this strategy, and the following section describes the approach for generating an ion beam with the required parameters and an increased number of projectiles.

3.2 Approach for Stopping Power Experiments with the LIGHT Beamline

In contrast to magnetic filtering (Apiñaniz et al. 2021), laboratories around the world are combining laser-driven beamlines with conventional accelerator components such as quadrupoles, magnets and plasma lenses to shape the laser-accelerated ion beam to specific requirements (Brack et al. 2020; Kroll et al. 2022; Rösch et al. 2020; Zhu et al. 2020).
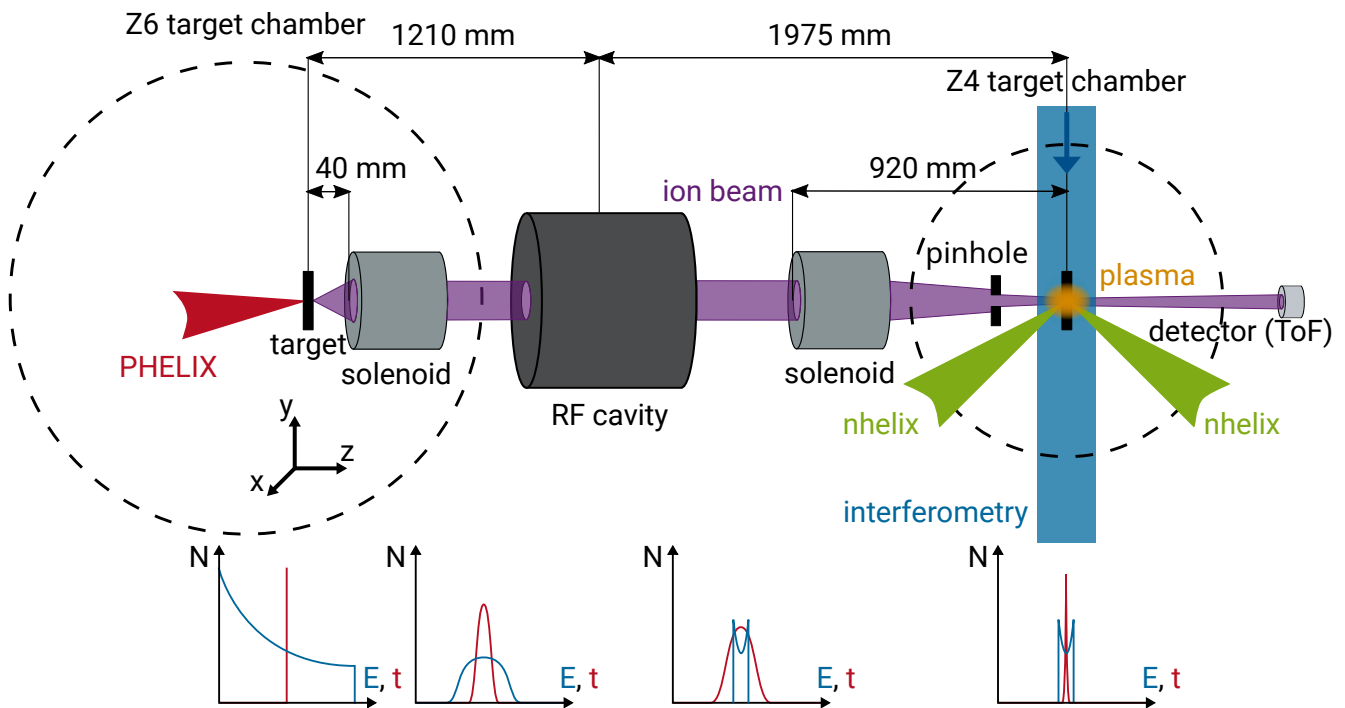

Figure 3.6: Schematic illustration of the planned stopping power experiment with the LIGHT beamline at the Z6 experimental area of GSI. The qualitative distribution of energy and temporal shape of the projectile bunch are illustrated at the TNSA target, after the first solenoid, after the RF cavity, and at the stopping target.

The Laser Ion Generation, Handling and Transport (LIGHT) collaboration (S. Busold et al. 2014b) was established to explore the feasibility of working with laser-driven ion beams using conventional accelerator components. The preexisting infrastructure at GSI allows for the operation of a radio-frequency (RF) cavity, which enables the LIGHT beamline to manipulate the bunches longitudinally. This manipulation can reduce the energy spread of the bunches or compress them temporally (S. Busold et al. 2013, 2014a; Simon Busold et al. 2015; Ikegami et al. 2009; Jahn et al. 2019; Metternich et al. 2022; Teng et al. 2013). The

Helmholtz-Zentrum Dresden-Rossendorf (HZDR) contributes its expertise in high-field solenoid magnets to enhance the transverse focusing and capture efficiency of the LIGHT beamline.

A stopping power experiment is planned to be conducted in the experimental area Z6 at GSI. Figure 3.6 shows the schematic setup of the planned experiment. The objective is to use ions generated with PHELIX and transported with the LIGHT beamline. The bunch will be compressed to the shortest possible length to investigate its stopping power in a laser-generated plasma. The probed plasma, generated with the nhelix laser, will have a maximum temperature of $T_e \approx 180\,\text{eV}$ and a free electron density of $n_e \approx 3 \times 10^{20}\,\text{cm}^{-3}$. To achieve the stopping maximum regime, where the stopping theories differ the most, it is crucial to match the velocity of the probing ions with the thermal plasma electrons (see Figure 3.7). This requires an energy per mass ratio of $0.5\,\text{MeV/u}$ for the ions, which is lower than the typical energy per mass ratio of $8\,\text{MeV/u}$ targeted at the LIGHT beamline (Metternich et al. 2022). In the remainder of this thesis, the z-axis is defined as the axis of the projectile beam, while the x and y axes are defined as the axes of the beam in the transverse plane, with r defined as $r = \sqrt{x^2 + y^2}$.
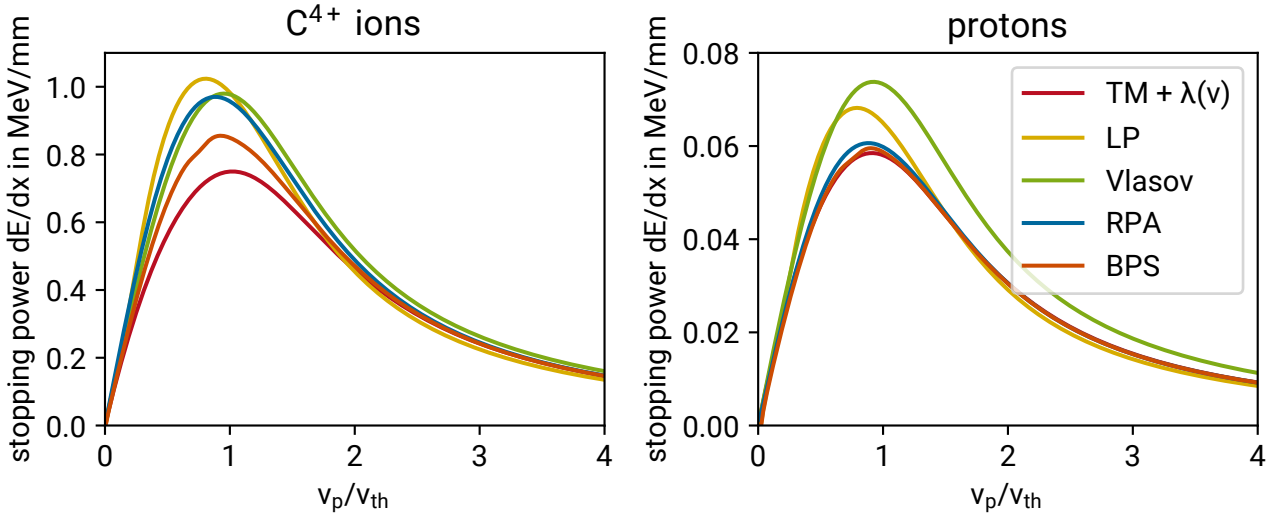

Figure 3.7: Different theoretical models for the stopping of (left) carbon ions (C^{4+}) and (right) protons plotted over the ratio of the projectile velocity to the thermal velocity of the free electrons in the plasma. $TM + \lambda(v)$ is the T-Matrix formalism with $\lambda(v)$, LP is the Li-Petrasso model, Vlasov is the linear Vlasov model, RPA is the Lenard-Balescu Random Phase Approximation and BPS is the Brown Preston Singleton formalism (refer to Chapter 2).

The experiment is planned to be conducted using both carbon ions and protons due to their respective advantages. Carbon ions experience approximately 10–15 times higher energy loss in plasma, as shown on the vertical axis of the plots in Figure 3.7. Furthermore, slow carbon ions are easier to detect using diamond detectors and scintillators due to their higher energy deposition in the detectors. On the other hand, protons have only one charge state, making it unnecessary to estimate their charge state evolution while traveling through the plasma with theoretical models. For carbon ions, the charge state changes within the plasma, requiring theoretical modeling. Therefore, using protons makes modeling the experiment easier. Additionally, different theoretical models behave differently for different species (see Figure 3.7), particularly in the stopping maximum. This effect can be more accurately evaluated by using both carbon ions and protons in stopping power experiments.

3.2.1 The LIGHT Beamline

The planned experiment uses the LIGHT beamline as the source of the ion beam. It combines laser-driven ion beams with conventional accelerator components, including the TNSA source, solenoid magnets, and the RF cavity. The achieved beam parameters have resulted in several publications (S. Busold et al. 2013, 2014a,b; Simon Busold et al. 2015; Jahn et al. 2019; Metternich et al. 2022; Nazary et al. 2024).

This section presents the different components of the LIGHT beamline and briefly explains their functionality.

Laser-Driven Ion Acceleration

The ions are generated and accelerated in the Z6 target chamber via the TNSA mechanism (Gibbon 2005; Macchi 2013; Mulser et al. 2010; Wilks et al. 2001), using the PHELIX laser (Bagnoud et al. 2010). Despite the PHELIX laser's energy being constrained to 40 J at the Z6 experimental area due to the limited aperture available in the laser beamline, its pulse duration of 650 fs (FWHM) and focal spot size of 3.5 μm (FWHM) produce a laser intensity exceeding 10^{19} W/cm^2, which is sufficient to accelerate ions to MeV energies. Different targets are used depending on the desired ion species. The energy spectrum for protons is shown in Figure 3.8 (left). It exponentially decays and has a cutoff energy of 28.4 MeV (S. Busold et al. 2013). The energy-dependent divergence of the protons is illustrated in Figure 3.8 (right). It can be observed that higher-energy protons exhibit a lower divergence. In the vicinity of the cutoff energy, the half-opening angle is approximately 5°, while ions with energies well below the cutoff energy (< 1 MeV/u), which are necessary for this experiment, exhibit high divergences of up to 30° (Simon Busold 2014).
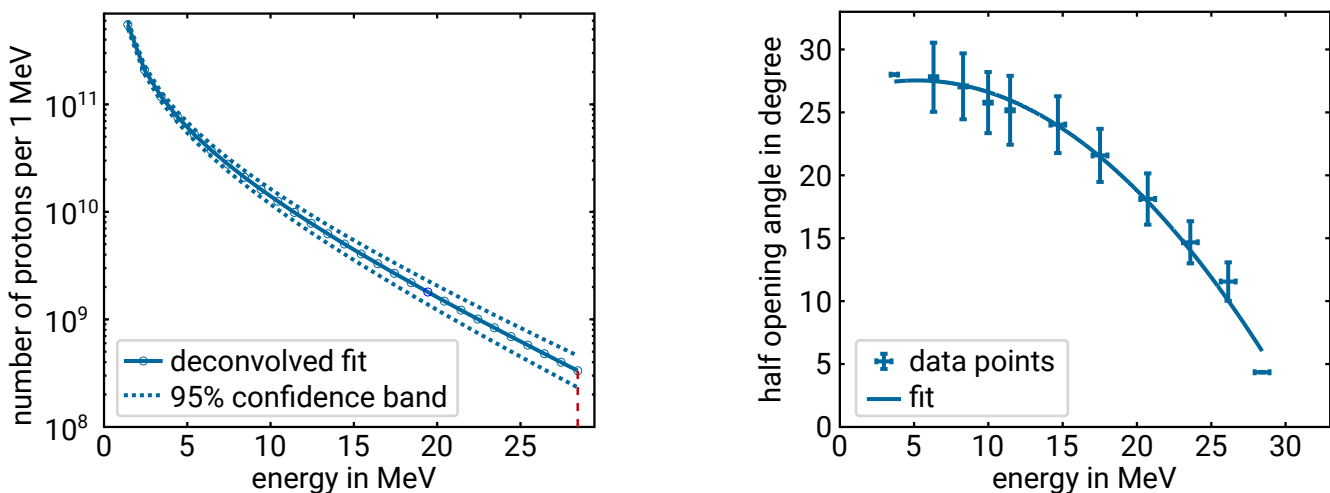

Figure 3.8: Proton spectrum from the TNSA mechanism measured in the Z6 target chamber (left). The energy-dependent divergence of the beam (right). Graphics taken from Simon Busold 2014.

Beam Transport

To capture and transport ions, a high-field solenoid magnet is positioned on a hexapod within the Z6 target chamber. The solenoid's magnetic field causes a focusing effect on the passing charged particles, functioning as an energy selector. However, this focusing effect also causes chromatic aberrations, as the focal length depends on the square of the particle's momentum (Kumar 2009). Imperfect magnetic

fields inside the solenoid introduce spherical aberrations, which along with chromatic aberrations, cause emittance growth of the beam. Additional information regarding the functionality and properties of solenoids can be found in Y.-J. Chen 2003 and Kumar 2009. The pulsed high-field solenoid magnets utilized in the LIGHT beamline were designed and constructed by the high-field laboratory (HLD) at HZDR (Kroll 2019). Figure 3.9 (left) depicts a technical drawing of the solenoid. The capture efficiency depends on the energy of the ions due to the smaller initial directional deviation of higher-energy ions (see Figure 3.8 (right)). Simulations (Metternich 2023) show that the transport efficiency in the corresponding energy interval ($\Delta E/E = 10\,\%$) for protons generated with the TNSA mechanism in the Z6 target chamber and the current LIGHT beamline setup increases from $8.43\,\%$ ($E = 4.75\,\text{MeV}$) to $13.40\,\%$ ($E = 17.5\,\text{MeV}$). The solenoid can capture a maximum opening angle of $130\,\text{mrad}$ ($7.5°$). The magnetic field imperfections, particularly those created by the connection cables of the solenoid, generate filaments in the beam that cause deviations in the energy distribution from that of the entire beam (Metternich 2023; Metternich et al. 2022).
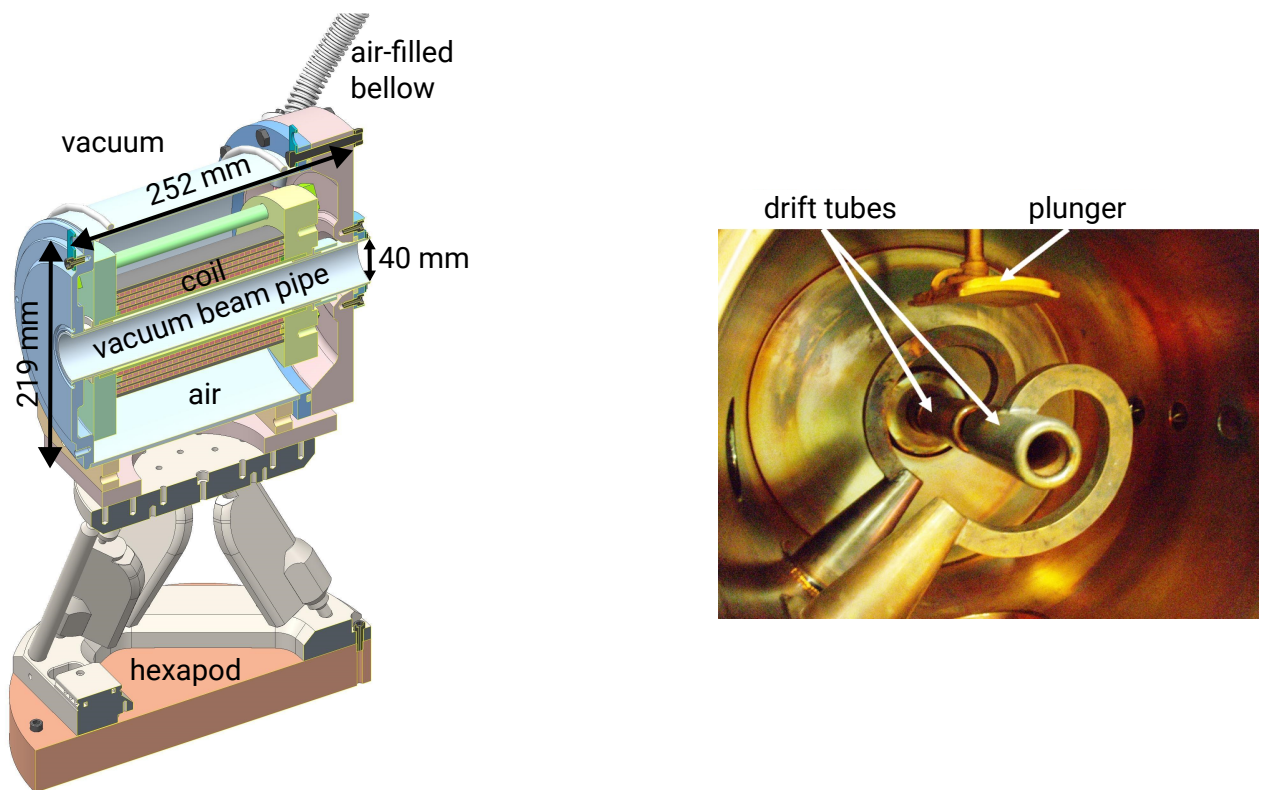

Figure 3.9: Cutaway view of the pulsed, high-field solenoid magnet with a stainless steel housing, which is mounted on a hexapod (Kroll 2019) (left). Photograph of the interior of the RF cavity, which is equipped with drift tubes and a plunger (Simon Busold 2014) (right).

To enhance capture efficiency, it is essential to place the first solenoid close to the TNSA target. The solenoid casing begins $40\,\text{mm}$ behind the TNSA target to allow for the positioning of a motorized stage with a lens and a mirror between the TNSA target and the solenoid before each shot. This is done to adjust the PHELIX laser focus. The magnetic field strength of the solenoid is adjusted to select and transport ions with the desired energy through the beamline.

Another solenoid is used to transversely focus the ion bunch onto the plasma generated in the Z4 target chamber to probe the plasma with as many ions as possible. The optimal placement of the second solenoid

depends on the size of the plasma target to be probed by the ion beam. In order to achieve the desired plasma parameters, the focal spot size of the heating laser (nhelix) is limited to a diameter of 1 mm due to its limited energy. If the focal spot size is increased, the intensity of the laser beam decreases, assuming the energy remains constant, which in turn reduces the plasma temperature. Based on previous experiments (W. Cayzac et al. 2017; A. Frank et al. 2013) and simulations (refer to Chapter 4), this process produces a plasma that is transversely homogeneous in the innermost region, with a diameter of 0.5 mm. Therefore, the second solenoid should focus the ion beam on the plasma to maximize the number of ions passing through this region. As the focal length of the solenoid increases, so does the size of the focal spot (Y.-J. Chen 2003). Therefore, it is important to keep the distance between the second solenoid and the plasma target as short as possible. However, due to the path of the heating laser, the minimum distance achievable is approximately 90 cm (refer to Figure 3.6).

Longitudinal Manipulation

The beamline's component for longitudinal manipulation of the ion bunch is the radio-frequency (RF) cavity, which is a three-gap spiral resonator. It was previously used at the UNILAC of GSI (Häuser 1989) and has a resonance frequency of 108.4 MHz. In Figure 3.9 (right) a photograph of the interior of the RF cavity is depicted. The drift tubes, which are held in place by spiral arms, are visible, as is the plunger utilized to control the resonance frequency of the resonator. RF electric fields generated in cavities are used in accelerators to accelerate or decelerate particles and impact the longitudinal beam dynamics. The particles are subjected to the electric field of the standing wave when traversing the gaps and are shielded from it when passing through the drift tubes. The energy transfer from the cavity to the particles depends on their injection phase. The use of an RF cavity allows for the acceleration of slow ions at the back of the ion bunch and the deceleration of fast ions at the front. The low longitudinal emittance of laser-driven ions makes it possible to significantly reduce their energy spread. For instance, for protons with an energy of 8 MeV, the energy spread was reduced from around 20 % after the first solenoid to below 3 % (S. Busold et al. 2014a; Simon Busold et al. 2015). It is possible to compress the ion bunch to sub-nanosecond durations (Simon Busold et al. 2015; Jahn et al. 2019; Metternich et al. 2022) by overshooting the energy compression. This is achieved by injecting the ions into the cavity at a phase where the ions at the front of the bunch are decelerated to a velocity below the mean velocity of the bunch, while the ions at the back are accelerated to a velocity above the mean velocity. As a result, the leading ions are slower than the trailing ions, allowing the trailing ions to catch up after a certain propagation distance. This methodology will be applied in the stopping power experiment, where sub-nanosecond ion bunches will be generated with an energy spread of 2 %, as determined by simulations (Metternich 2023).

The RF cavity will be configured to compress the ions temporally in the center of the second target chamber, Z4, where the plasma target will be located. The plasma expands rapidly, causing its parameters to change quickly. To minimize the plasma parameter variations during the passing of the ion bunch, a shorter ion bunch is required. This decreases the temporal uncertainty of the plasma parameters that the ions interact with. The transit time factor of the RF cavity, which characterizes the energy gain of a particle passing through the acceleration gaps, taking into account the time variation of the field during particle transit through the gaps, is nearly zero at an energy-to-mass ratio of 0.5 MeV/u (Ding 2018). As a result, it is impossible to temporally compress ion beams with an energy-to-mass ratio of 0.5 MeV/u. For the stopping power experiment, an energy-to-mass ratio of 0.6 MeV/u was targeted. This enables the temporal compression of the ion bunch while remaining close to the stopping maximum ($v_\mathrm{p} \approx v_\mathrm{th}$). The number of particles that can be compressed into a single bunch is determined by the proximity of the RF cavity to the TNSA target. For projectile ions with 0.6 MeV/u, the minimum distance is restricted by geometrical

constraints, resulting in a distance of 1210 mm between the TNSA target and the middle of the RF cavity. The necessary cavity voltage for temporal compression also varies based on the distance between the RF cavity and the plasma target. However, this distance does not significantly affect the resulting beam parameters. Therefore, it is set to 2 m to ensure stable operation of the RF cavity.

3.2.2 Plasma Target

In the planned stopping power experiment with the LIGHT beamline at the experimental area Z6 of GSI the plasma is generated using the nhelix laser. To achieve plasma parameters similar to the experiment by W. Cayzac et al. 2017, the nhelix beam is split into two beams, each with an energy of 30 J, a pulse length of 7 ns (FWHM), a wavelength of 526.5 nm, and a focal spot size of 1 mm. The focal spots are smoothed using a random phase plate (RPP). This section explains plasma generation using a laser, describes the upgraded nhelix laser system, discusses the chosen laser parameters, and presents the interferometric diagnostics developed to measure the plasma's free electron density.

Laser-Plasma Interaction

This section, like the theoretical part of this work, expresses all physical quantities in the cgs unit system (centimeter, gram, second), while numerical values are given in SI base units. For a detailed overview of this topic refer to Mulser et al. 2010.
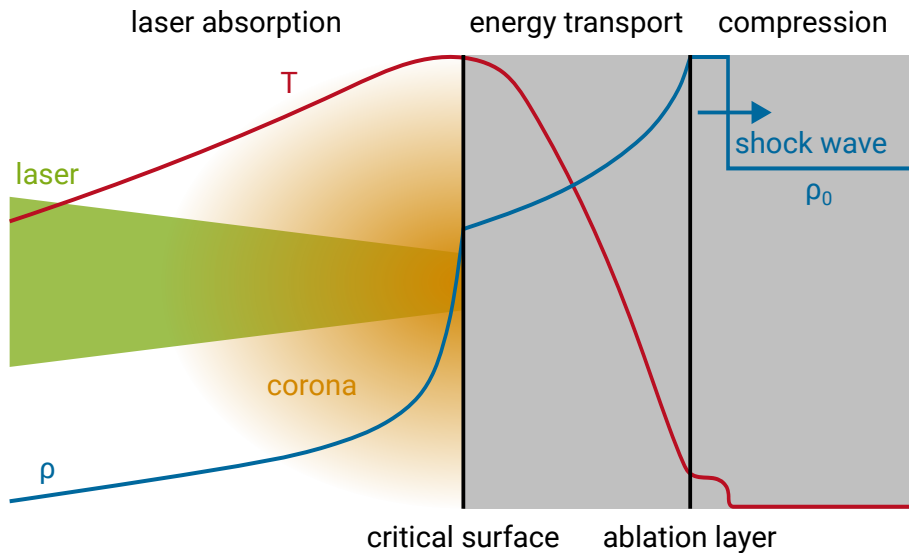

Figure 3.10: Schematic representation of the laser-plasma interaction: In the corona, the laser is absorbed up to the critical density. The reemission or transport zone is heated by heat conduction and X-rays from the corona. The thermalized radiation is also reemitted here. In the compression zone, the solid is compressed by the shock wave driven by the ablation pressure. T and ρ represent the temperature and density, respectively.

Plasma can be generated using intense laser radiation. Figure 3.10 shows a schematic representation of plasma formation and expansion. The intensities present at the target in this work range from 10^{11} W/cm^2 to 10^{12} W/cm^2. A laser pulse with a minimum intensity of approximately 10^9 W/cm^2 can ignite plasma when it strikes matter (BAUER 2003; Mulser et al. 2010). However, the photon energy is typically insufficient to directly ionize the material. The target contains either a free electron or an atom with a weakly bound electron. This electron may be the result of statistical processes or material impurities. Subsequently, the electron begins to oscillate in the electric field of the laser and ionizes other atoms in the target through inelastic collisions. The laser field induces oscillations in the released secondary electrons, which in turn ionize additional atoms. This initiates an avalanche effect, breaking almost all atomic bonds

on the target surface and resulting in the formation of a plasma layer known as the corona. The corona is heated until the end of the laser pulse, and it rapidly expands. The speed of sound of the plasma, which describes the speed of longitudinal waves, can be used to estimate the expansion speed of the corona:

$$c_{\rm s} = \sqrt{\frac{Z_{\rm T} k_{\rm B} T_{\rm e}}{m_{\rm i}}} \tag{3.1}$$

with $Z_{\rm T}$ the plasma ionization degree, $T_{\rm e}$ the plasma temperature and $m_{\rm i}$ the ion mass. For the 180 eV fully ionized carbon plasma studied in this work, a sound velocity of 90 μm/ns is estimated.

Once the incoming laser radiation reaches an electron density at which the plasma frequency $\omega_{\rm p}$ (see Equation 2.2) equals the frequency of the laser light $\omega_{\rm L}$, the laser light cannot propagate any further and is reflected. The refractive index of the plasma can explain this phenomenon:

$$n = \left(1 - \frac{\omega_{\rm p}^2}{\omega_{\rm L}^2}\right)^{\frac{1}{2}}. \tag{3.2}$$

If the plasma frequency $\omega_{\rm p}$ is greater than the laser frequency $\omega_{\rm L}$ the refractive index n becomes imaginary, and the laser is reflected. This results in a corresponding density known as the **critical density** $n_{\rm c}$:

$$n_{\rm c} = \frac{m_{\rm e}}{4\pi e^2} \omega_{\rm L}^2. \tag{3.3}$$

In physical terms, upon reaching the critical density, the plasma frequency of electron oscillations matches the incoming laser light frequency, resulting in a resonance phenomenon. This resonance enables strong interactions between the light wave and the electrons, with the electrons absorbing energy from the laser and subsequently reradiating it, effectively reflecting the light. A higher laser frequency $\omega_{\rm L}$, which corresponds to a lower laser wavelength $\lambda_{\rm L}$, enables the laser to penetrate deeper into the plasma. In this case, the frequency-doubled nhelix laser with a wavelength of $\lambda_{\rm L} = 526.5$ nm reaches a critical density of $n_{\rm c} = 4 \times 10^{21}$ cm^{-3}, which marks the end of the corona. The electron density increases exponentially until it reaches the critical density. In this region, laser absorption is primarily due to inverse Bremsstrahlung. This occurs when an electron absorbs the energy of a photon while being scattered on a plasma ion. Other absorption processes include resonant absorption, where plasmons (Langmuir waves) are resonantly excited by the laser and the coupling of the laser light with various plasma waves which are caused by parametric instabilities.

Behind the critical surface, the corona ends and the energy transport region begins. The energy deposited by the laser is then effectively transported to higher-density regions through diffusion processes. Thermal conduction and radiation are the primary mechanisms for transmitting energy from the corona to deeper plasma layers within this energy transport zone. As a result, the temperature decreases in comparison to the corona, while the density increases to approach solid-state density.

The ablation front is the outer boundary between the energy transport region and the compression region. It signifies the surface from which plasma initiates outward expansion. Within the ablation front, the compression zone shows high density and low temperature. This zone experiences compression due to a shock wave generated by the ablation pressure from the outgoing corona, resulting in progressively higher densities at the target center. This process causes the compressed material to exceed solid-state density, while the temperature remains low. The pressure wave generated propagates through the solid material, and its speed can exceed the speed of sound in the undisturbed part of the material, forming a shock wave. However, the compression zone is significantly limited in space and time when the target is thin.

nhelix Laser System

The target will be heated from both sides with 30 J each, similar to the experiment by W. Cayzac et al. 2017, who used the PHELIX and nhelix lasers for this purpose. In this planned stopping power experiment, the PHELIX laser is being used to accelerate ions via TNSA for the LIGHT beamline. Therefore, the nhelix laser needs to cover both laser beams that irradiate the target. To achieve this, the nhelix laser needs to deliver an energy of 60 J (2×30 J) at a frequency-doubled wavelength of 526.5 nm. Prior to this work, it was not possible to achieve 60 J energy with the nhelix laser system due to defects in the last amplifier rod, which had a diameter of 64 mm and was made of silicate glass. Phosphate glass amplifiers have become more common in new laser systems, resulting in a decrease in the use of this type of glass, particularly in this size. Therefore, a change to phosphate glass was necessary, resulting in a shift in wavelength from 1064 nm to 1053 nm. As part of this thesis, the nhelix laser was redesigned and rebuilt to meet the necessary energy requirements for this work. This section introduces the new nhelix laser system.

Figure 3.11 shows an overview of the new nhelix laser system. The frontend, a seeded (S) Q-switched high-energy (Q2HE) laser by Quantum Light Instruments (QLI), is situated on the first table (FE). It operates at a repetition rate of 10 Hz and a wavelength of 1053 nm, reaching 50 mJ. The frontend is followed by a Pockels cell (PC1), which sets the pulse length to 10 ns and protects the frontend from back reflections. The first table features a serrated aperture (SA) that produces a top hat spatial beam profile after passing through the initial spatial filter and telescope (T1). This telescope decreases the beam diameter from 7.5 mm to 6.5 mm and includes a pinhole in its focal point to function as a spatial filter. All telescopes, except for the final one (T6), function as spatial filters. On the second table, the preamplifier (PreAmp PA) is located. It is nearly identical to the preamplifier of the PHELIX laser. After the second telescope (T2), the beam diameter is increased to 14 mm. The beam is then amplified in a flashlamp-pumped Nd:glass amplifier rod with a diameter of 19 mm (19DP). This amplifier is passed twice, resulting in an energy gain of 200. Following this, a second Pockels cell is used to reduce amplified spontaneous emission (ASE) and protect earlier components from back reflections. Then, the third telescope (T3) increases the beam diameter to 37 mm. The second amplifier stage is a 45 mm Nd:glass rod that is also operated in the double-pass configuration, achieving a gain of 30. Before leaving the PreAmp table, the beam size is increased in the fourth telescope (T4). The main amplifier (MainAmp MA) of the nhelix laser consists of a modified flash lamp-cooled PHELIX MainAmp module. The module has two Nd:glass slabs that are placed at the Brewster angle to reduce surface reflection. The nhelix beam passes through the amplifier six times and increases in diameter with the last two telescopes (T5, T6) after every two passes, resulting in a gain of seven. The final beam diameter is 90 mm. There are three diagnostic beam paths throughout the nhelix laser system: one after the serrated aperture (D1), one after the PreAmp (D2), and one after the MainAmp (D3). Cameras can be used to observe the near and far fields, while Shack Hartmann sensors can measure the wavefront. It has been demonstrated that the nhelix laser can deliver at least 60 J after frequency-doubling, which is sufficient for the planned stopping power experiment. However, a complete and comprehensive characterization of the nhelix laser system has not yet been performed due to time constraints.
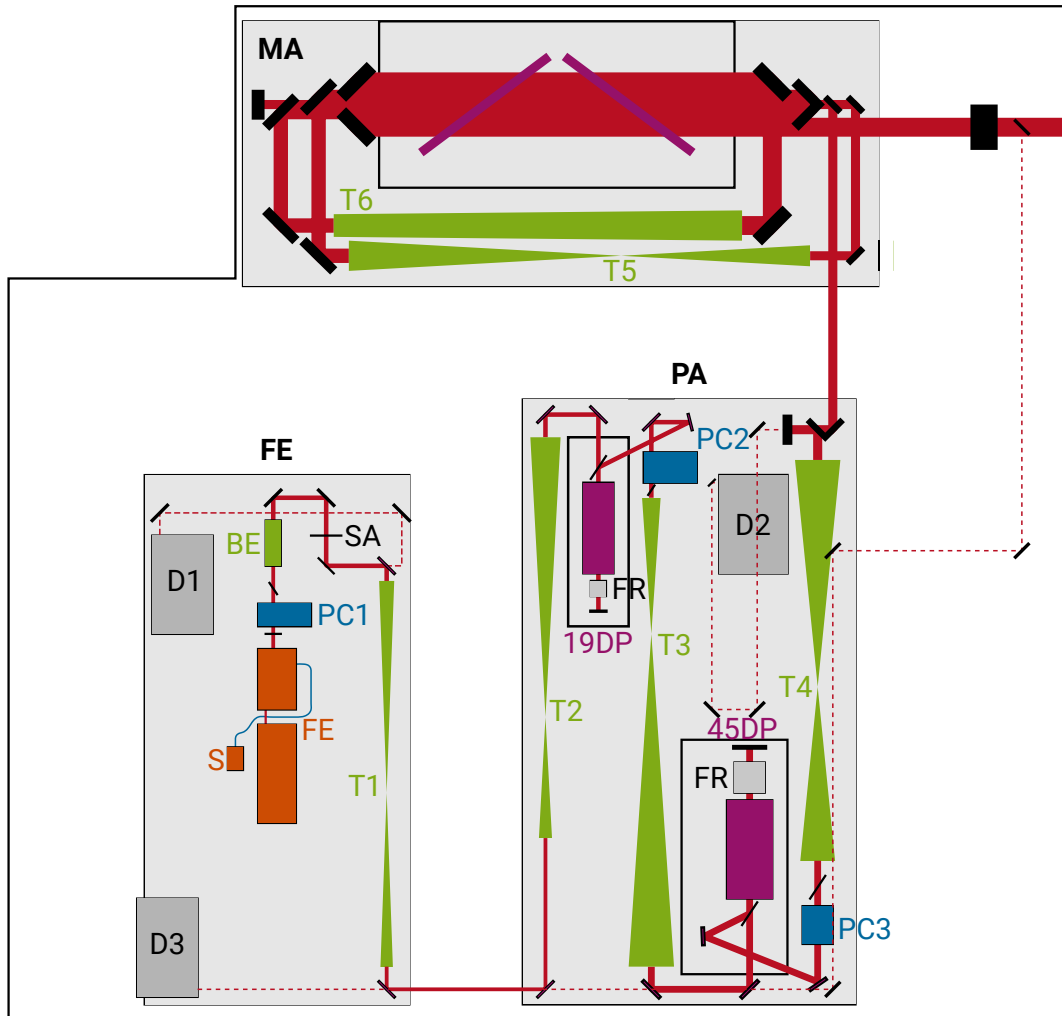
Figure 3.11: Schematic overview of the new nhelix laser system. FE and S represent the frontend and its seed laser, respectively. PC1-3 are Pockels cells. SA denotes a serrated aperture. T1-6 are telescopes. PA stands for the preamplifier. 19DP and 45DP are amplifier stages with diameters of 19 mm and 45 mm, respectively, operated in a double pass configuration. FR are Faraday rotators. MA represents the main amplifier, while D1-3 are diagnostic boxes.
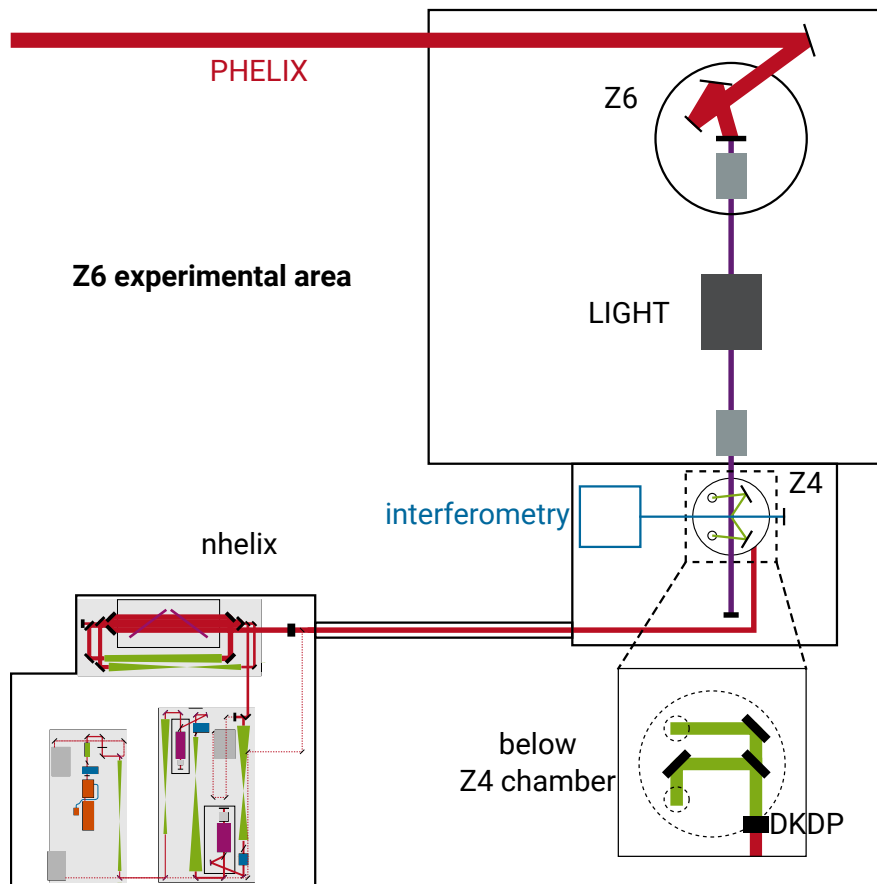
Figure 3.12: Overview of the Z6 experimental area with all relevant components for the stopping power experiment including the nhelix laser in the nhelix room, the LIGHT beamline, and the Z4 target chamber.

To ignite a plasma in the Z4 target chamber, the nhelix laser beam must be guided from the laser room into the Z4 chamber. Figure 3.12 shows the Z6 experimental area. The nhelix beam exits the nhelix room through a tube located approximately 20 cm above the floor. The tube leads to a small, temporary lightproof room. The nhelix beam is then directed beneath the Z4 target chamber, where a DKDP (Deuterated Potassium Dihydrogen Phosphate) crystal is located for frequency-doubling. The critical density is four times higher with the frequency-doubled laser beams, increasing collisional absorption and radiative transport. Radiative transport is a faster mechanism than thermal conduction, resulting in quicker longitudinal heating and homogenization of the plasma. This leads to a more reproducible and more homogenous plasma evolution (Alexander Frank 2012). After the nhelix beam is frequency-doubled, a beamsplitter divides the beam into two equal energy beams. The beams then enter the Z4 target chamber through two windows at the bottom. Inside the target chamber, the beams are focused onto the target using lenses. The laser focus profile can be smoothed to a top-hat profile with a diameter of 1 mm by using random phase plates. This improves the transversal homogeneity of the plasma in relation to the incoming ion beam. The plasma size and temperature in stopping power experiments are mainly restricted by the laser used to generate it. It is important to note that a smaller laser focus can increase the plasma temperature. However, this reduces the range in which the plasma parameters are spatially homogeneous and the timescale on which the plasma parameters are changing.

The plasma's free electron density will be measured via interferometry to verify the hydrodynamic simulations of the laser-generated plasma presented in Chapter 4. These simulations are used to calculate the ions' stopping power along their path inside the plasma, according to different theoretical models. This is necessary to compare measurements with theory.

Interferometric Measurement of the Free Electron Density

To gain a comprehensive understanding of the factors that influence the interaction between plasma and passing particles, it is essential to possess extensive knowledge about the parameters of the plasma. Theoretical simulations can provide insights into these parameters, but they must be validated through empirical evidence.

To characterize the plasma generated by the laser, an interferometric measurement of the free electron density will be performed. As part of this project, Sarah Grimm's master's thesis, entitled "Interferometric Measurement of the Free Electron Density in a Laser-Generated Plasma for Verification of Hydro-Simulations," was overseen by myself (Grimm 2023). In the following section, the setup of the interferometer and the resulting characteristics are briefly described. For more information, refer to the thesis itself.

A suitable interferometer was designed to measure the free electron density in laser-generated plasma. The CAD model of the entire setup is shown in Figure 3.13. A laser frontend (MPL1100-TH) with a wavelength of 355 nm and a pulse duration of 500 ps was ordered from QS Lasers and placed on the lower level of the setup. The wavelength was chosen to probe a significant amount of unchanged plasma since its high critical density ($n_\text{c} = 8.8 \times 10^{21}\,\text{cm}^{-3}$). The optical system comprises a Kepler and Galilean telescope that relays the laser beam image to the plasma and magnifies it by a factor of 24. Subsequently, a Kepler telescope with doublets images the plasma onto the camera, reduces the beam diameter by a factor of 2/3, and simultaneously collimates the beam. The optical system was designed using ZEMAX. Its imaging is limited by diffraction, with wavefront distortions smaller than $\lambda/20$ according to ZEMAX. Thus, the interferometer can produce a significant interferogram by superimposing a portion of the laser beam that passes through the plasma with a portion that does not. The resulting image is captured by a camera with a 16-bit dynamic range and low median readout noise. When the beam passes through the chamber undisturbed, it produces a regular interference pattern of straight stripes. However, if part of the beam encounters free electron density, it results in a change in the refractive index within that area. When the beam goes through the plasma, it accumulates a phase shift in comparison to undisturbed surrounding regions along its path. This causes a change in the stripe distance, which can be used to determine the phase shift. In order to determine the three-dimensional refractive index of the two-dimensional projected phase shift recorded by the camera, it is necessary to assume cylindrical symmetry. This refractive index can then be used to calculate the free electron density. Figure 3.14 shows a schematic overview of the interferometer with the chosen Mach-Zehnder configuration.

Figure 3.13: Overview of the designed system. The experimental setup consists of two base frames: one supporting the Z4 target chamber and the other holding two breadboards on different levels. The laser frontend is located on the lower level, with its beam directed by two mirrors toward an enlarging telescope. The first lens of the telescope is positioned on the breadboard, and the second lens is placed on a rail attached to the base frame of the target chamber. A mirror behind the second lens directs the horizontal beam to a magnifying telescope, which utilizes a vertical structural rail for its lenses. The beam is finally directed into the Z4 target chamber by a tilting mirror. Within the chamber, the beam fully surrounds the plasma at its center. The beam passes through the first doublet of a telescope, with the second doublet positioned on the upper breadboard. This telescope reduces the beam diameter and images the plasma on the camera. The camera is situated behind a Mach-Zehnder interferometer on the upper level of the optical table. The displayed laser beam diameter corresponds to its actual size. The graphic is taken from Grimm 2023.
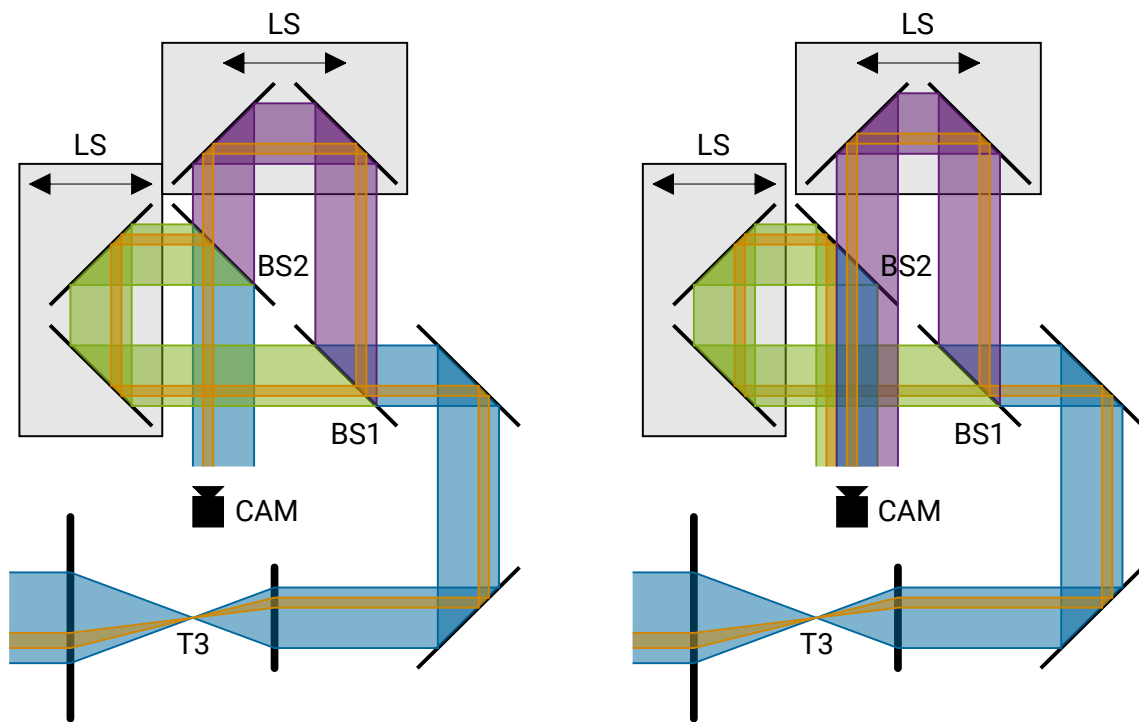
Figure 3.14: Schematic layout of the designed Mach-Zehnder interferometer. The blue laser beam passes through the plasma (orange) and is then reduced in diameter by a telescope (T3). Next, the light is reflected onto a beam splitter (BS1), which splits it into two beams: one reflected (shown in purple) and one transmitted (shown in green). The resulting partial beams are redirected by two mirrors on a linear stage (LS) to the second beam splitter (BS2). The area of overlap between the two partial beams is determined by the position of the linear stage. The beams can be either perfectly overlapped (left) or slightly displaced (right). The latter alignment is used to detect a meaningful interference pattern of the plasma using a camera (CAM). The graphic is taken from Grimm 2023.

The available nhelix parameters were used to test the measurement of the free electron density of a laser-generated plasma, as the nhelix laser upgrade was not yet complete. A graphite target was exposed to laser energy of (1.90 ± 0.13) J at a wavelength of 1053 nm, with a pulse duration of (7.0 ± 0.7) ns (FWHM). In some shots, a phase plate was used to increase the nhelix beam's focus from (48.4 ± 4.4) µm (FWHM) to (193.6 ± 11.0) µm (FWHM). The plasma was analyzed by the interferometer at various times, ranging from -5 to 30 ns after the nhelix reached its half-maximum intensity on the target. A total of 71 successful shots were conducted during the designated beamtime.

The system demonstrated dependability and precision in measurements, despite using nhelix parameters different from those intended for the planned experiment on stopping power. The probe beam of interferometry provided complete access to all plasmas generated during the beamtime. The measured peak free electron density was $(7.57 \pm 0.84) \times 10^{20}$ cm^{-3}.

A comprehensive analysis script was developed to evaluate the generated data. The script enables the examination of interferograms derived from measuring dense plasmas, even when they are highly saturated. Figure 3.15 shows an example of an interferogram captured with the interferometry along with the evaluated free electron density.
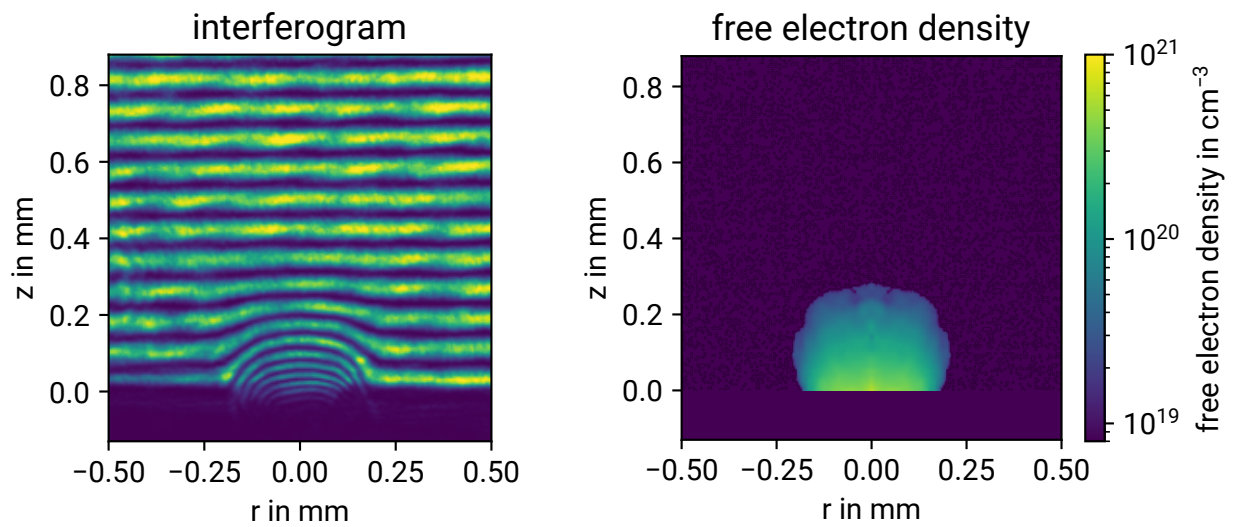
Figure 3.15: Exemplary interferometric measurement (left) and the free electron density obtained from it (right). The focal spot size of the nhelix laser was influenced by the random phase plate and measured to be 193.6 μm (FWHM). This measurement captured the plasma 0.26 ns after the laser reached half of its maximum.

The ions produced by the LIGHT beamline will interact with the plasma generated by the nhelix laser. Chapter 4 will present the theoretical modeling of the stopping power experiment.

4 Theoretical Modeling of the Stopping Power Experiment

In this chapter, I modeled the planned stopping power experiment presented in Chapter 3. The projectile ion beam is taken from simulations of the LIGHT beamline (refer to Section 4.1). The plasma is then simulated using the hydrodynamic code MULTI2D (Ramis et al. 2009) (refer to Section 4.2). Finally, the stopping of the ions in the plasma is modeled using theoretical models for the charge state of the ions, free electron stopping, and bound electron stopping (refer to Section 4.3).

4.1 Beamline Simulations of the Projectile Ions

Simulation studies are performed before conducting beamtimes with the LIGHT beamline to predict the resulting beam characteristics and requisite beamline settings. The simulation employs numerical solutions of the Lorentz equation to calculate ion trajectories in arbitrary electromagnetic fields. The electromagnetic fields used in the simulations for each beamline component are determined by calculations and simulations. The initial TNSA ion beam parameters are determined from various measurements of the TNSA source at the Z6 target chamber (Ding 2018; Metternich 2023). The simulation does not account for self-generated electric and magnetic fields, such as space charge effects. For a detailed explanation of the LIGHT beamline simulations, please refer to Metternich et al. 2022 and Metternich 2023. All beamline simulations presented and used in this thesis were performed in collaboration with Martin Metternich.

The simulations of the LIGHT beamline predict the properties of the projectile ions before passing through the plasma. To reconstruct the respective TNSA beams, Thomson parabola measurements from Ding 2018 were used for carbon ions, and radiochromic imaging spectroscopy (RIS) measurements from Metternich 2023 were used for protons. The results show that C^{4+} ions have the highest number of particles, making them the ideal choice for stopping power experiments. Both the solenoids and the RF cavity were optimized to transport and temporally compress the respective projectiles with an energy-to-mass ratio of 0.6 MeV/u. The setup presented in Section 3.2 was used for the simulation.

Figure 4.1 displays the simulated carbon ion focus at the center of the Z4 target chamber (left). The focal spot size, determined by encircling 50 % of the C^{4+} ions, had a radius of 5.45 mm. The addition of a scattering foil (2 µm Mylar) 300 mm before reaching the focal spot disrupts the transverse filamentation of the beam, as depicted in the middle image of Figure 4.1. The transverse filamentation of the beam is caused by imperfections in the magnetic field of the solenoid due to its connection cables (Metternich et al. 2022). The focal spot size increases to a radius of 6.3 mm due to transverse straggling. On the right, the beam is shown after a 0.5 mm pinhole is added. This is done to limit the area of the ion beam that passes through the plasma and ensure that the plasma parameters are transversely homogeneous. The pinhole allows approximately 0.15 % of the ions in the beam to pass through.
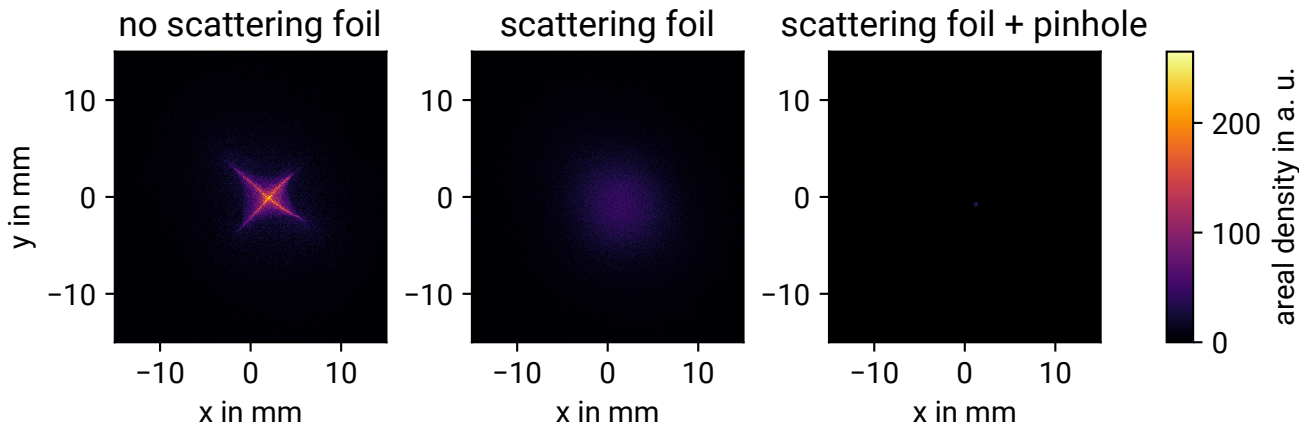
Figure 4.1: Simulated spatial beam profile of the C^{4+} ions in the middle of the Z4 target chamber with no scattering foil (left), with a scattering foil (2 µm Mylar) (middle) and with a scattering foil and a 0.5 mm pinhole (right).
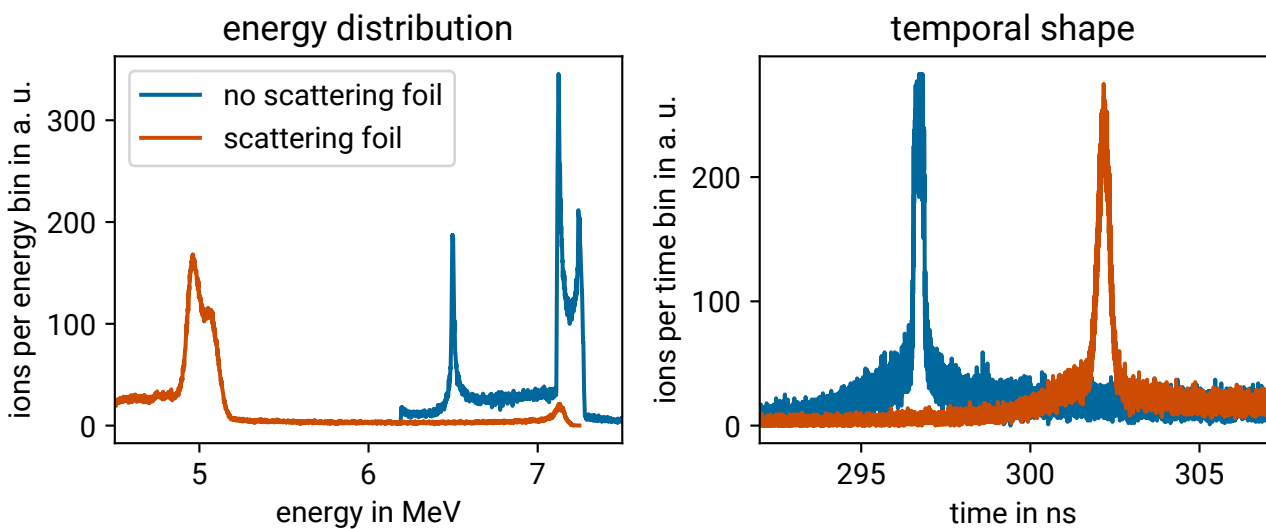

Figure 4.2: Energy distribution (left) and temporal shape (right) of the C^{4+} ions in the middle of the Z4 target chamber with no scattering foil and with a scattering foil (2 µm Mylar).

Figure 4.2 displays the energy distribution (left) and temporal shape (right) of C^{4+} ions at the focal spot, with and without the scattering foil. The energy spectrum exhibits two peaks. The U-shaped peak is the temporally compressed peak of relevance, while the other peak at approximately 6.5 MeV is energetically compressed and not transported optimally. This peak does not affect the stopping power measurements since it is temporally separated from the relevant peak. The relevant C^{4+} ions have a mean energy of 7.2 MeV without the scattering foil. However, with the scattering foil, they lose energy and their mean energy shifts to 6.0 MeV. The energy spread increases with the scattering foil due to straggling, from 2.2 % (width at 20 % of maximum) to 5.2 %. Additionally, the temporal bunch length increases from 336 ps (FWHM) to 432 ps.
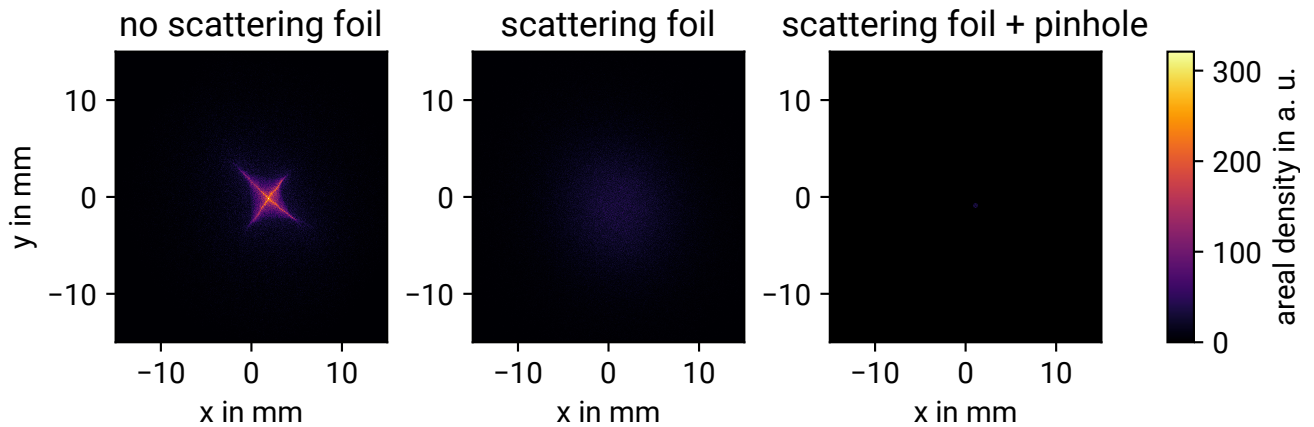
Figure 4.3: Simulated spatial beam profile of the protons in the middle of the Z4 target chamber with no scattering foil (left), with a scattering foil (1 μm Mylar) (middle) and with a scattering foil and a 0.5 mm pinhole.
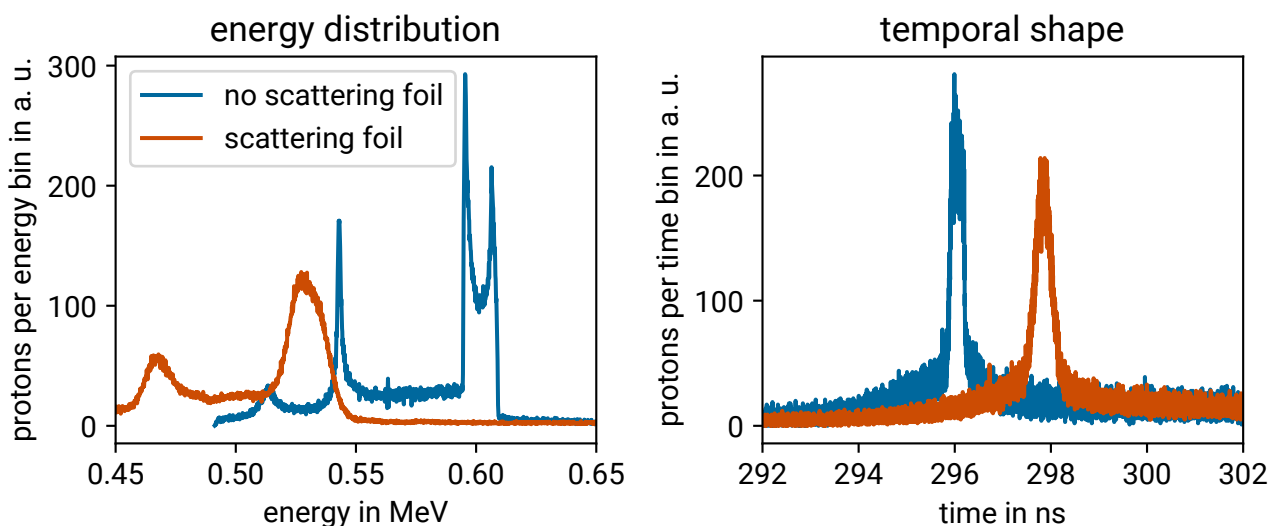

Figure 4.4: Energy distribution (left) and temporal shape (right) of the protons in the middle of the Z4 target chamber with no scattering foil and with a scattering foil (1 μm Mylar).

Similarly, Figures 4.3 and 4.4 show the focal spots, energy distributions, and temporal shape for protons with and without a 1 μm thick Mylar scattering foil. The focal spot size, measured by encircling 50 % of the protons, has a radius of 4.45 mm. Approximately 0.12 % of the protons in the beam can traverse the pinhole. The mean energy of the relevant protons is 0.60 MeV without the scattering foil and 0.53 MeV with the scattering foil. The energy spread and temporal bunch both increase with the scattering foil. Specifically, the energy spread widens from 2.4 % (width at 20 % of maximum) to 8.0 %, while the temporal bunch increases from 304 ps (FWHM) to 439 ps.

Table 4.1 summarizes the beam parameters with and without the scattering foil. The simulated projectile beams are used to model the planned stopping power experiment (refer to Chapter 3). For that, the simulated beams must pass through a plasma, which is modeled in the next section. Chapter 5 presents preparatory experiments, which included generating the simulated beams as one of the main objectives.

Table 4.1: Parameters of the projectile ion beams with and without the scattering foils according to beamline simulations.

parameter	without scattering foil		with scattering foil	
	C^{4+} ions	protons	C^{4+} ions	protons
mean energy	7.2 MeV	0.60 MeV	5.0 MeV	0.53 MeV
energy spread (width at 20 % of maximum)	2.2 %	2.4 %	5.2 %	8.0 %
temporal bunch width (FWHM)	336 ps	304 ps	432 ps	439 ps
focal spot radius (50 % encircled)	5.45 mm	4.45 mm	6.3 mm	6.6 mm

4.2 Hydrodynamic Simulation of the Plasma Target

The hydrodynamic approach is appropriate for describing plasma evolution over a relatively long timescale of several nanoseconds, as it deals with slow-varying average quantities. However, it is only valid when the particle energy distribution follows a Maxwellian distribution, indicating that the plasma is in a state of local thermal equilibrium (LTE). This implies that collision processes are more dominant than excitation processes caused by plasma radiation. It can be assumed that LTE applies to the relevant regions of the plasma in this work.

The hydrodynamic model proposes that the plasma is neutral and consists of two distinct fluids: electrons and ions. Each fluid can be described by four hydrodynamic variables: mass density ρ, average velocity $\vec{u}$, average temperature T (or energy ϵ), and pressure P. A system of four equations is constructed for each fluid, comprising the conservation of mass, momentum, and energy, as well as the equation of state (EOS) of the target species. The system is solved using the heat transport coefficients and the Maxwell equations. For a more detailed hydrodynamic description, please refer to McKenna et al. 2013 and Mulser et al. 2010.

The hydrodynamic code utilized in this study is MULTI2D (Ramis et al. 2009). It is proficient in handling axial-symmetric geometry problems related to plasma hydrodynamics and various energy transfer mechanisms, such as electronic heat conduction, thermal radiation transport, and energy deposition by laser or ion beam. The MULTI2D model uses unstructured grids composed of triangular elements and employs a fractional step scheme to advance state variables through sub-steps, with only specific physical processes active in each step. The conservation of physical quantities is a primary focus. For further information on MULTI2D, please refer to Ramis et al. 2009.

The nhelix laser will be used to generate the plasma. The plan is to irradiate a planar carbon foil from both sides with an areal density of $104\,\mu g/cm^2$ ($\rho = 1.3\,g/cm^3$). The beams will be frequency-doubled (526.5 nm) with 30 J in each beam and a pulse length of 7 ns (refer to Chapter 3). A. Frank et al. 2013, Tauschwitz et al. 2013 and W. Cayzac et al. 2017 have shown that similar parameters result in the generation of a hot, fully ionized, and sufficiently homogeneous carbon plasma. The MULTI2D simulation used a Gaussian temporal laser profile and a supergaussian spatial profile of order $n = 8$. The simulation began 7 ns prior to the maximum laser intensity ($I \approx 5 \times 10^{11}\,W/cm^2$) and employed a Langrangian grid. Two-dimensional data on the current state of plasma expansion was generated every 0.25 ns.

For further calculations using MULTI2D simulations, it is necessary to conduct post-processing of the simulation data. To calculate the charge state and stopping power of ions passing through a plasma, one needs to know the plasma temperature T_e, density ρ, free electron density n_e, and plasma charge state Z_T. MULTI2D provides the grid of triangular elements used at each time step. The plasma temperature T_e is defined at the nodes of the grid, while the pressure P and mass density ρ are defined for each triangular cell. To determine the plasma charge state, the Saha equation (Saha 1920) can be used, which is valid for LTE:

$$\frac{n_Z + 1}{n_Z} = \frac{1}{4\pi^{\frac{3}{2}}} \frac{Q_{Z+1}(T_e)}{Q_Z(T_e)} \left(\frac{k_B T_e}{I_H}\right)^{\frac{3}{2}} \frac{1}{n_e a_0^3} \exp\left(-\frac{I_Z}{k_B T_e}\right). \tag{4.1}$$

Here, n_Z represents the number density of plasma ions with charge state Z, Q_Z is the statistical partition function of ions with charge state Z, I_H is the ionization energy of hydrogen, I_Z is the ionization energy associated with charge state Z, and a_0 is the Bohr radius. In Zaghloul et al. 2000, a solution for ideal plasmas is presented when the pressure P and the number density of plasma ions n_T are known:

$$Z_{av} = \frac{P}{n_T k_B T_e} - 1. \tag{4.2}$$

Z_{av} represents the average charge state, while the number density of plasma ions, n_T, can be calculated using the mass density, ρ. This calculation is valid for regions where the plasma is ideal and in local thermal equilibrium, which is the case for the relevant regions of the stopping power experiment.

To estimate the influence of non-LTE regions in the plasma, a second method for determining the charge state is also used. A dedicated code called FLYCHK (Chung et al. 2005) is capable of calculating the degree of ionization of plasma ions in non-LTE conditions. The method solves the rate equations of the ionization and recombination processes.
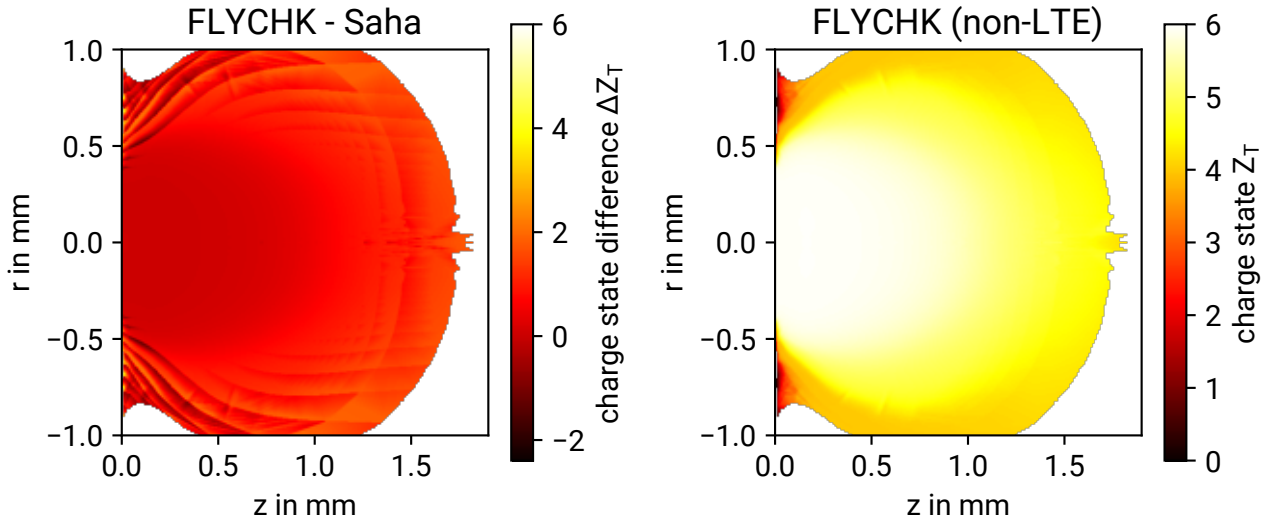

Figure 4.5: Difference of the calculated charge states of the plasma simulated with MULTI2D after 7 ns of plasma expansion (left). The calculated charge state with the non-LTE FLYCHK code is subtracted from the charge state calculated with the Saha equation (LTE). Charge state distribution calculated with the non-LTE FLYCHK code (right).

Figure 4.5 shows the difference between the Saha equation and the FLYCHK code (left) and the charge state distribution calculated with the non-LTE FLYCHK code for the plasma expansion after 7 ns. The

laser and projectile beams travel along the z-axis. The charge state is calculated to range from 4 to 6 in calculations performed with the non-LTE FLYCHK code. The differences between the Saha equation and the FLYCHK code are $|\Delta Z| \leq 1.9$ in the relevant parts of the plasma, where the projectile ions interact with the plasma ($|r| \leq 0.3$ mm). In the denser regions ($|z| \leq 1$ mm), where most of the stopping takes place, the differences of the different calculated charge states are below 0.6. This small difference is not expected to noticeably affect the calculated stopping power. For the remaining calculations in this work, the non-LTE FLYCHK code was chosen over the Saha equation. This decision was made because there is no disadvantage in using the FLYCHK code and it avoids the LTE assumptions made by the Saha equation.

Since it is impossible to measure the energy loss of individual projectile ions, it is necessary to ensure that all ions in the bunch interact with the plasma under similar plasma conditions. Therefore, transverse homogeneity (r-axis) is required. A decrease in transverse homogeneity degrades the resolution of the energy loss measurement. To reduce the required size of the transversally homogenous region, a pinhole will be used to decrease the diameter of the projectile beam. Longitudinal homogeneity (z-axis) is crucial to ensure a nearly constant projectile ion charge state and stopping power along the propagation path through the plasma. Both transverse and longitudinal homogeneity are necessary for the stopping power experiments and are further investigated.

Figure 4.6 illustrates the plasma conditions for three different times with a 16 µm offset of the ion beam axis (z-axis).
The first time (4 ns) corresponds to the early phase of laser heating before reaching the peak laser intensity (7 ns). At this stage, the plasma is partially ionized. The target is not fully heated yet, as the temperature in the middle of the target is less than 20 eV, and the plasma ion charge state is one, which is lower than the target edges that have been heated first ($T_e = 115$ eV and $Z_T = 5.8$).
The second time (7.75 ns) corresponds to the maximum electron temperature ($T_{e,max} = 180$ eV) reached during the plasma expansion in the middle of the target. Here, all plasma parameters show longitudinal homogeneity ($n_e = 2 \times 10^{20}$ cm^{-3} and $Z_T = 5.95$).
The third time (15 ns) corresponds to the later stages of the plasma expansion when the target is no longer fully ionized. The plasma temperature and density are significantly lower ($T_e = 64$ eV and $n_T = 8 \times 10^{18}$ cm^{-3}). The areal density of the target has strongly decreased due to two-dimensional plasma expansion.

Figure 4.7 shows the areal density profile of the plasma transverse to the ion beam axis at different times of the plasma expansion, which is used to estimate its transverse homogeneity. The dashed lines indicate the edges of the projectile ion beam, which will have a diameter of 0.5 mm due to a pinhole. The simulation exhibits some numerical artifacts for early times until 4 ns. The stopping calculations for these times should be viewed with caution as they may not be entirely accurate. Subsequently, the plasma expands two-dimensionally and becomes increasingly homogeneous in the region where the beam passes ($|r| \leq 0.25$ mm), with maximum discrepancies of 17 %. By 10 ns, it is almost perfectly homogeneous with a maximum discrepancy of 5 %, and this remains consistent until the end of the two-dimensional expansion. At the boundaries of the plasma ($|r| = 0.75$ mm), there are numerical errors resulting from the Lagrangian grid and its discontinuous transition to vacuum. These errors become more pronounced with time, as the plasma undergoes two-dimensional expansion.

To ensure accurate simulations, it is necessary to fully characterize the nhelix laser focal spot and pulse length on the target. Afterwards, the plasma parameters acquired from the MULTI2D simulation must be verified by comparing the simulated free electron density with the interferometric measurements during the experiment.
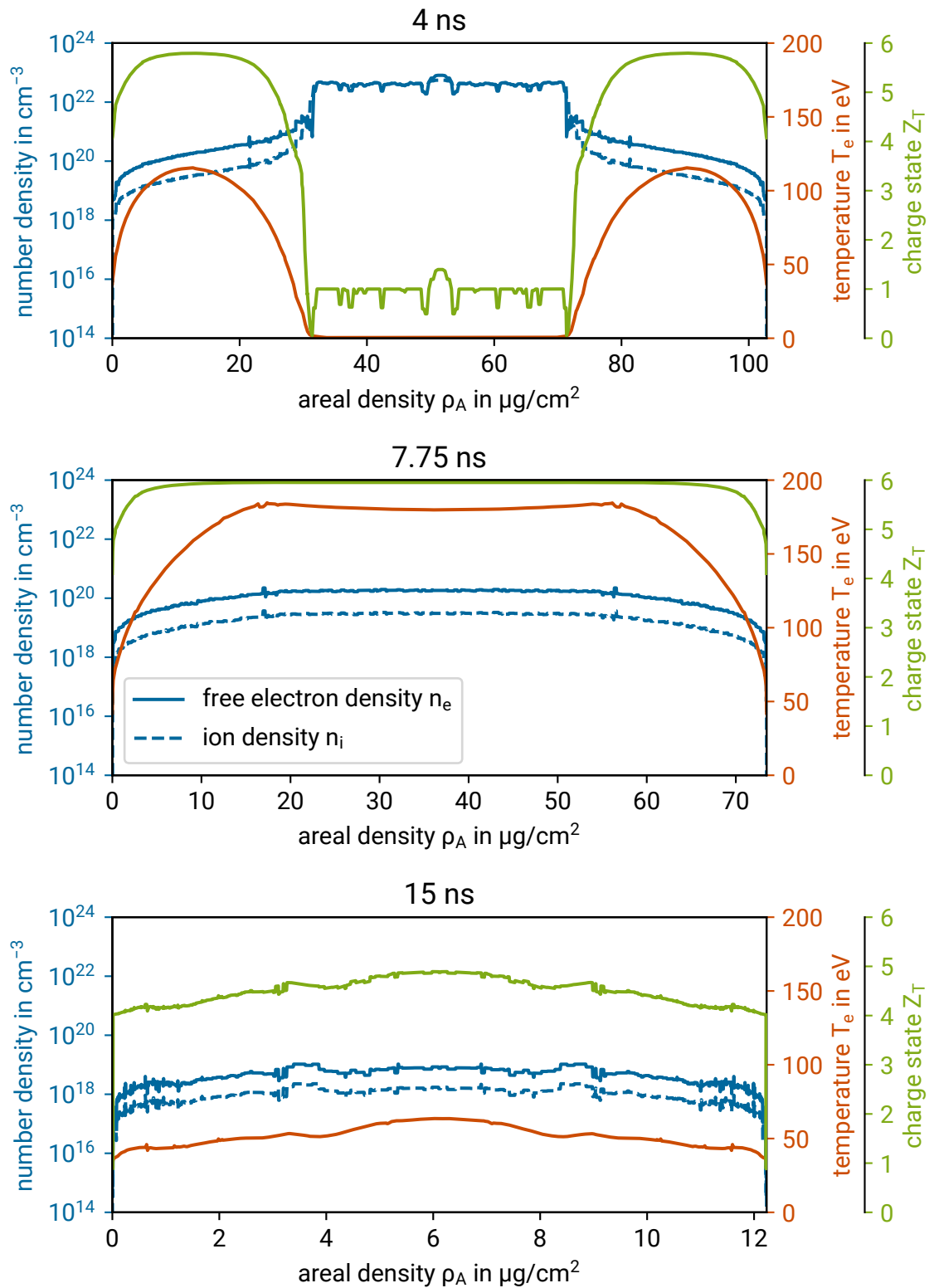
Figure 4.6: Profiles of ion density, free electron density, electron temperature and charge state as a function of the target areal density, on the ion axis and at different times of plasma expansion.
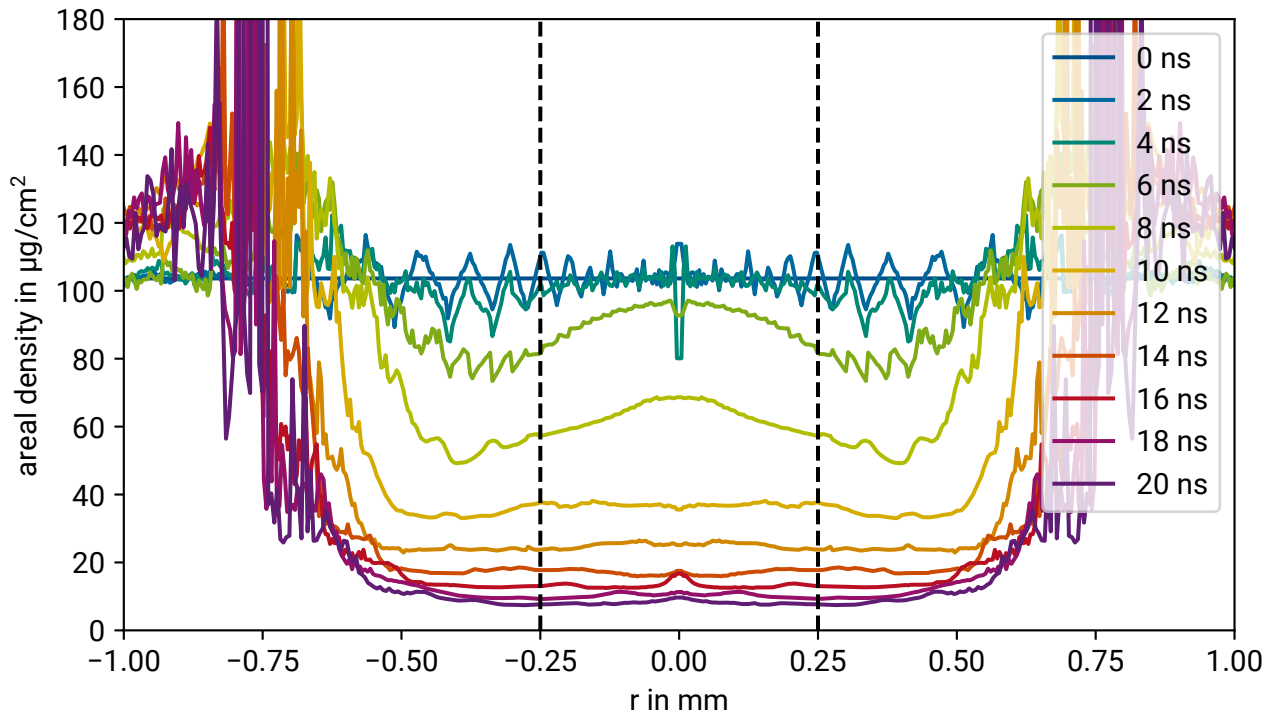
Figure 4.7: Transversal areal density profiles of the plasma shown in 2 ns steps, as obtained from MULTI2D simulations. The dashed lines indicate the edges of the projectile ion beam with a diameter of 0.5 mm.

This work utilizes the presented plasma simulation to calculate the theoretical energy loss based on various models.

4.3 Stopping Power Calculations

This section presents the calculation of the stopping power of projectile ions in plasma using various theoretical models. First, I considered an ideal ion/proton beam with an energy-to-mass ratio of 0.5 MeV/u moving along the central axis ($z = 0$) of the plasma. Subsequently, I conducted a full 2D simulation of the experiment using the realistic beams created with the beamline simulation.

For all simulations in this section, the charge state of the projectile ions was calculated using the Gus'kov model and its nonequilibrium extension (see Section 2.3.3). Equation 2.40 is used to calculate the stopping power of bound electrons.

4.3.1 1D Simulations with Ideal Ion Beam

This subsection considers an ideal ion beam with no spatial or temporal size unless otherwise specified.
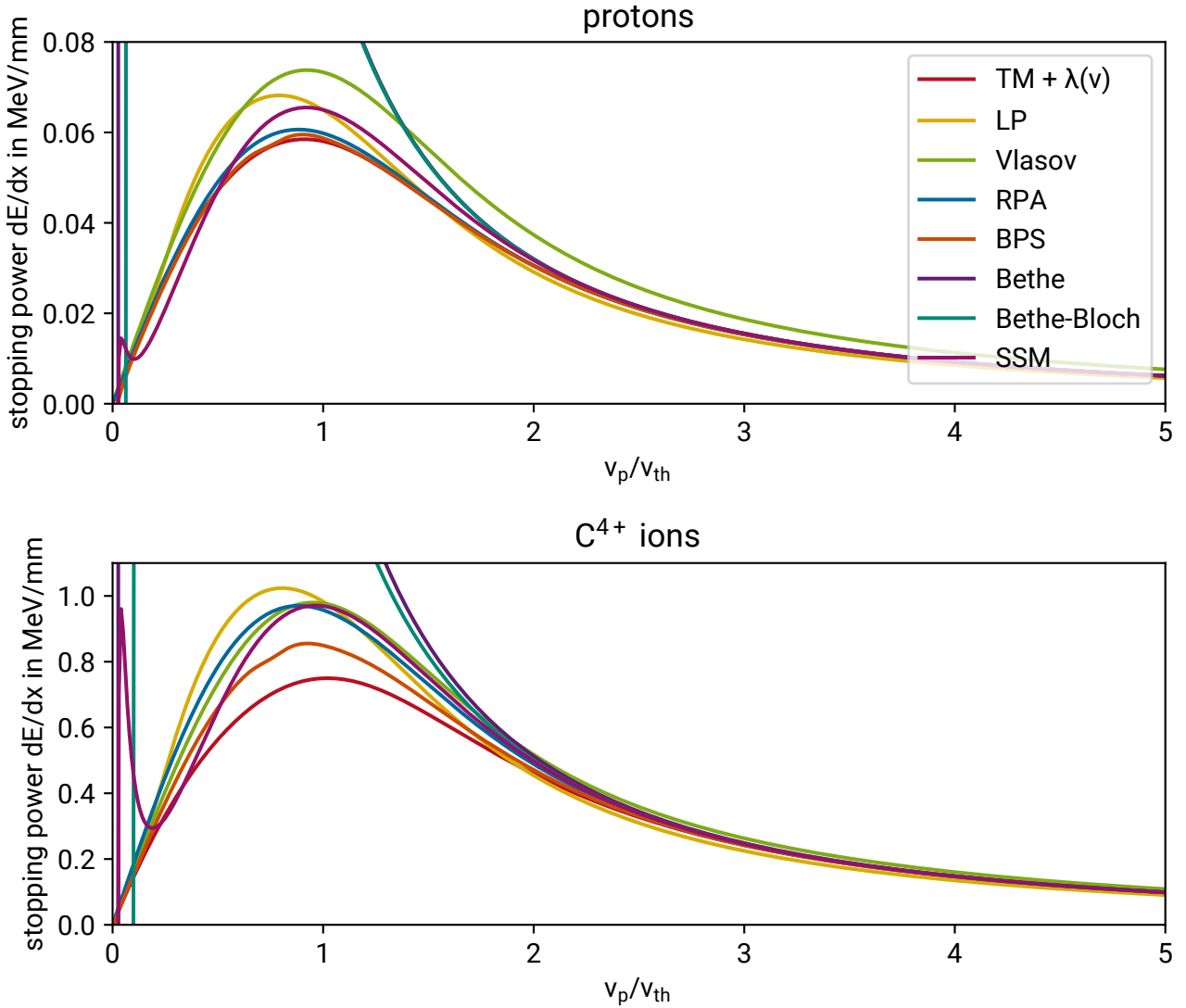

Figure 4.8: Comparison of various stopping power predictions for protons (top) and C^{4+} ions (bottom) interacting with a free electron density of 3×10^{20} cm^{-3} and a temperature of 180 eV as a function of the ratio between the projectile velocity and the thermal plasma electron velocity.

Figure 4.8 shows the stopping power of protons and C^{4+} ions in a plasma with $n_e = 3 \times 10^{20}$ cm^{-3} and $T_e = 180$ eV as a function of the ratio of the projectile velocity to the thermal electron velocity, according to various theoretical models (refer to Chapter 2). The calculation only considers stopping by free electrons. The different theoretical models agree for high projectile velocities. All of the models approach the Bethe formula for $v_p \gg v_{th}$.

However, discrepancies start to arise between the theories for lower projectile velocities ($v_p/v_{th} < 2$). These discrepancies are at their maximum at the stopping maximum ($v_p \approx v_{th}$). Both the Bethe and

Bethe-Bloch formulas demonstrate significantly higher stopping powers than the other theories. As for the carbon ions, the four approaches based on the first Born approximation (Vlasov, RPA, SSM, Li-Petrasso LP) feature similar stopping curves, while for protons, the differences between them are more pronounced. The T-Matrix with $\lambda(v)$ (TM $+\lambda(v)$) theory predicts substantially lower values for carbon ions in the stopping maximum compared to other theories. This theory considers nonperturbative effects and collective effects simultaneously. These results suggest that the significant discrepancies in relation to standard approaches come from nonperturbative effects. The latter appears to have a significant impact in the region of maximum stopping, where the Coulomb coupling between the projectile and the plasma is at its highest. For protons, the T-Matrix with $\lambda(v)$, RPA and BPS show similar values at the stopping maximum, indicating that nonperturbative effects are less significant.

The next stage of the calculations involves the ion beam traversing the plasma, which has been simulated using MULTI2D. The energy loss is determined by integrating the stopping power along the projectile path in the plasma target. As the ions lose a significant amount of energy inside the target, the projectile velocity cannot be considered constant during the interaction. Therefore, the energy of the projectile changes in every step it travels through the plasma. The charge state of carbon ions is adjusted stepwise based on the local plasma and current projectile ion parameters.

Figure 4.9 illustrates the stopping power of the carbon ions passing through the plasma for different times of expansion. The stopping power was calculated using the plasma profiles from Figure 4.6 and different theoretical models (refer to Chapter 2). The calculated average charge state, as predicted by the nonequilibrium Gus'kov model (refer to Section 2.3.3) for the T-matrix with the $\lambda(v)$ case, is also presented. At early times (4 ns), the plasma is longitudinally inhomogeneous and the target is not completely heated, resulting in lower stopping power in the middle where it is dominated by bound electrons. In hotter regions at the edges, the plasma is highly ionized, resulting in a higher stopping power. However, different stopping power theories show significant discrepancies in these regions. The asymmetry arises from the fact that the ions lose energy along their path, which in turn affects their stopping power. The average charge state prior to entering the plasma is 4. Upon entering the plasma, it begins to rise to approximately 5.5, and then it gradually and almost linearly declines to 5.4. The cold region in the middle of the target does not significantly impact the charge state due to its low thickness. This implies that the ions are only present in this region for a brief period. The nonequilibrium Gus'kov model is not expected to yield accurate results during the initial stages of expansion.

For intermediate times (7.75 ns), where the plasma is nearly homogeneous, the stopping power theories feature stable values along the ion path. The mean charge state increases to approximately 5.6 and remains relatively stable for the majority of the passing. The charge state then gradually declines to 5.5 before exiting the plasma.

For later times (15 ns), the stopping power decreases significantly due to the decreased plasma temperature. The decreasing areal density is due to the two-dimensional plasma expansion (refer to Section 4.2). The average charge state does not reach a maximum and gradually rises from 4 to 5.2 throughout the plasma.
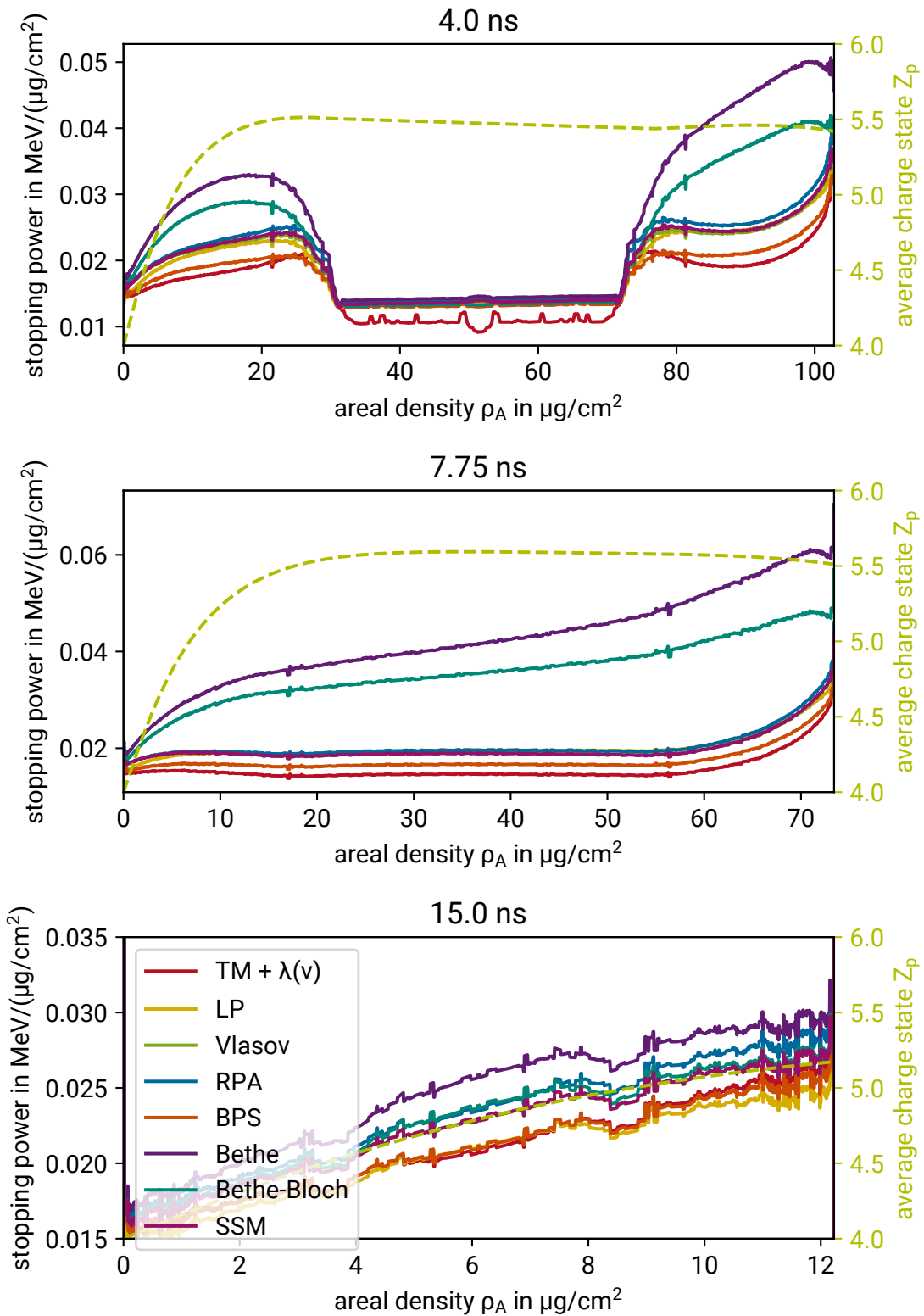
Figure 4.9: Stopping power profiles and charge state of the carbon ions in the plasma target as a function of the areal density for different times.
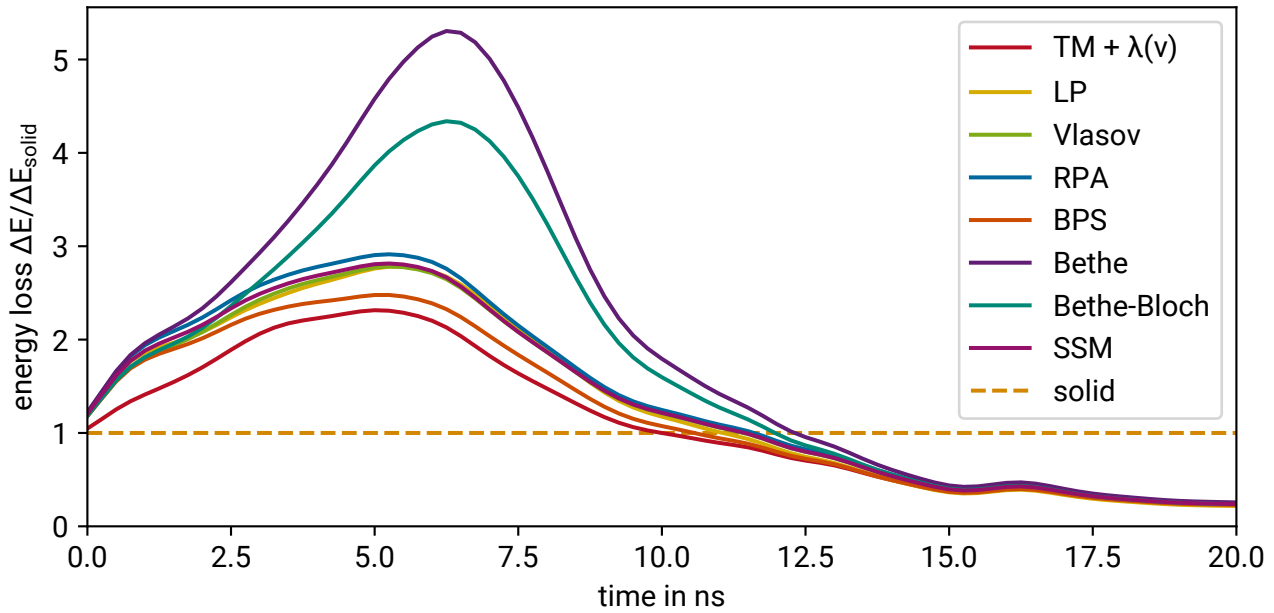
Figure 4.10: Comparison of the energy loss of the carbon ions calculated according to different theoretical models over the plasma expansion time.

Figure 4.10 shows the energy loss of C^{4+} ions as they travel through the plasma at different times of expansion. The energy loss is normalized with the energy loss of carbon ions in a solid target with an areal density of $104\,\mu g/cm^2$. The energy loss of the solid target was calculated using the SRIM code and is $\Delta E_{solid} = 742\,keV$. It is assumed that the plasma conditions are fixed as a single ion travels through it quickly (200–300 ps). When considering an ion bunch with a temporal width of 1 ns, which is achievable with the LIGHT beamline (Metternich et al. 2022), the ions travel through the plasma at different times, causing them to experience varying plasma conditions. To account for the temporal length of the ion bunch, a Gaussian filter with a full width half maximum of 1 ns was applied to the results. This explains why the energy loss curves do not start at unity.

At $t = 0\,ns$, the laser beams irradiate the target, creating plasma. As the target ionizes, the density of free plasma electrons increases, which reduces the recombination processes of the projectile. This enhances the ion stopping power and energy loss due to the simultaneous increase in the stopping Coulomb logarithm and the mean charge state of the ion beam. Energy loss increases across all theories and peaks at approximately 5.5 ns when the plasma becomes fully ionized. Subsequently, the energy loss decreases because of the decrease in plasma areal density caused by the three-dimensional expansion of the plasma in a vacuum. Eventually, it reaches the level of cold matter at 10–12.5 ns.

The Bethe and Bethe-Bloch theories predict a maximal enhancement of approximately 530 % and 430%, respectively. Theories based on the first Born approximation forecast values between 280 % and 290 %. The BPS model predicts a value of 250%, while the T-Matrix ansatz with $\lambda(v)$ suggests a value of 230 %. There are significant energy-loss differences among the various theoretical approaches. These discrepancies occur in the region of maximum energy loss, where the ratio v_p/v_{th} is close to unity, resulting in the highest stopping power. Only measurements around the maximum energy loss can potentially distinguish between the results of the different theories and serve as a benchmark for them. Based on these results, a resolution

of 14 % would allow for distinguishing the results of the T-Matrix with $\lambda(v)$ and the BPS model from the other theories. Based on previous experiments, these two theories are expected to provide the best descriptions of the experiment (W. Cayzac et al. 2017). It is estimated that an energy resolution of at least 11 % is necessary to differentiate between the T-Matrix with $\lambda(v)$ and the BPS model. The Bethe and Bethe-Bloch will most definitely be distinguishable from the other theories. They are not expected to predict realistic results around the stopping maximum.
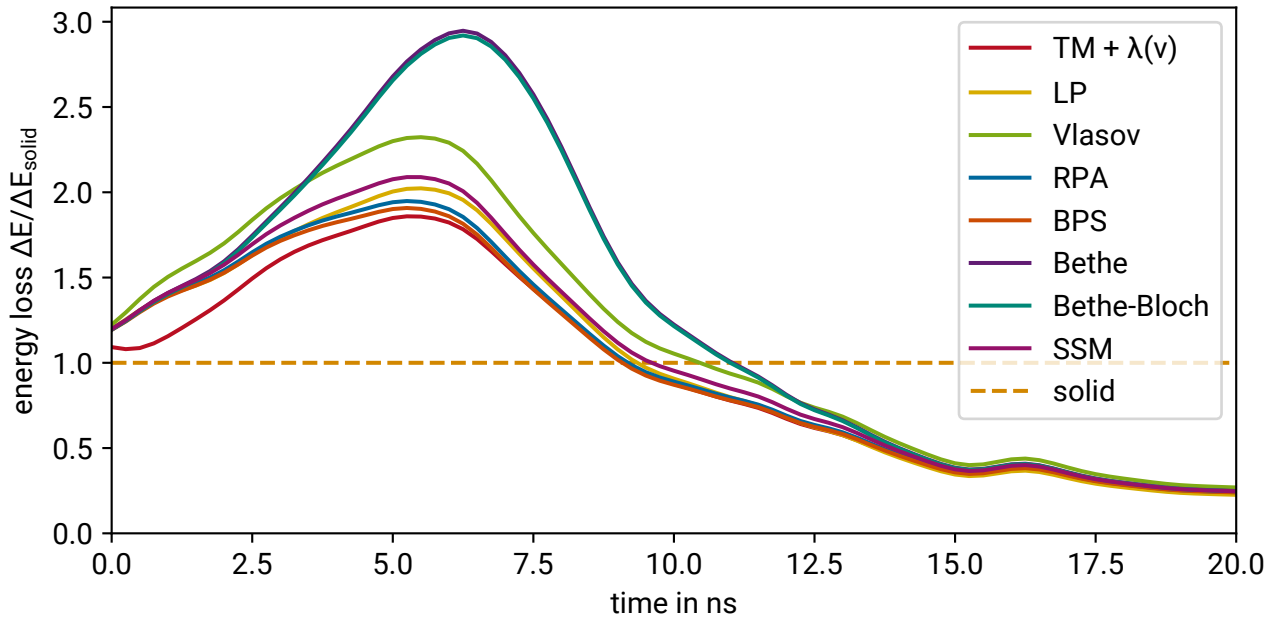

Figure 4.11: Comparison of the energy loss of the protons calculated according to different theoretical models over the plasma expansion time.

To differentiate between theories based on the first Born approximation, it is possible to observe the stopping power of the protons. Figure 4.11 shows the energy loss of protons as they travel through the plasma at different times of plasma expansion. The energy loss is normalized with the energy loss in the solid target ($\Delta E_{\text{solid}} = 37\,\text{keV}$). The temporal length of the proton bunch is also taken into consideration. The charge state estimation is not considered, and the charge state is assumed to be 1 throughout.

All stopping theories predict that protons experience lower energy losses than carbon ions. The Bethe and Bethe-Bloch theories predict a similar maximal energy loss of approximately 290 %. The theories based on the first Born approximation show higher discrepancies in the case of protons. The Vlasov stopping power model predicts a maximum stopping power of 230 %, while the SSM, Li-Petrasso, and RPA models predict values of 210 %, 200 %, and 195 %. The T-Matrix with $\lambda(v)$ and BPS models predict the lowest energy at approximately 185–190 %. These results enable discrimination between theories that were indistinguishable for carbon ions with realistically achievable energy resolutions. To differentiate the Vlasov model from other theories, an energy resolution of 11 % is sufficient.

In order to distinguish between the various presented stopping power models, except for the Li-Petrasso and RPA models, an energy resolution of 8 % is required for the planned stopping power experiments. To differentiate between the Li-Petrasso and RPA models, an energy resolution of 6 % is required. Previous stopping power experiments suggest that the stopping power will be close to or lower than the predictions

made by the T-Matrix with $\lambda(v)$ model (W. Cayzac et al. 2017; Frenje et al. 2019). In this case, an energy resolution of 14 % is adequate to eliminate all stopping power models except for the T-Matrix with $\lambda(v)$ and the BPS model. An energy resolution of 11 % would also eliminate the BPS model. In Section 5.5, the energy resolution of the planned stopping power experiment in a plasma will be estimated based on the experimental results of the stopping power measurements in a solid foil.

4.3.2 Full 2D Simulation

In this subsection, a realistic beam resulting from beamline simulations (see Section 4.1) is propagated through the plasma instead of a perfect ion beam. For this, the path for each projectile ion through the plasma is calculated. The ions move along their paths and experience a stepwise energy loss. These calculations are only done for the carbon ion beam to reduce redundancies.
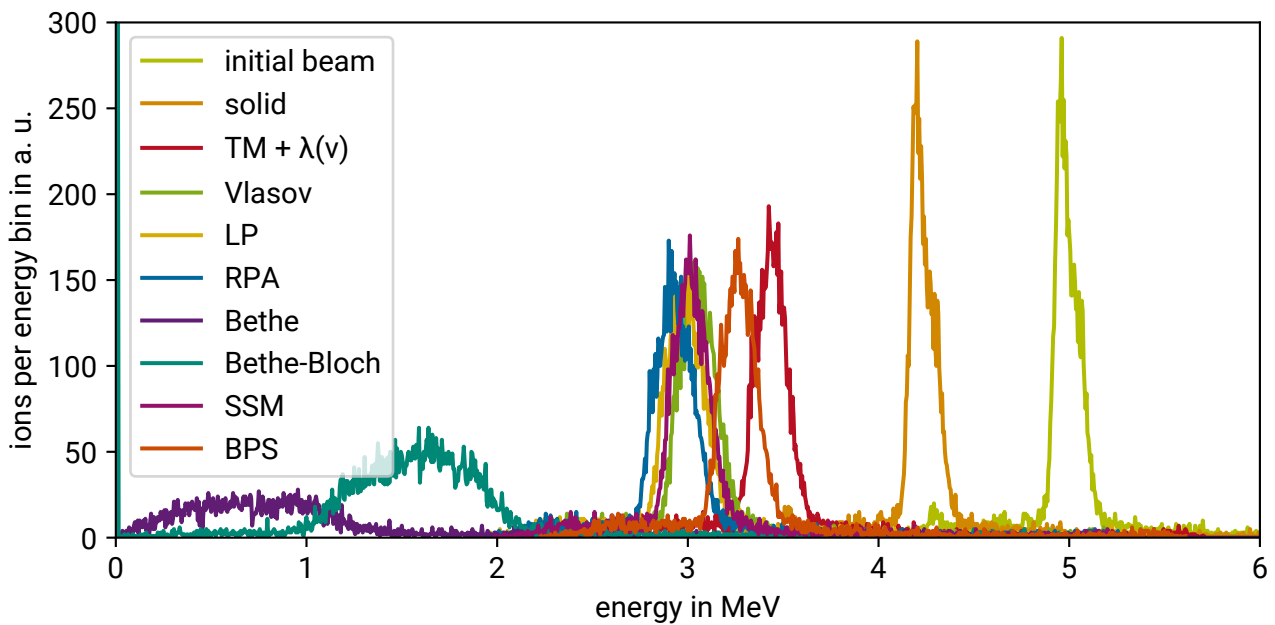

Figure 4.12: Energy spectra of the ion beam before the target, after the cold solid target, and after the plasma target at 5.5 ns of plasma expansion according to different theoretical models.

First, the beam after the 0.5 mm pinhole is employed to calculate the energy spectrum after the plasma target. The plasma after 5.5 ns of expansion was selected since this is the point at which ion stopping is at its maximum. The calculated energy spectra utilizing the different theoretical models presented in Chapter 2 are illustrated in Figure 4.12. The initial ion beam has an average energy of 5.0 MeV. After traversing the cold solid target with an areal density of 104 µg/cm^2, the ions exhibit a mean energy of 4.3 MeV, while the shape of the energy spectrum remains largely unaltered. In contrast, the energy loss is higher in the plasma case. The Vlasov, RPA, SSM, and Li-Petrasso (LP) theories yield mean energies that are close to 3.0–3.1 MeV. The BPS model predicts a mean energy of 3.3 MeV. The T-Matrix with $\lambda(v)$ model estimates a mean energy of 3.5 MeV. The Bethe and Bethe-Bloch formulas predict much higher energy losses, with many ions being stopped in the plasma target. These results are consistent with the calculations of the ideal ion beam. The energy spread of the initial beam and the different paths the ions

take through the plasma target cause the different ions to experience different energy losses. This results in the energy spectra within the plasma being broader than those of the initial beam.
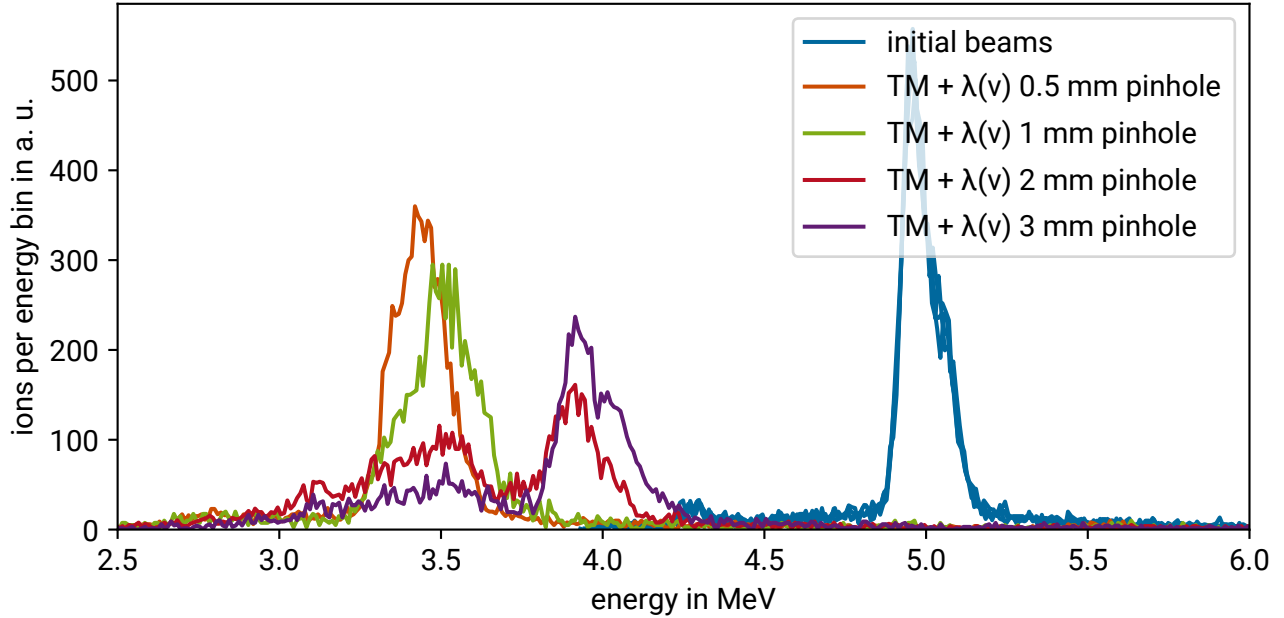

Figure 4.13: Energy spectra of the ion beam with different pinhole sizes before the target and after the plasma target at 5.5 ns of plasma expansion according to T-Matrix with $\lambda(v)$ formalism.

To demonstrate the necessity of the pinhole, ion beams with varying pinhole sizes were employed to calculate the energy loss using the T-Matrix with $\lambda(v)$ formalism. Figure 4.13 illustrates the energy spectra with different pinhole sizes before and after the plasma, at 5.5 ns of expansion. The particle numbers were scaled to ensure comparability. A comparison of the spectra with different pinhole sizes reveals that the mean energies are shifted upwards for larger pinholes. This is due to the outer plasma areas, where ion stopping is not at its maximum. Additionally, the energy width of the bunches widens with increasing pinhole size. This is caused by the inhomogeneity of plasma parameters in the outer regions (see Section 4.2). The pinholes with a diameter of 2 mm and above encounter the boundaries of the plasma, where the Lagrangian grid introduces numerical errors. These errors result in the generation of a double-peak structure that is physically incorrect and would not be observable in the experiment. The inclusion of inhomogeneous plasma boundaries is suboptimal in both the simulated and real case. The mean energies and energy widths of the bunches after the plasma with different pinhole sizes are summarized in Table 4.2. It can be observed that as the pinhole size decreases, the mean energy loss increases, while the energy spread of the bunch after passing through the plasma decreases.

Table 4.2: Mean energy and energy spread of the carbon ion beam with different sized pinholes passing through the plasma after 5.5 ns of expansion. For pinhole sizes of 2 and 3 mm, it is necessary to take into account the presence of numerical errors.

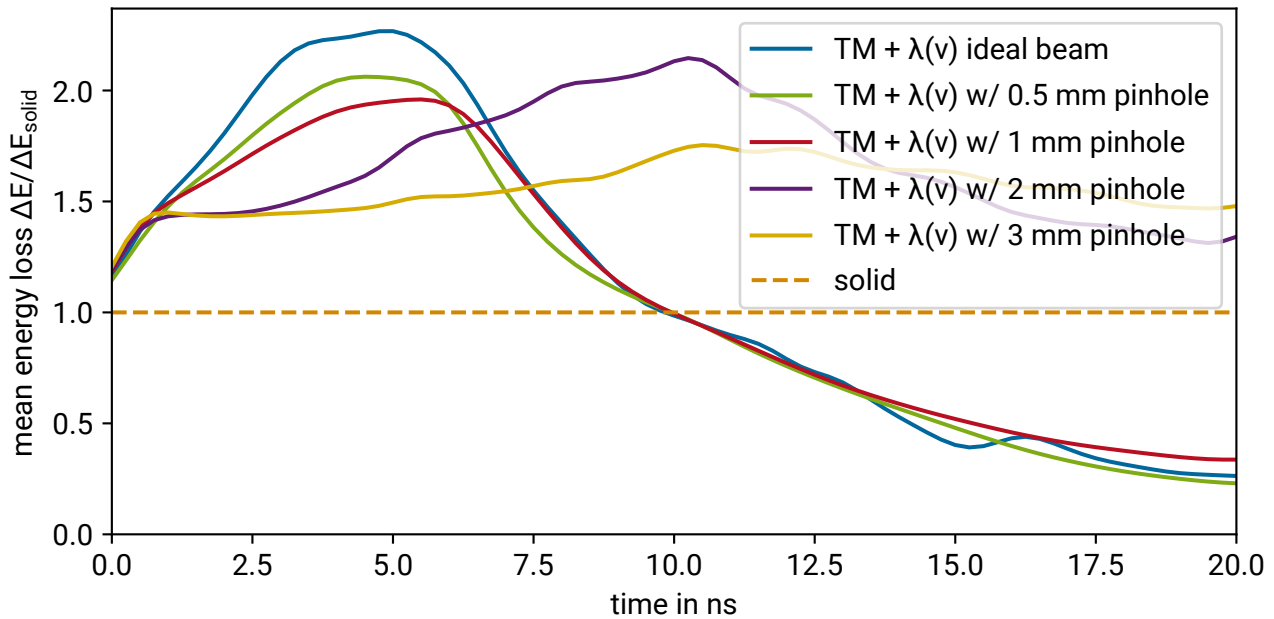| pinhole size	0.5 mm	1 mm	2 mm	3 mm
mean energy	3.49 MeV	3.55 MeV	3.67 MeV	3.88 MeV
energy spread (FWHM)	0.20 MeV	0.23 MeV	(0.69 MeV)	(0.19 MeV)

Figure 4.14: Comparison of the mean energy loss of the ideal carbon ion beam with the simulated beam with different pinhole sizes over the plasma expansion time.

Figure 4.14 depicts the mean energy losses normalized to the energy loss in the solid target as a function of plasma expansion time for different pinhole sizes. For comparison, the results of an ideal monoenergetic beam with no spatial size and an energy of 5.0 MeV are also shown. To account for the temporal length of the ion bunch, a Gaussian filter with a full width half maximum of 1 ns was applied to the results. It can be observed that the results of the simulated beam with the 0.5 mm and 1 mm pinholes exhibit a similar trend to those of the ideal beam. The 0.5 mm pinhole exhibits a deviation of 21 % of the energy loss in the solid target at the maximum, while the 1 mm pinhole exhibits a deviation of 31 %. The larger pinholes include the boundaries of the plasma, which are subject to numerical errors due to the limitations of the Lagrangian grid. These errors become more pronounced with increasing expansion time (refer to Section 4.2), as the outcomes do not align with the ideal beam results. The unphysical results would not be observable in the experiment. It is evident that smaller pinholes are more desirable.

This chapter presented the successful modeling of the planned stopping power experiment. The calculations revealed the required energy resolution for obtaining meaningful results. The next chapter showcases preparatory experiments that demonstrate the generation of the necessary ion beams. These ion beams were utilized to determine their stopping power in a solid foil, predicting the energy resolution of the planned stopping power experiments and demonstrating their feasibility.

5 Preparatory Experimental Campaigns

It is important to demonstrate the production of the desired ion beams. To achieve this goal, I conducted preliminary beamtimes, during which I measured the stopping power in a solid target. This chapter discusses the experimental campaigns conducted as preparation for the stopping power experiment. The experiments were conducted in three separate beamtimes. Two beamtimes, held in January 2021 and January 2024, were dedicated to carbon ions, while one beamtime, held in June 2022, was dedicated to protons. The initial section describes the various diagnostics used depending on the experimental requirements (refer to Section 5.1). The second section outlines the experimental setup employed during the beamtimes (refer to Section 5.2). The following section describes the generation of the desired proton and carbon ion beams (refer to Section 5.3). Subsequently, the measurement of the stopping power in a solid foil using these beams is presented (refer to Section 5.4). The final section discusses the implications of these results for measuring stopping power in a plasma (refer to Section 5.5).

5.1 Diagnostics

During preparatory beamtimes, three categories of diagnostics are utilized. Firstly, radiochromic films are used as spatial diagnostics to determine the size and position of the beam. Secondly, a diamond detector and a fast Faraday cup are used to determine the temporal shape of the ion bunches, specifically to measure the bunch length. Finally, a photodiode, scintillator, and diamond detector are used for the time of flight measurement to determine the energy of the ions.

5.1.1 Transversal Beam Diagnostics

Radiochromic films (RCFs) are commonly used to diagnose laser-accelerated protons in many laboratories due to their inherent insensitivity to electromagnetic pulses (EMP) generated during laser-matter interaction. RCFs are utilized in radiochromic imaging spectroscopy (RIS) to characterize the TNSA source and adjust the LIGHT beamline at various locations. They are also used to measure the focal spot size in the middle of the Z4 target chamber. For additional information on distinguishing between types of ionizing radiation, determining deposited energy from RCF scans, and calibrating different RCF batches with respect to RIS, please refer to Schmitz et al. 2022.

RCFs are transparent plastic films containing polymers that turn deep blue by solid-state polymerization in proportion to the irradiation dose received (McLaughlin et al. 1996). These radiochromic films (RCFs) usually consist of a radiation-sensitive layer (active layer) and a protective layer (passive layer) with a thickness of several micrometers. RCF stacks are configured based on the ion species and energy that is detected. The energy deposition in the active layers of an RCF is different for different types of ionizing radiation generated by the TNSA mechanism. Gamma rays and electrons generated during the TNSA

process (Wilks et al. 2001) penetrate the entire stack and deposit a small amount of kinetic energy in all active layers, whereas the accelerated ions are stopped in the RCF stack. According to the Bragg curve, a large fraction of their energy is deposited in a small region. The energy loss per distance of a charged particle in matter is proportional to the Z_{eff}^2 of the projectile. As a result, all ion species in the MeV range, except for protons, are stopped within the first few µm of the first RCF. The desired protons and carbon ions with 0.6 MeV/u have a range of 9 µm and 8 µm, respectively, in plastic. Since the passive layer of the used RCF HD-V2 from Ashland (*Gafchromic™ HD-V2 films* 2024) has a thickness of 97 µm, only a single RCF with the active layer facing the beam is used in the experiments reported in this chapter. For protons with higher energy, a small stack is typically used, where the appropriate proton energy is stopped in an active layer (James F. Ziegler et al. 1985).

5.1.2 Longitudinal Beam Diagnostics

To determine the temporal shape of the ion bunch, a diamond detector is used. Diamond's electronic properties, including its high charge carrier drift velocity and wide band gap, make it an excellent material for particle detection in harsh environments due to its radiation hardness (Berdermann et al. 2010; Witold Cayzac et al. 2013). Artificially produced chemical vapor deposited (CVD) diamonds were utilized to establish quality standards and ensure scientific reproducibility. Diamond detectors are classified as semiconductor detectors and usually consist of a parallel-plate geometry, which includes two electrodes surrounding the diamond. When a voltage is applied, the diamond creates a solid-state ionization chamber. These detectors operate by detecting ionizing particles, such as X-rays, ions, or electrons, that penetrate the diamond and generate electron-hole pairs through ionization processes. The charge carriers quickly thermalize and drift toward the electrodes, resulting in an image charge based on the applied field geometry. The compensating current generated in the external circuit is then recorded using a digital oscilloscope. A diamond membrane detector uses a diamond in which the crystallites all have the same orientation. The experimental campaigns with the LIGHT beamline typically use an etched single crystal (sc) diamond membrane detector with a thickness of 6 µm and a detection area of 0.5 mm. The diamond detector has a time response of $t_{\mathrm{FWHM}} = (113 \pm 11)\,\mathrm{ps}$ (Jahn et al. 2018).

During the last beamtime with carbon ions, a fast Faraday cup (FFC) was additionally used to measure the temporal shape of the ion bunch. A Faraday Cup is a conductive cup designed to catch charged particles in vacuum. The fast Faraday cup generates signals accurately and proportionally to the beam being measured with fast response time and low distortion and has a wide bandwidth in the frequency domain. The diameter of its entrance hole is 0.8 mm and it has a wide bandwidth of 20 GHz. The FFC used in this work was a loan from the beam diagnostics department of GSI. More details about it can be found in Singh et al. 2021 and Mal et al. 2022.

5.1.3 Time of Flight Diagnostics

The time of flight (ToF) method, commonly employed in various scientific fields, is a technique used for energy measurements. It relies on the principle of measuring the time it takes for a particle to travel a certain distance. In this method, multiple detectors are strategically placed at different distances from the source of the particle. The energy of the particle can be accurately determined by analyzing the time it takes to reach each detector.

To initiate the acceleration at the TNSA target, a photodiode records the gamma flash produced by the impact of the PHELIX laser on the TNSA target. The rising edge of the photodiode signal corresponds to the time of flight of the electromagnetic radiation from its origin to the photodiode. The photodiode is usually placed in the Z4 target chamber facing towards the TNSA target.

A scintillator with a 5 mm hole is utilized for semi-destructive time of flight diagnostics. Scintillators are frequently employed as particle counters and are intended to measure fluxes. When a particle enters a scintillator, it interacts with the electrons, causing energy loss and generating fluorescence photons. These photons are subsequently detected using photodiodes. In this study, a BC-442Q plastic scintillator manufactured by the company Saint Gobain was used (*Fast Timing BC-418, BC-420, BC-422, BC-422Q | Luxium Solutions* 2024). The scintillator has a decay time of 0.7 ns and emits light at a wavelength of 355 nm upon energy absorption. The scintillator's hole allows ions located in the middle of the beam to pass through while stopping those located on the periphery. The ions that are stopped in the scintillator generate fluorescence photons, which are then detected by an AXUV20HS1 photodiode by Optodiode. This provides a start signal for the ToF measurement.

A fourfold-segmented diamond detector with an area of $10 \times 10 \, \text{mm}^2$ and with a thickness of $19 \, \mu\text{m}$ was used as a stop detector (Wamers 2006). This detector has a time resolution of $110 \, \text{ps}$.

5.2 Experimental Setup

The desired proton and ion bunches were generated using the LIGHT beamline. The goal was to generate C^{4+} ions with an energy-to-mass ratio of 0.6 MeV/u, and protons with an energy of 0.6 MeV. The cavity was set up to compress the beam to the shortest possible bunch in the center of the Z4 target chamber, where the plasma target will be placed (refer to Chapter 3). This reduces the influence of the hydrodynamic expansion of the plasma target.
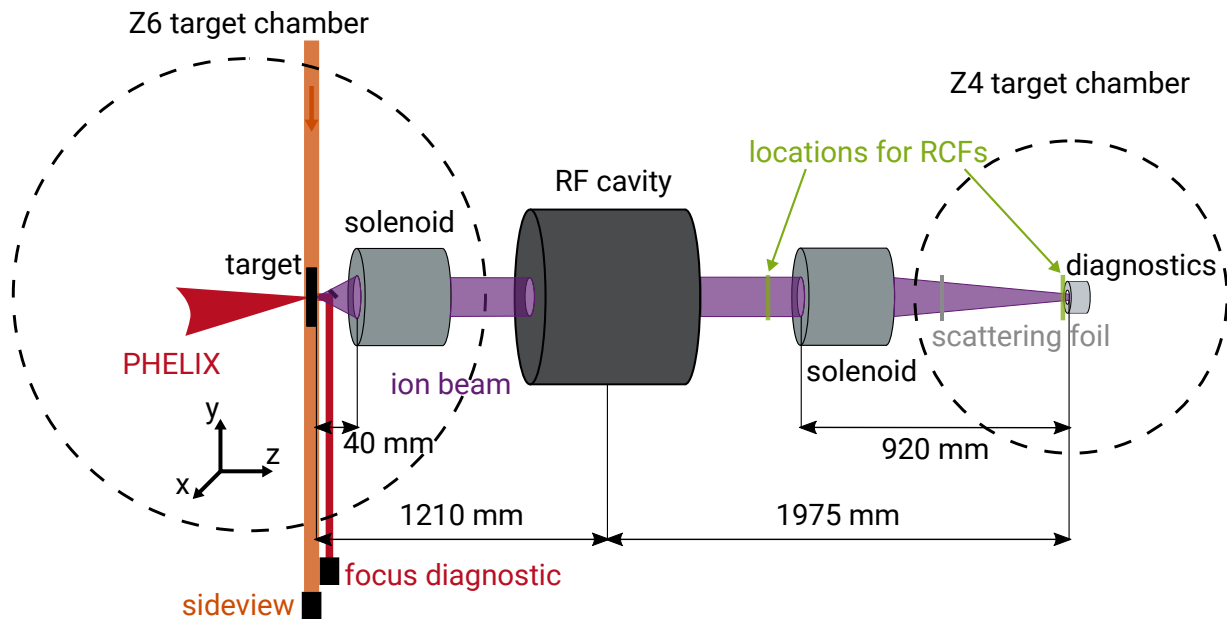

Figure 5.1: Schematic setup of the preparatory experimental campaigns to generate the desired ion/proton beams for stopping power experiments with the LIGHT beamline.

The experimental setup was chosen to be identical to that of the planned stopping power experiment with diagnostics placed inside the Z4 target chamber instead of the plasma target (see Figure 5.1). The distances seen in 5.1 were the same for both the carbon ions and protons.

The LIGHT beamline utilizes the PHELIX laser to accelerate protons and ions through the TNSA mechanism within the Z6 target chamber, as previously described. Once the PHELIX beam enters the Z6 target chamber, it is reflected by a mirror onto an off-axis parabola, which then focuses the beam on the TNSA target. The alignment of the PHELIX beam's focus and the TNSA target is achieved through the use of a sideview and a focus diagnostic. The sideview images the TNSA target onto a camera, while a laser pointer serves as a backlight. The focus diagnostic, on the other hand, images the focal spot of the PHELIX (see Figure 5.1). The first optics of the focus diagnostic are mounted on a motorized linear stage, which allows them to be moved away from the beamline axis.

The divergent protons and ions were captured and transported by the two solenoids. The first solenoid was adjusted with an RCF located after the RF cavity, where a small diagnostics chamber is located, and with an RCF in the middle of the Z4 target chamber (see Figure 5.1). The RCF's active layer faced the beam, as the slow protons and the carbon ions would be stopped in a passive layer (refer to Section 5.1). The RCF was used to adjust the positioning and magnetic field strength of both solenoids. The solenoid's alignment is determined by the beam's position on the RCF. The optimal alignment of the first solenoid

is essential for maximizing its capture efficiency, which is the reason it is mounted on a hexapod. The magnetic field strength of the second solenoid was also adjusted using an RCF in the center of the Z4 target chamber. The size of the beam in the active layer determines the adjustment of the solenoid's magnetic field strength. Due to the short distance between the second solenoid and the middle of the Z4 target chamber, the alignment is less demanding. Therefore, it is placed on a manually adjustable table outside of the vacuum. A PEEK tube is laid through the solenoid for the protons to pass through in the vacuum.

To compress the bunch temporally using the RF cavity, the temporal beam profile of the bunch was measured with the ultra-fast diamond membrane detector. The detector was positioned at the focal spot in the center of the Z4 target chamber to capture this temporal information. To eliminate the transverse filamentation of the beam caused by imperfections in the magnetic field of the solenoid due to its connection cables (Metternich et al. 2022), a Mylar scattering foil is placed in front of the diamond detector (see Figure 5.1). The positioning and the thickness varied for protons and carbon ions. A photodiode adjacent to the diamond detector measures the electromagnetic radiation resulting from the interaction between the PHELIX laser and the TNSA target. The start time of the ions can be determined using the rising edge of the photodiode signal.
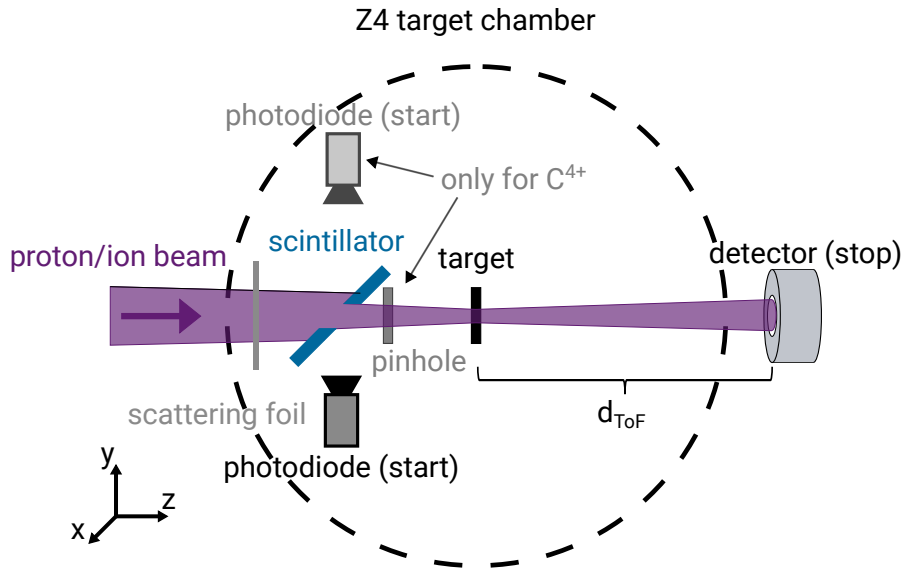

Figure 5.2: Schematic illustration of the stopping power experiment with the LIGHT beamline in a cold carbon foil.

In the stopping power experiment, the transported protons and ions after the scattering foil were utilized. This process disrupts filamentation in the beam, ensuring a homogeneous beam passes through the stopping target. The scattering foil slightly reduces the energy of the projectile (500–600 keV/u). The projectile beams passed through a scintillator with a hole in it (see Figure 5.2) and were detected with a photodiode that provided the start signal for the ToF measurement (refer to Section 5.1). For the stopping power experiment with carbon ions, two photodiodes were used to increase the dynamic range of the starting signal and therefore increase its reliability. The angle and distance of the scintillators were adjusted to ensure that their sensitivities were different. To ensure the detection of a usable signal, the more sensitive photodiode is utilized for low radiation of the scintillator, while the less sensitive photodiode is used for high radiation when the more sensitive photodiode saturates. The protons and ions that passed through the aperture lost energy within the carbon foil located in the focal spot of the beam. Following a time of flight distance d_{ToF} a diamond detector with an area of $10 \times 10 \, \text{mm}^2$ and with a thickness of $19 \, \mu\text{m}$ is

employed to measure the stop signal (refer to Section 5.1). The stopping target was a carbon foil with an areal density of approximately $100\,\mu g/cm^2$. For the carbon ion experiment, a pinhole with a diameter of $0.5\,mm$ was placed behind the scintillator to mimic the stopping power experiment with the plasma. This pinhole ensures that the ions traveling through the plasma target (refer to Section 4.2) only interact with the spatially homogeneous part of the plasma.

The following sections present the generated projectile beams and the results of the stopping power experiments conducted with those beams in a solid foil.

5.3 Ion Beam Generation

The experimental results of the projectile beam generation first for protons and then for carbon ions (C^{4+}) are presented and compared to the beamline simulations (refer to Section 4.1) in this section.

5.3.1 Protons

As previously stated, this preparatory beamtime aimed to transport protons with an energy of $0.6\,MeV$, to compress them temporally to the shortest possible bunch length and to focus the beam transversely in the center of the Z4 target chamber.

Proton Acceleration

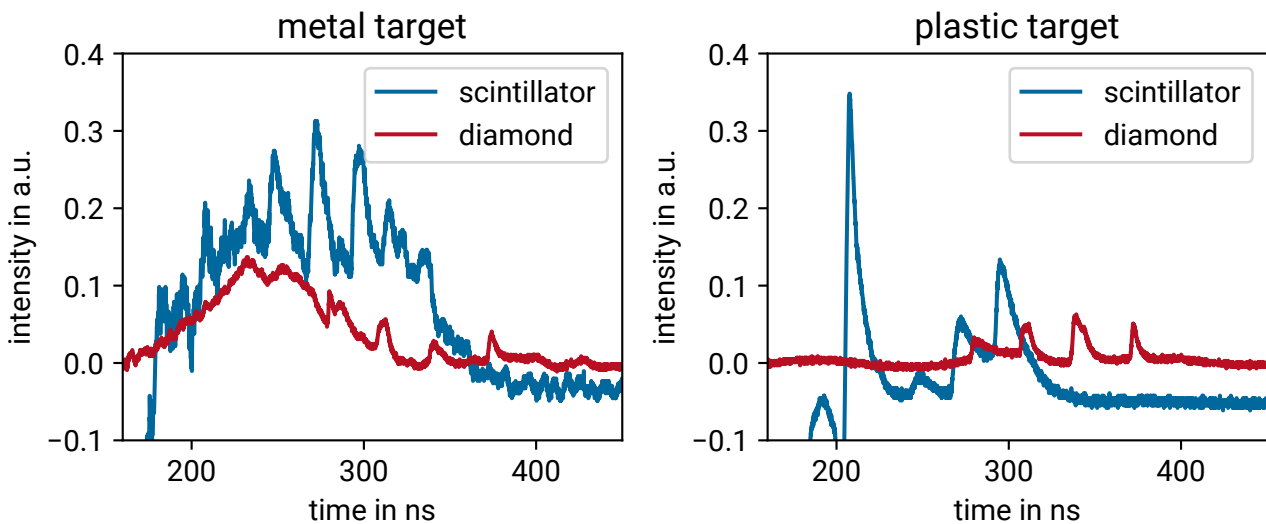Figure 5.3: Comparison of the temporal signal of a diamond detector and a scintillator with a photodiode affected by EMP, when using a metal target on a metal holder (left) and a plastic target on a plastic holder (right).

This experimental campaign also aimed to identify the most suitable TNSA target for conducting proton stopping power experiments. The objective is to reduce the electromagnetic pulse (EMP) generated during

the interaction of the laser with matter. To achieve this, a range of TNSA targets were utilized and various target holders were tested. The signals from the ToF detectors were compared for different target setups, including 5–20 μm gold targets and 10 μm tungsten targets. No discernible differences in behavior between the two types of targets were observed. In addition, 500 nm polystyrene targets were tested and a significant decrease in the EMP was detected by the time of flight diagnostics. The targets are usually mounted on an aluminum holder, but it was replaced with a 3D-printed PETG (polyethylene terephthalate glycol-modified) holder. This also reduced the noise and ringing caused by the EMP. Figure 5.3 shows the temporal signal of the diamond detector and the scintillator with a photodiode (refer to Section 5.1) for the metal target with the metal holder and the plastic target with the plastic holder. The scintillator was placed in the Z4 target chamber, and the diamond detector was placed approximately 80 cm behind the middle of the Z4 target chamber. The noise significantly reduces with the plastic target, particularly for the signal measured with the scintillator. The peaks corresponding to particle bunches are easily recognizable with the plastic target. The reduction of EMP improves the signal on the diagnostics and enables more reliable measurements.

The divergent laser-generated protons with the desired energy of 0.6 MeV are captured and transported using a solenoid.

Transport and Focus

Transporting protons with an energy of 0.6 MeV is a challenging task with the current solenoid setup in the LIGHT beamline. The inverse focal length of a solenoid, f^{-1}, is proportional to $(qB/p)^2$, where q is the charge and p is the momentum of the projectile, and B is the magnetic field strength of the solenoid. Therefore, the magnetic field and thus the currents ($B \propto I$) required for the magnets to handle low-energy protons is significantly low, ranging from 1–2 kA. The current pulsed power supplies that drive the magnets are not designed to operate at such low currents. To solve this problem, the protons' passage through the pulsed solenoid was timed to coincide with the falling edge of its magnetic field. This resulted in the protons experiencing a lower magnetic field than usual (refer to Figure 5.4). A successful transportation of protons was achieved using this method.
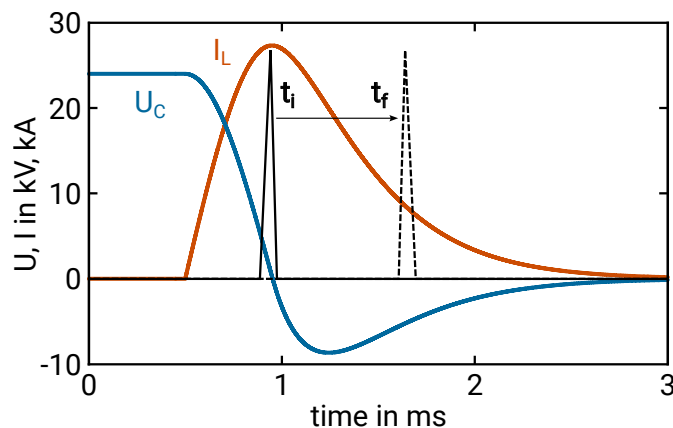

Figure 5.4: Current (orange) and voltage (blue) of the solenoid and its capacitor over time. t_i is the usual time of the proton bunch passing through the solenoid. t_f is the timing that needs to be used to reach lower currents and lower magnetic fields. This graph was adapted from Brack 2022.

The focal spot of the transported protons, which contained all transported protons, was measured using an HD-V2 RCF (refer to Section 5.1). The evaluated RCF is depicted in Figure 5.5. A **focal spot radius of (2.82 ± 0.03) mm**, which contained 50 % of the protons, was achieved (red circle). The minimum size is limited by the shortest achievable distance between the second solenoid and the focus position, and the transverse emittance of the beam. The measured focal spot is smaller than the simulated focal spot radius of 4.45 mm, a discrepancy that currently cannot be explained.
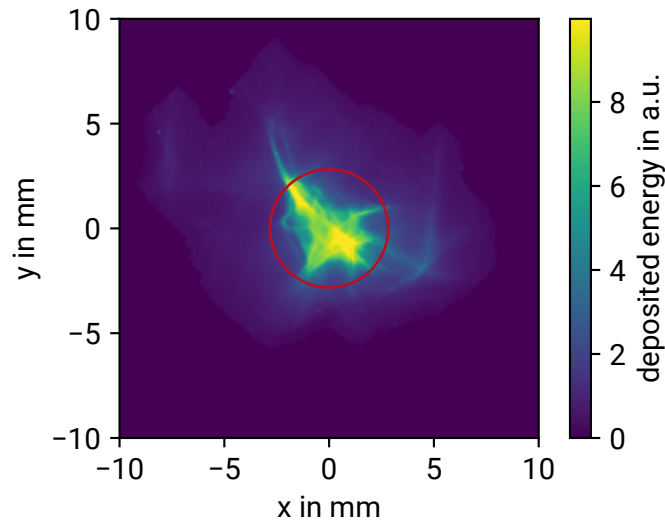

Figure 5.5: Focal spot of protons measured with an RCF in the center of the Z4 target chamber. The smallest circle that contains 50 % of the deposited energy, with a diameter of (2.82 ± 0.03) mm, is depicted in red.

Temporal Compression

The following step involves compressing the bunch using the RF cavity. To eliminate the transverse filamentation of the beam caused by imperfections in the magnetic field of the solenoid due to its connection cables (Metternich et al. 2022), a 1 µm thick Mylar scattering foil is placed 320 mm in front of the diamond detector. This results in a mean scattering angle of 21 mrad for 630 keV protons, which corresponds to a location deviation of 6.8 mm over the 320 mm distance, according to SRIM (James F. Ziegler et al. 1985). Figure 5.6 (left) shows the signal of the diamond detector in conjunction with the simulated proton bunch. The protons with an energy of 0.6 MeV are expected to arrive at approximately $t = 295$ ns. It can be seen that the diamond detector did not detect the slow protons. To ensure that the magnets were transporting protons at the correct energy of 0.6 MeV, an RCF measurement was carried out. In front of the active layer of the RCF, Mylar foils of different thicknesses were placed to stop all protons up to a certain energy. Figure 5.6 (right) shows the RCF with three segments. The 12 µm Mylar foil stops all protons with an energy lower than 0.7 MeV ($t > 281$ ns), which is a significant amount. The 6 µm foil stops all protons with an energy lower than 0.45 MeV ($t > 351$ ns), and in the third segment, all protons deposit energy in the RCF. Since the segment with the 6 µm Mylar foil shows a considerable number of protons, it can be concluded that protons with an energy between 0.45 MeV and 0.7 MeV (281 ns $< t < 351$ ns) were transported but not detected by the diamond detector. It is suspected that the diamond detector has difficulty detecting low-energy ions due to their low energy deposition or low range in the diamond.
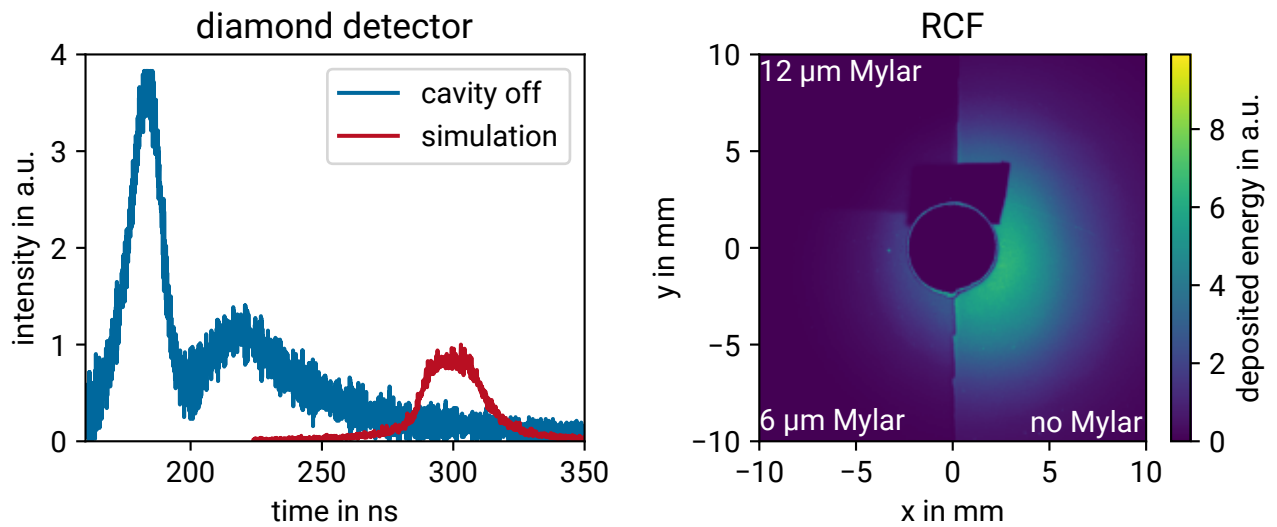
Figure 5.6: Diamond detector signal that corresponds to the time of flight of the protons that are transported through the LIGHT beamline as well as the time of flight of the transported protons in the simulation (left). RCF measurement of the proton beam with three segments (right): one with no Mylar foil, one with 6 μm (> 0.45 MeV) and one with 12 μm Mylar (>0.7 MeV) in front of it. In the middle of the RCF, there is a hole and a piece of tape.

Upon switching on the RF cavity, the intensity of the proton bunch with a time of flight corresponding to an **energy of (0.63 ± 0.01) MeV** increased due to the temporal compression. This increased intensity enabled the detection of the proton bunch by the diamond detector. The RF cavity's voltage and phase were then adjusted to achieve optimal temporal compression. Altering the phase of the RF cavity results in a different energy transfer to the nominal particle, while adjusting the voltage of the RF cavity changes the energy spread of the bunch, and consequently, the temporal bunch width at the diamond detector's position. Figure 5.7 displays the shortest measured proton bunch, revealing the presence of multiple generated bunches. This occurs because the temporal width of the transported protons is longer than twice the period duration when they reach the RF cavity, resulting in multiple peaks at the focal spot in the middle of the Z4 chamber. The energy transfer from the RF cavity to the protons is velocity-dependent due to the three accelerating gaps. Therefore, other energies are compressed at different distances (Metternich 2023). For most transported protons, their relative energy transfer is greater, causing them to compress at a shorter distance. The additional flight distance results in a U-shaped temporal profile of the bunch at the position of the diamond detector, as seen around 270 ns in Figure 5.7. In the planned stopping power experiments, the temporally compressed protons with an energy of approximately 630 keV will be used. The separation of the peaks in the measurement is straightforward because the plasma remains in a relevant state for only 12 ns (refer to Chapter 4) and only affects the peak of interest. The phase and voltage of each shot are measured to determine the precise cavity settings. The standard deviation of the measured cavity voltage is 1.23 %, while the measured phase has a standard deviation of 3.1°, equivalent to a 0.08 ns delay. The deviation in voltage affects only the bunch length, while the deviation in phase affects both the bunch length and the temporally compressed energy. A translated standard deviation of 642 eV/u in energy and 100 ps in pulse length was simulated. The shortest **bunch duration of (0.76 ± 0.04) ns** as shown in Figure 5.7 was measured with the diamond membrane detector. Although the flight times and temporal distributions show minimal deviations, the experimental bunch duration exceeds the simulated

bunch duration (see Table 5.1). A range of potential causes were examined, including the scattering foil, space charge effects, the non-negligible initial emittance of the TNSA-generated ion beam, and the radial dependency of the electric field within the RF cavity gaps. However, further examination of the observed phenomenon is necessary (Metternich 2023). Saturation effects in the diamond detector are considered a plausible cause and are investigated in the experimental campaign with carbon ions (see Section 5.3.2).
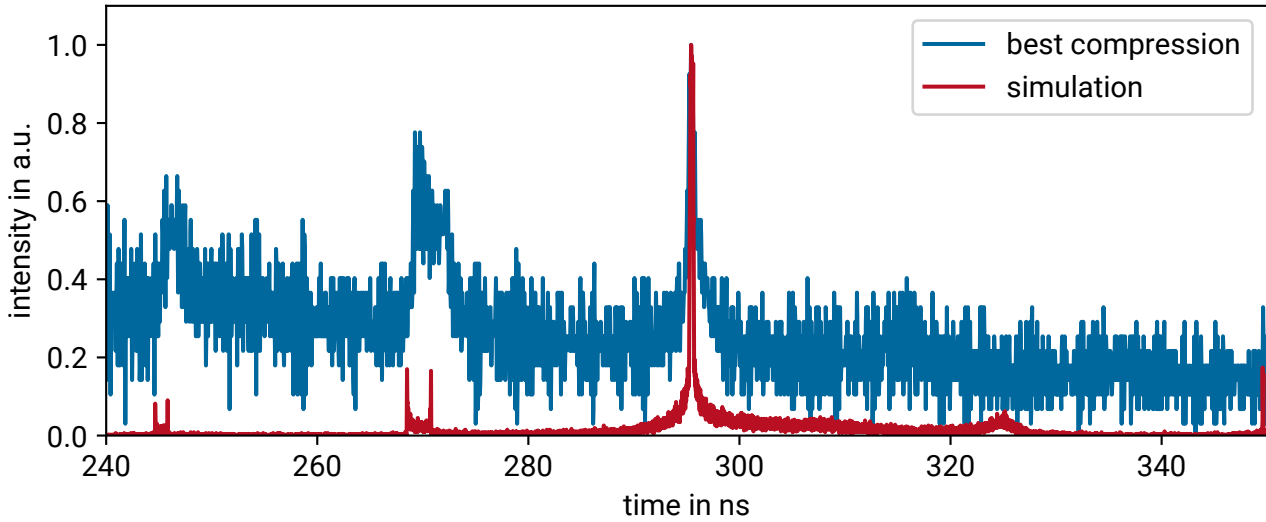

Figure 5.7: Measured and simulated time of flight of the temporally compressed protons. The measurement was conducted with a diamond membrane detector in the center of the Z4 chamber.

Estimated Number of Protons

Due to a limited understanding of the diamond detector's response at low energies, it cannot be assumed that the energy deposited on the RCF is solely from protons with an energy of (0.63 ± 0.01) MeV. Instead, the amount of transported protons was estimated by modeling their propagation through the beamline (see Section 4.1) using the proton distribution at the TNSA source, which was measured using radiochromic imaging spectroscopy (RIS) (Schmitz et al. 2022). This estimation resulted in **$(5.8 \pm 0.4) \times 10^8$ temporally compressed protons** with an energy spread of 2.4 %.

In Table 5.1 the parameters of the final proton bunch are compared to the simulation. The proton bunch is suitable for experiments on stopping power, despite being longer than predicted by simulations.

Table 5.1: Comparison between simulated (refer to Section 4.1) and measured parameters of the temporally compressed proton bunch.

parameter	experiment	simulation
mean energy	(0.63 ± 0.01) MeV	0.60 MeV
energy spread (width at 20 % of maximum)	not measured	2.4 %
temporal bunch width (FWHM)	(0.76 ± 0.04) ns	0.44 ns
focal spot radius (50 % encircled)	(2.82 ± 0.03) mm	4.45 mm
estimated number of protons	not measured	$(5.9 \pm 0.4) \times 10^8$

5.3.2 Carbon Ions

The objective of the preparatory beamtime with carbon ions was to transport carbon ions (C^{4+}) with an energy of 0.6 MeV/u and compress them temporally to the shortest possible bunch length in the middle of the Z4 target chamber while focusing the beam transversely.

Ion Acceleration

To accelerate carbon ions, usually heated targets consisting of carbon-containing materials are used. The target is heated to remove any hydrogen contaminants from its surface. This leads to a decrease in the number of accelerated protons and an increase in the acceleration of carbon ions (Hegelich et al. 2002). However, non-heated targets have also been tested to simplify the experimental procedure. The non-heated targets were made of carbon with an areal density of 650 µg/cm^2. The targets were manufactured by the target laboratory at GSI. The heated targets consisted of 10 µm thick tungsten foils with a 0.9 µm thick carbon coating on the backside. The target was heated to temperatures above 1000 °C using ohmic heating. This method produces heat by passing an electric current through the target, causing the contaminant layer to evaporate. To ensure accurate temperature measurement and reach the target temperature, a pyrometer was utilized. The target holder was used to hold the target under tension to prevent significant deformation due to thermal expansion.
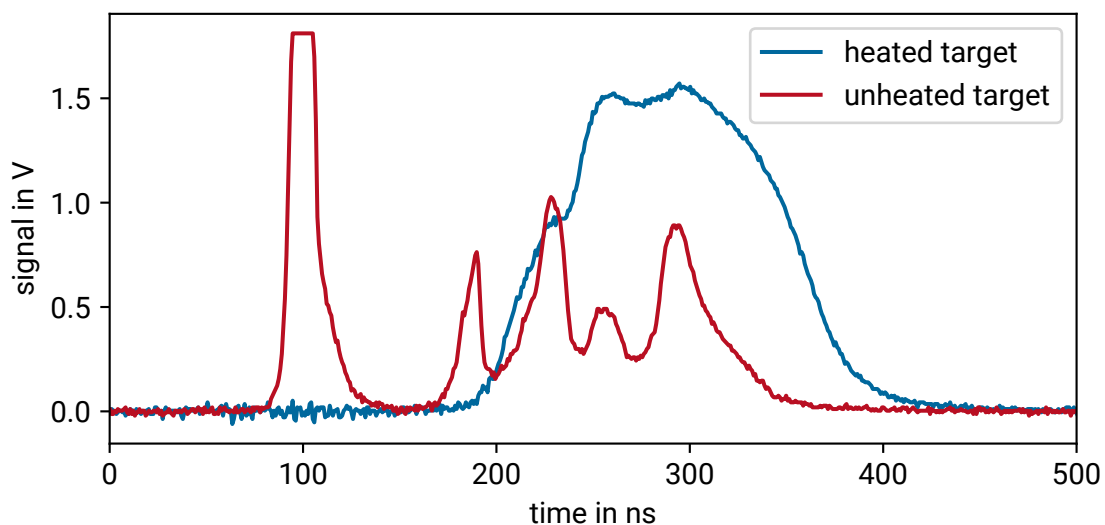
Figure 5.8: Diamond detector signal with a heated target (blue) and an unheated target (red) in the middle of the Z4 target chamber with cavity turned off.

Figure 5.8 displays the measurement obtained using the diamond membrane detector at the center of the Z4 target chamber for both heated and non-heated targets. The results demonstrate that heating the target not only increases the number of carbon ions (200–400 ns), but also eliminate the accelerated protons (98 ns). Other contaminants, such as oxygen and nitrogen, are also increased by heating the target, indicating that the target was not heated sufficiently to evaporate these contaminants or that these contaminants are present in the bulk of the target and not only on the surface. All the transported peaks are identified in Table 5.2 with their respective calculated flight times. The long falling edge at 342 ns

was attributed to N^{4+} ions. All the ions simultaneously transported by solenoids have the same magnetic rigidity, which is defined by their speed v, mass m, and charge q ($\propto \frac{mv}{q}$). Transported ions with a higher charge-to-mass ratio exhibit a higher velocity and thus a shorter flight time.

Table 5.2: All the ions transported by the solenoids with their respective calculated flight times (see Figure 5.8).

ion	H^+	N^{7+}	C^{5+}	O^{6+}	C^{4+}	N^{4+}
flight time	98 ns	195 ns	234 ns	260 ns	293 ns	342 ns

Transport and Focus

To prepare for the transportation of carbon ions, solenoids were set up to transport protons with an energy of 5.4 MeV, which have the same magnetic rigidity as C^{4+} ions with an energy of 7.2 MeV (0.6 MeV/u). This results in the simultaneous transport of 7.2 MeV C^{4+} ions. The validity of this was confirmed through beamline simulations (Metternich 2023). Using protons to adjust the beamline eliminates the need to heat the target for the adjustment process. Additionally, an RCF stack with an active layer at the appropriate energy can be utilized (refer to Section 5.1). After successfully transporting the proton beam, either carbon targets or heated tungsten targets with carbon sputtered on them, depending on the corresponding measurement's necessity were used.
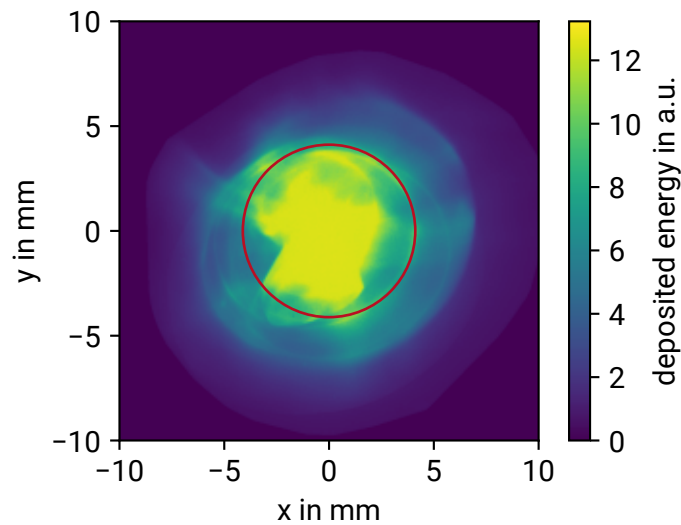
Figure 5.9: Focal spots of carbon ions (C^{4+}) achieved with the LIGHT beamline measured with an RCF in the center of the Z4 target chamber. The smallest circle that contains 50 % of the deposited energy, with a diameter of (4.11 ± 0.02) mm, is depicted in red.

To measure the focal spot size, a heated target was used to accelerate as many carbon ions as possible. An HD-V2 RCF with the active layer facing the ion beam was used to measure the focal spot. Figure 5.9 shows the focal spot of all carbon ions, regardless of their charge state, as measured by the RCF. The RCF's active layer captures all or a significant portion of the kinetic energy of all ion species and charge states with velocities up to 0.75 MeV/u. The achieved focal spot radius, containing 50 % of carbon ions, was measured

to be **(4.11 ± 0.02) mm** (red circle). Similarly to the measured proton focal spot, the carbon ion focal spot is smaller than the radius of the simulated best possible focal spot radius of 5.45 mm.

Temporal Compression

To temporally measure and subsequently compress the ion bunch, a scattering foil (2 μm Mylar) was placed 300 mm in front of the diamond detector in order to disrupt the transverse filamentation of the beam (Metternich et al. 2022). The average scattering angle for C^{4+} ions with an energy of $E = 7.2$ MeV is 13 mrad, which corresponds to a positional deviation of 3.9 mm over a distance of 300 mm, as calculated by SRIM (James F. Ziegler et al. 1985).
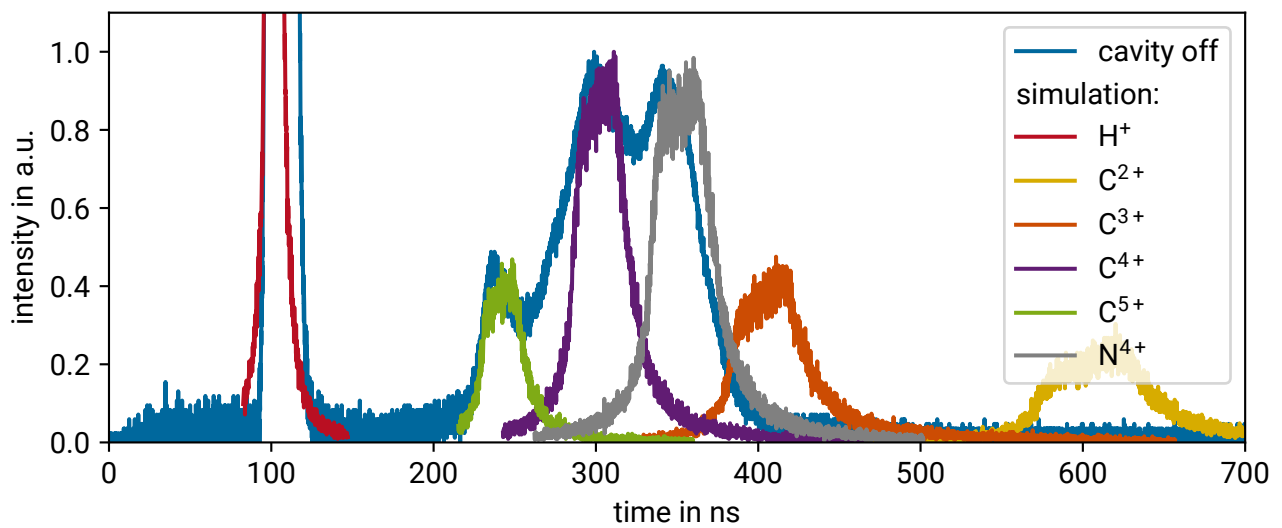
Figure 5.10: Diamond detector signal that corresponds to the time of flight of the ions transported through the LIGHT beamline as well as the time of flight of the transported ions in the simulation. The signals are normalized to the C^{4+} peak.

Figure 5.10 displays the temporal shape of the bunch with the RF cavity turned off, along with the corresponding time of flight signals of the carbon ions in the simulations. It is clear that, despite heating the target, contaminants remained present. The detected peaks correspond to protons, C^{5+} and C^{4+} ions, respectively. Notably, there is no signal detected for C^{3+} and C^{2+} ions. The peak at 340 ns is attributed to N^{4+} ions with $E = 6$ MeV (calculated flight time of 358 ns). However, it is unclear why the diamond detector does not detect low energy ions ($\lesssim 0.4$ MeV/u). According to SRIM, these ions are not stopped within the 2 μm thick Mylar foil. The Thomson parabola spectra (Ding 2018) and simulations were used to determine that the space charge effects for C^{3+} ions are lower than those for C^{4+} ions, ruling out space charge effects as the cause of the missing signal. Similar to the proton measurements, the data indicates that the efficiency of diamond detectors in detecting low-energy particles may be questionable. However, it does demonstrate the successful transport of C^{4+} ions with an **energy of** $E = (7.2 \pm 0.2)$ **MeV**. (Metternich 2023)

To compress the C^{4+} ions temporally, the voltage and phase of the RF cavity were incrementally adjusted after each shot. Figure 5.11 shows the shortest diamond detector signal achieved through this procedure (orange), along with the signal of the uncompressed beam (blue) and the temporally compressed beam from the simulation (green).
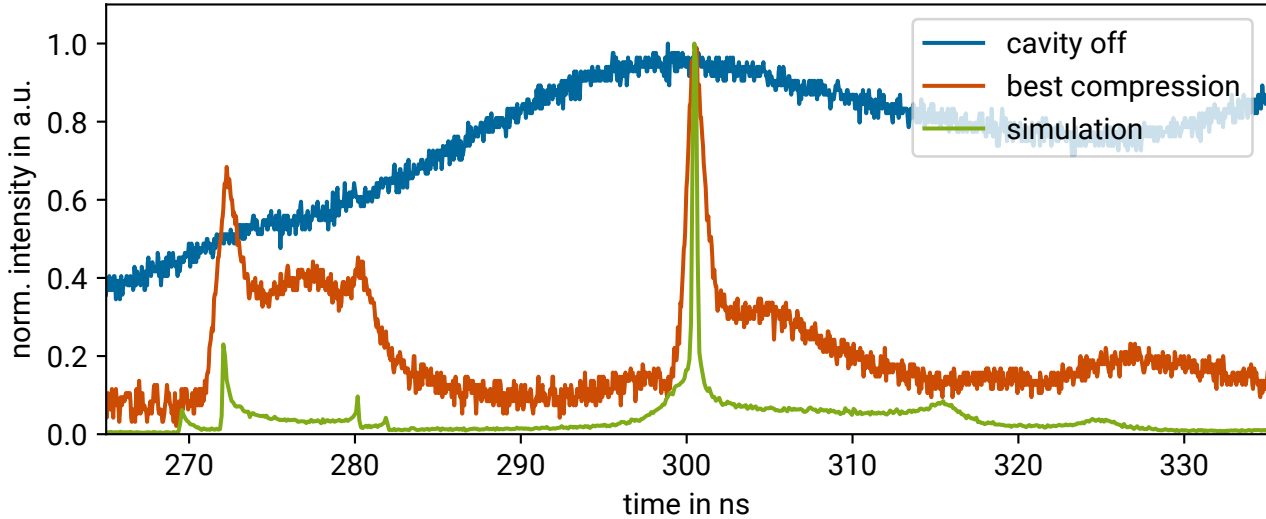

Figure 5.11: Measured and simulated time of flight of the temporally compressed C^{4+} ions along with the measured time of flight of the uncompressed C^{4+} ions. The measurement was conducted with a diamond membrane detector in the center of the Z4 target chamber.

The flight times and temporal distributions of the different carbon ion bunches from measurements and simulations exhibit only minor variations. The shortest duration of the bunch achieved is $\tau = (1.23 \pm 0.04)$ **ns (FWHM)**, which is 60 % longer than the shortest proton bunch achieved and three times larger than the predicted value from simulations (refer to Table 5.3). As previously described, several potential causes were examined and eliminated (Metternich 2023), leaving saturation effects in the diamond detector as a potential cause of the observed phenomenon. To test this hypothesis, an FFC (refer to Section 5.1) was used to measure the pulse length in a different experimental campaign. Figure 5.12 shows the FFC signal alongside a diamond signal obtained with reduced ion flux. The measured bunch lengths are similar to those measured in the previous experimental campaign. The signal of the diamond detector shows a long falling edge, which suggests the presence of saturation effects. In contrast, the FFC does not exhibit such behavior. The measured bunch length is approximately 30 % lower with the FFC, which is still significantly higher than predicted by simulations. This contradicts the hypothesis of diamond saturation. The remaining most probable cause of the underestimation of the bunch length is the inaccurate assumptions made about the longitudinal emittance growth when traversing the solenoids in the beamline simulations. To confirm this, it is necessary to measure both the emittance and the energy width of the transported ions at various locations in the beamline, especially before and after passing through a solenoid.
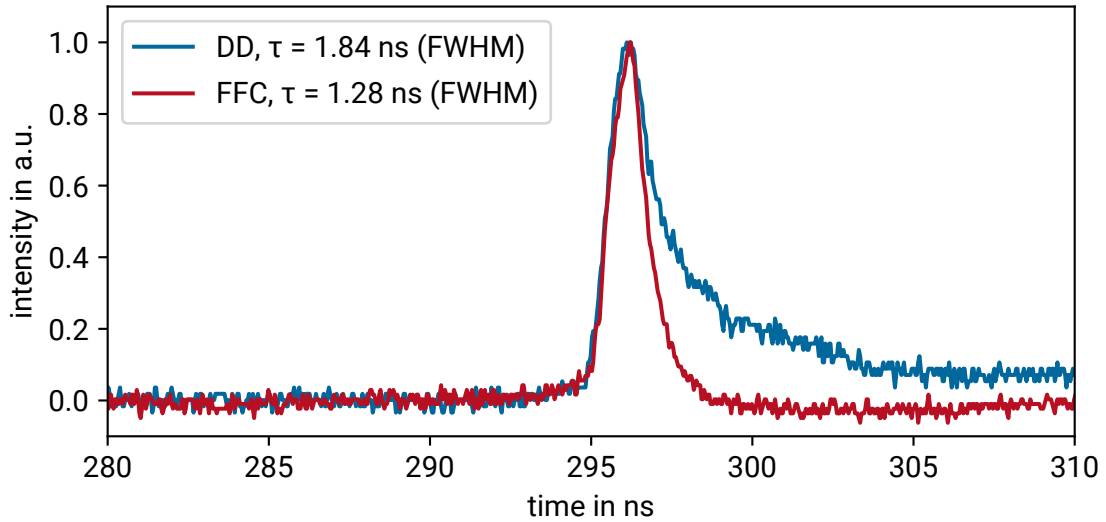
Figure 5.12: Diamond detector signal (DD) and fast faraday cup signal (FFC) of temporally compressed C^{4+} ions. The measurements were conducted in the center of the Z4 target chamber.

Estimated Number of Ions

To estimate the number of carbon ions transported, an HD-V2 RCF was positioned at the focal spot in the middle of the Z4 target chamber (see Figure 5.9). The deposited energy of the temporally compressed ion beam was measured by the RCF's active layer (refer to Section 5.1). The energy deposited by protons in the active layer can be neglected, as those with an energy of 5.25 MeV are not stopped in this layer and lose minimal energy (≈ 8 keV per proton). Ions with energies up to 10 MeV are stopped in the active layer. According to the measurements and simulations, the highest energy ions transported are C^{5+} ions with an energy of 12 MeV. They deposit approximately 80 % of their energy in the active layer. Therefore, for the estimation, it is assumed that the total energy deposited in the active layer corresponds to the energy of all transported carbon and nitrogen ions. The diamond detector faced difficulties in detecting lower energies, which made it impossible to determine the energy spectrum of the transported ions from the ToF data. Thus, the simulation results were used to estimate the energy spectrum of the carbon ions. The transported beam in the simulation comprises 21 % C^{2+}, 26 % C^{3+}, 40 % C^{4+}, and 13 % C^{5+} ions, and uses the Thomson parabola spectra measured in Ding 2018 to reconstruct the TNSA source. The total energy deposited in the active layer amounts to $E_{\text{dep}} = (2.0 \pm 0.6) \times 10^{10}$ MeV. The significant uncertainty is due to the lack of calibration in the used RCF lot, which required the use of a calibration from an older lot. The transported ion beam consists of $(3.6 \pm 1.1) \times 10^9$ carbon ions, of which $(1.4 \pm 0.4) \times 10^9$ are C^{4+} ions, assuming that the spectrum of the measured beam corresponds to the spectrum obtained from simulations. Simulations show that 14 % of transported C^{4+} ions can be temporally compressed, resulting in **$(2.0 \pm 0.6) \times 10^8$ compressed C^{4+} ions** during the experiment. (Metternich 2023)

Table 5.3 summarizes and compares the most important parameters of the final carbon bunch to the simulation. Although the ion bunch was longer than anticipated by the simulations, it is more suitable for stopping power experiments than the ion bunches used in previous experiments. It has three orders of magnitude more ions in a five times shorter bunch than previous stopping power experiments with linear accelerators (W. Cayzac et al. 2017).

Table 5.3: Comparison between simulated (refer to Section 4.1) and measured parameters of the temporally compressed carbon bunch.

parameter	experiment	simulation
mean energy	(7.2 ± 0.2) MeV	7.2 MeV
energy spread (width at 20 % of maximum)	not measured	2.2 %
temporal bunch width (FWHM)	(1.23 ± 0.04) ns	0.43 ns
focal spot radius (50 % encircled)	(4.11 ± 0.02) mm	5.45 mm
estimated number of C^{4+} ions	$(2.0 \pm 0.6) \times 10^8$	

5.4 Stopping Power Measurement in Solid Target

This section reports on experiments conducted during beamtimes on stopping power using a cold carbon foil. The stopping power for protons and carbon ions was measured.

5.4.1 Protons

The proton beam presented in Section 5.3.1 was used for a stopping power experiment. The protons lost energy as they passed through a carbon foil with an areal density of 105 µg/cm^2 and had a time of flight distance of $d_{\text{ToF}} = (0.818 \pm 0.002)$ m. Two shots without and two shots with the stopping target were conducted, in order to measure the energy loss of the protons in the carbon foil. Figure 5.13 illustrates the time signals of the start and stop detectors for a shot without and with the carbon foil. The observed variation in the baseline is attributed to the varying intensity of the gamma flash detected in the laser-matter interaction of the TNSA process.
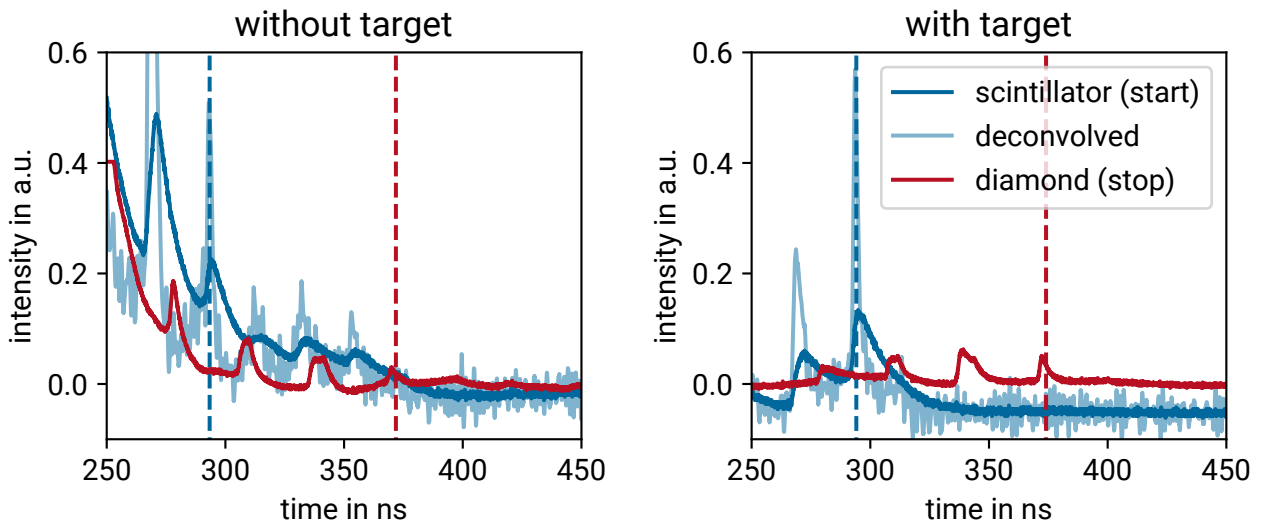

Figure 5.13: Time of flight measurements of the proton energy with a scintillator (start) and a diamond detector (stop). Time of flight measurement of initial proton energy without carbon foil (left). Time of flight measurement of final proton energy with carbon foil (right). The dashed lines show the center of mass of the proton bunch used for the stopping power measurement.

The scintillator signal was deconvolved using the response function of the AXUV photodiode, which was measured with a short-pulse laser. The laser pulse length was approximately 500 ps and was measured with a Det10A photodetector from Thorlabs. Deconvolving the AXUV signal with the Det10A signal produced the response function of the AXUV diode. The Det10A detector cannot be used with the scintillator because its sensitivity is too low for the radiation emitted by the scintillator. Figure 5.14 shows the resulting response function. A Wiener deconvolution was used to obtain both the response function and the deconvolved start signal.
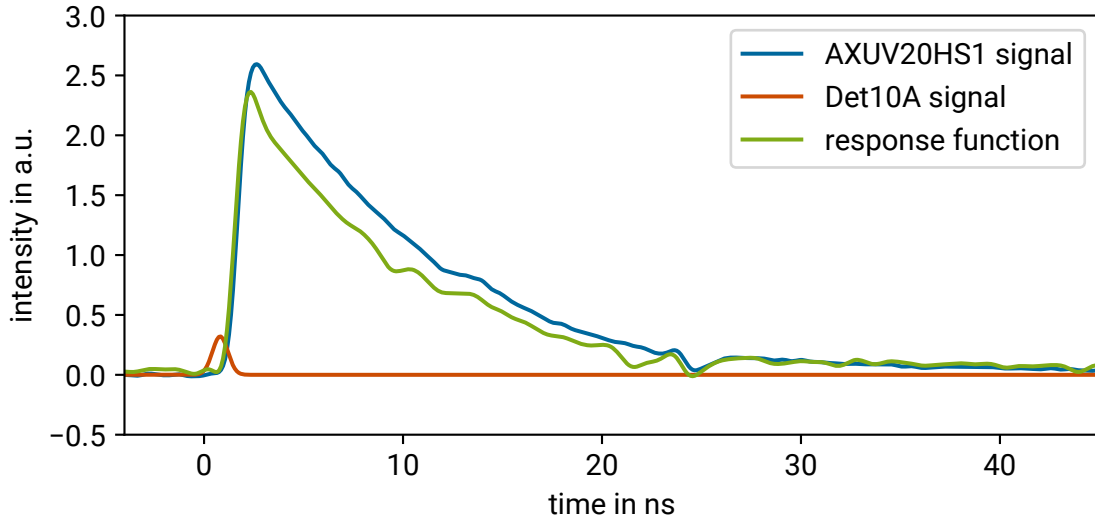

Figure 5.14: Response function of the AXUV20HS1 photodiode by Optodiode produced with a 500 ps laser pulse.

The responses of the scintillator and the diamond detector were not considered since both of them have fast rise and fall times ($\approx 10^{-9}$ s). The shots without the carbon foil are used to measure the initial energy of the proton bunch. The central energy was obtained by using the peaks' center of masses. An initial energy of $E_\mathrm{i} = (595 \pm 5)$ keV was determined. The final energy after the carbon target with an areal density of 105 µg/cm^2 was determined with the two shots in which the protons passed through the carbon foil. The signal was observed to shift towards later times, indicating a reduction in the energy of the protons. An energy of $E_\mathrm{f} = (566 \pm 4)$ keV was determined. Using the measured initial energy of the protons it is possible to calculate their energy after passing through the stopping foil with SRIM, which concludes to $E_\mathrm{f,SRIM} = (563 \pm 12)$ keV. The calculated and measured energies of the protons after passing through the carbon foil are within each other's error bars.

An **energy loss of** $dE = (\mathbf{29 \pm 6})$ **keV** was measured, corresponding to an uncertainty of 21 %. This uncertainty is due to the inaccuracy of the time measurements with the scintillator t_start and the diamond detector t_stop and the measurement of the time of flight distance d_ToF. Approximately 73 % of the uncertainty arises from the scintillator and the photodiode ($\Delta t_\mathrm{start} = 0.36$ ns), 20 % is due to the uncertainty of the time of flight distance ($\Delta d_\mathrm{ToF} = 2$ mm), and 7 % is attributed to the stop signal from the diamond detector ($\Delta t_\mathrm{stop} = 0.11$ ns).

5.4.2 Carbon Ions

For the stopping power experiment, a similar carbon ion beam was used as presented in Section 5.3.2. The time of flight distance was $d_{\text{ToF}} = (1.519 \pm 0.002)$ m, which was increased compared to protons due to the higher response of the diamond detector to carbon ions. However, during the experimental campaign with carbon ions, it proved challenging to obtain shots where both the start and stop detectors generated signals at the same time. This was due to time constraints and the limited number of shots that could be conducted with the final adjusted setup. To measure the initial energy, six shots were used where only the start detector received a signal, two shots where both the start and stop detectors received a signal, and four shots where only the stop detector received a signal. Three stop signals were measured when the stop target was in place. All shots are depicted in Figure 5.15. It is evident that during the three shots with the stopping target (orange), the ions arrived approximately 10 ns later at the stop detector. After considering all of the deconvolved start signals, the center of mass of the bunch arrives at the scintillator at $t_{\text{start}} = (292.9 \pm 0.8)$ ns (blue). The stop signals without the stopping target arrive at $t_{\text{stop}} = (453.3 \pm 0.7)$ ns (green), resulting in an initial energy per nucleon of $E_{\text{i}} = (503 \pm 7)$ keV/u. The stop signals with the stopping target, a carbon target with an areal density of $104 \, \mu\text{g/cm}^2$, average to (463.7 ± 0.8) ns (orange), resulting in a final energy of (442 ± 7) keV/u. The initial energy measurement was used by SRIM to calculate a final energy of (441 ± 9) keV/u, which falls within the error bars of the measurement.
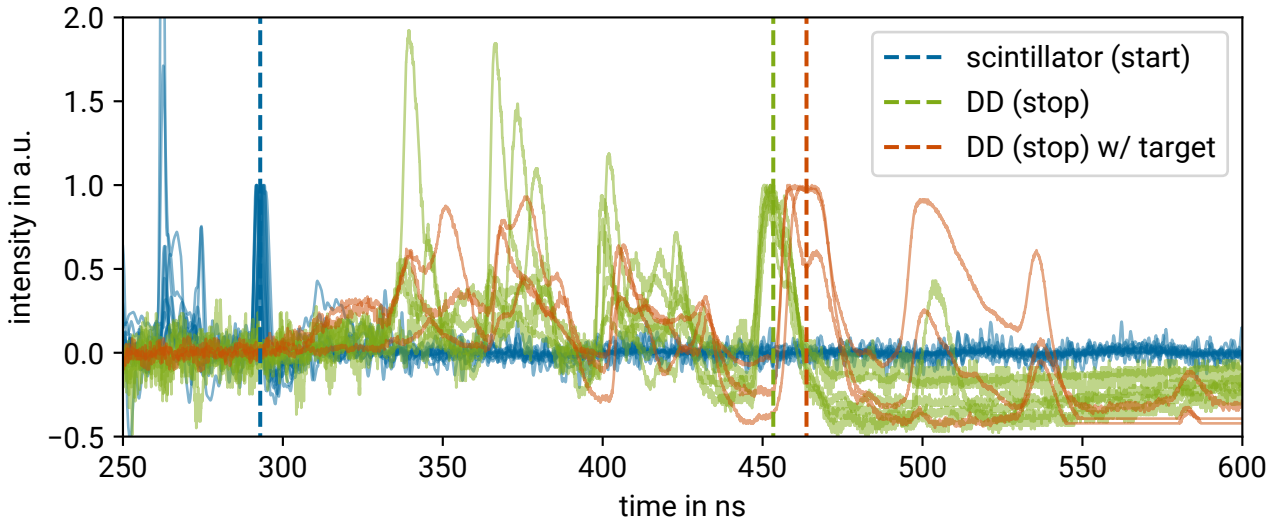
Figure 5.15: Time of flight measurements of the carbon ion energy with a scintillator (start) and a diamond detector (stop). The deconvolved signals of all measured start signals with scintillator and photodiode are shown in blue. The green lines represent all stop signals without a stopping target measured with the diamond detector, while the red lines represent all stop signals with the stopping target. The dashed lines indicate the average center of mass of the relevant peak for the respective signals.

The measured **energy loss is (61 ± 10) keV/u**, corresponding to a 16 % uncertainty. The uncertainties of the temporal signals t_{start} and t_{stop} were determined statistically using the standard deviations of the signals, resulting in $\Delta t_{\text{start}} = 0.79$ ns and $\Delta t_{\text{stop}} = 0.69$ ns. They contribute to the final uncertainty with 55 % and 41 %, respectively, while the uncertainty of the distance contributes with 4 %. The difficulties in obtaining signals for both diagnostics on the same shot necessitate the use of statistical uncertainty, which

increases the uncertainty compared to the measurement with protons. However, the increased time of flight distance (d_{ToF}) reduces the impact of the uncertainties when calculating the ion velocity, resulting in a smaller relative uncertainty of the energy loss.

5.5 Implications for Stopping Power Measurements in Plasma

In this section, the resulting proton and carbon ion beams are compared with the ion beam used in the stopping power measurements described in Section 3.1.1. This experiment had similar conditions to the one planned with the LIGHT beamline, as described in Section 3.2. To summarize the previous experiment, W. Cayzac et al. 2017 used the UNILAC ion source at GSI to provide nitrogen ions. The ions were passed through a 0.5 mm pinhole to reduce their size. The beam was then further degraded to reach the target energy of (0.586 ± 0.016) MeV/u where the projectile velocity is similar to the thermal velocity of the plasma electrons ($v_{\text{p}} \approx v_{\text{th}}$). The microbunches of the nitrogen beam contained around 10^3 ions and had a Gaussian temporal profile and a bunch width of 5.5 ns (FWHM). The main uncertainties in the stopping power calculations were due to the temporal averaging of the plasma parameters over the 5.5 ns and the low particle count, resulting in a low signal-to-noise ratio (refer to Section 3.1.1). The use of temporally compressed protons and C^{4+} ions from the LIGHT beamline for plasma probing offers several advantages, which will be discussed in the following.

The temporal width of the proton bunch and the C^{4+} ion bunch is (0.76 ± 0.04) ns and (1.23 ± 0.04) ns, respectively, which is five to seven times shorter. This reduces the need for time averaging in the stopping power experiment with the LIGHT beamline.

According to simulations (refer to Chapter 4), the particle number passing through the pinhole is expected to be around 0.15 %, which corresponds to 3×10^5 C^{4+} ions and 9×10^5 protons. Consequently, the LIGHT beamline yields approximately two to three orders of magnitude more particles in a single bunch than the UNILAC in the previous stopping power experiment (W. Cayzac et al. 2017), as well as in the proton bunch generated by Malko et al. 2022 through magnetic filtering of laser-accelerated protons (refer to Section 3.1). This enables an increase in the ToF distance, which in turn improves the energy resolution.

The stopping power experiments in a solid target provide information on the resolution of the measurement. The experiment measured an energy loss of $dE = (29 \pm 6)$ keV with an uncertainty of 21 % for protons. Theoretical models (refer to Section 4) anticipate that the protons will lose approximately 70–100 keV in the plasma targeted for the planned experiment ($E = 2 \times 30$ J, $\lambda = 527$ nm, $\tau = 7$ ns (FWHM), $d = 1$ mm). The expected reduction in uncertainty is approximately 5 keV due to the longer flight time. The resulting uncertainty for 70 keV is 7 %. For C^{4+}, an energy loss of $dE = (61 \pm 10)$ keV/u was recorded, resulting in an expected uncertainty of 6 % in the stopping power measurement with a plasma.

These energy resolutions are adequate for distinguishing between the stopping power models presented in Chapter 2 and utilized to forecast the energy loss of protons and carbon ions in Chapter 4. Only the Li-Petrasso and RPA models require a higher resolution for protons of 6 %. According to previous experiments (W. Cayzac et al. 2017; Frenje et al. 2019), the stopping power is expected to be best represented by the T-Matrix with $\lambda(v)$ model. In this case, a resolution of 11 % is sufficient to eliminate all other stopping theories.

Some of the findings presented in this chapter have been published in Nazary et al. 2024.

6 Summary and Outlook

6.1 Summary

The objective of this thesis was to conduct a stopping power experiment with the LIGHT beamline. A detailed model of the planned experiment was developed to demonstrate its feasibility and define the requirements. The generation of the required ion beams and the measurement of their energy losses in a cold foil were successfully demonstrated.

The stopping power experiments I planned will use a carbon ion (C^{4+}) beam and a proton beam with an energy-to-mass ratio of 0.6 MeV/u selected and transported by the LIGHT beamline (refer to Chapter 3). The ions will be accelerated with the PHELIX laser and transported with two solenoids. The projectile bunches will be temporally compressed with an RF cavity to the shortest possible bunch length, in order to probe the transient plasma with as precisely defined parameters as possible. A new and upgraded version of the nhelix laser was designed and constructed in the scope of this work for the generation of the plasma target. The nhelix laser will irradiate a carbon foil with an areal density of 100 µg/cm^2 from both sides with an energy of 30 J each. The pulse length is 7 ns and the wavelength is 527 nm. The resulting plasma is designed to have a free electron density of 3×10^{20} cm^{-3} and a temperature of 180 eV. This configuration ensures that the projectile velocity is close to the thermal velocity of the plasma electrons ($v_{\mathrm{p}} \approx v_{\mathrm{th}}$). In this regime, the stopping maximum is located, and stopping theories show the highest discrepancies. The laser-generated plasma is diagnosed with an interferometric measurement of the free electron density. The development, construction, and successful testing of the interferometric setup were overseen by me throughout this work.

I modeled the planned stopping power experiment in great detail (refer to Chapter 4). Beamline simulations were conducted to predict the resulting beam characteristics and requisite beamline settings. I modeled the transport and temporal compression of 7.2 MeV carbon ions and 0.6 MeV protons. The final simulated bunches showed a temporal bunch width of 300–340 ps and a focal spot size of 4.5–5.5 mm at the plasma target. I used the hydrodynamic code MULTI2D to model the plasma and the non-LTE FLYCHK code to determine the charge state of the plasma ions. These simulations allowed me to study the plasma expansion, identify the homogeneous region of the plasma, and confirm the required laser parameters. The plasma reaches a maximum temperature of 180 eV and a free electron density on the order of 10^{20} cm^{-3} after 7.75 ns. Here, the plasma is longitudinally homogeneous. In the innermost region, where the projectile beam passes through the plasma, transverse homogeneity is achieved after 8 ns. In the final step, the interaction of the ion beam with the plasma target was modeled according to different theoretical models describing the stopping power. A comprehensive two-dimensional simulation of the experiment was successfully conducted. In the stopping maximum, the stopping power models predict an increased energy loss of 185–230 % for protons and 230–290 % for carbon ions compared to the energy loss in a solid target. The two-dimensional simulations were employed to identify the optimal pinhole size for the projectile beam in the stopping power experiments, resulting in a diameter of 0.5 mm. The results of the stopping power

simulations with the different models indicated that a required energy resolution of 11 % would enable the discrimination of the different stopping power models and facilitate the acquisition of meaningful results. With an energy resolution of 14 %, the results of the BPS and T-Matrix model can be distinguished from the other theories. Based on previous experiments with similar properties, it is anticipated that the T-Matrix and BPS models will provide the most accurate description for this experiment.

I performed a series of beamtimes in preparation for the planned stopping power experiments in plasma with the LIGHT beamline (refer to Chapter 5). In these experiments, the optimal target setups for both carbon ions and protons were established. For protons, the use of plastic targets on plastic holders resulted in the least amount of electromagnetic pulse (EMP) during the target normal sheath acceleration (TNSA) process. Conversely, for carbon ions, the use of ohmically heated targets was found to be optimal in order to maximize the number of accelerated carbon ions. During these beamtimes, the low efficiency of the diamond detectors for low-energy particles was identified. However, it was still possible to demonstrate the transportation of the desired beam. The capability of the beamline to generate the required ion beams was demonstrated. Carbon ions (C^{4+}) with an **energy of (7.2 ± 0.2) MeV** were successfully transported and temporally compressed to a **bunch duration of (1.23 ± 0.04) ns (FWHM)**. The **focal spot size was (4.11 ± 0.02) mm** in diameter, and the compressed bunch was estimated to contain **(2.0 ± 0.6) × 10^8 ions**. Additionally, protons with an **energy of (0.63 ± 0.01) MeV** were transported and temporally compressed to a **bunch duration of (0.76 ± 0.04) ns**. The **focal spot size was (2.82 ± 0.03) mm** in diameter, and the bunch was estimated to contain **(5.9 ± 0.4) × 10^8 protons**. The measured bunch durations for protons and carbon ions were found to be longer than the simulated ones. Several potential causes were investigated, including the saturation effects of the diamond detector. However, none of these could explain the discrepancy. The most probable cause was identified as the underestimation of longitudinal emittance growth by the solenoids in the beamline simulation. The achieved projectile beams are still **five to seven times shorter** than the projectile beams used in previous experiments using linear accelerators. This reduces the time averaging over the changing plasma parameters, which change on a nanosecond timescale, during the passing of the projectile bunch. Additionally, the particle numbers of the beam are estimated to be **two to three orders of magnitude higher** than in similar experiments, which allows for a higher ToF distance and therefore a higher energy resolution. The transported beams were used to conduct stopping power experiments in a solid carbon foil, to demonstrate the feasibility of the planned experiment. The energy loss for protons was measured to be $dE = $ **(29 ± 6) keV**, while for carbon ions, the energy loss was $dE = $ **(61 ± 10) keV**. These results align with the energy losses predicted by SRIM. With these measurements, an **uncertainty of 7 % for protons and 6 % for carbon ions** is predicted for the stopping power experiments with the plasma target. This will lead to meaningful data for benchmarking stopping power theories. These preliminary experiments demonstrate the viability of the proposed stopping power experiment.

6.2 Outlook

This section outlines the future directions of research in plasma physics with regard to stopping power. It builds on the findings of this thesis and highlights upcoming experiments and the potential for advancing both experimental and theoretical frameworks. It thus sets the stage for further contributions to the field and its applications.

The next step is to conduct the planned stopping power experiment with a plasma target. This experiment will allow for benchmarking of theories in the regime of the stopping maximum with higher accuracy than in previous stopping power experiments performed at GSI.

Future stopping power experiments should aim to reduce uncertainties in ion stopping measurements. While the main uncertainties in energy loss measurements originate from temporal diagnostics (accounting for approximately 80–96 % of the total uncertainty, as outlined in Section 5.4), the most effective method for reducing this uncertainty is to increase the time of flight distance. As the time of flight increases, the contribution of each uncertainty decreases. There are numerous ways to increase the time of flight distance. A larger stop detector could be employed to capture a greater number of ions from the divergent beam at greater distances. An increased number of projectile ions would also enable a high enough signal at a greater time of flight distance. This could be achieved by increasing the energy of the PHELIX laser or by optimizing the TNSA mechanism by optimizing the target. Additionally, a third solenoid could be used to collimate the beam after passing through the plasma. This approach generates a collimated beam, which enables the detector to detect a sufficient number of ions at greater distances. Besides increasing the time of flight distance, future experiments will also aim to optimize the time of flight diagnostics.

The improvement of the modeling of the experiment will facilitate the benchmarking of the different ion stopping models. In order to obtain more meaningful results, it is necessary to measure and compare the energy spread of the generated ions with the beamline simulations. Furthermore, it is essential to investigate the cause of the discrepancies between the simulated and measured temporal bunch width. The understanding of this issue could contribute to a reduction of the bunch width, thus decreasing the temporal averaging over the plasma parameters. The modeling could be further enhanced by the development of advanced plasma diagnostics for the accurate measurement of plasma parameters that affect ion stopping. For instance, the incorporation of an X-ray spectrometer for the measurement of plasma temperature would enable the benchmarking of the simulated plasma temperature in addition to the benchmarking of the free electron density. This would facilitate more precise modeling of stopping power experiments.

Expanding experiments to include a wider range of plasma densities, temperatures, and ion species can enhance the understanding of ion stopping phenomena. This can be achieved by using various target materials and laser parameters to generate plasmas that closely resemble conditions found in stellar environments or future fusion reactors.

Understanding ion stopping in plasmas is crucial for optimizing designs for both inertial confinement fusion (ICF) and magnetic confinement fusion (MCF). Future research could concentrate on applying improved ion stopping models to increase the efficiency of energy deposition in fusion plasmas, which could potentially enhance the net energy gain in future fusion reactors.

Additionally, the study of ion stopping power is relevant to astrophysical processes, including interactions with stellar winds and the propagation of cosmic rays. Advanced theoretical and experimental insights into ion stopping could contribute to more accurate models of stellar atmospheres, interstellar medium dynamics, and the behavior of cosmic rays.

The LIGHT beamline is a noteworthy technological advancement in ion acceleration and beam manipulation. Future developments could focus on improving beam quality, increasing ion energies, and reducing bunch durations. Upgrading the PHELIX laser at the Z6 experimental facility will expand the parameter space of the ion beams generated with the LIGHT beamline. A higher repetition rate would enhance the LIGHT beamline and increase its usefulness in most applications. This will not only benefit studies on ion stopping power but also expand the use of laser-driven ion sources in medical physics, materials science, and radiation therapy. One current investigation concerns the generation of an ion beam with the LIGHT beamline, which will be injected into the heavy ion synchrotron SIS18 of GSI. The injection of a laser-generated ion beam into a synchrotron would represent a significant advancement for the laser-plasma accelerator community.

The upcoming stopping power experiment will be the first of many utilizing the infrastructure and platform at the experimental area Z6 at GSI. The LIGHT beamline can cover a wide range of parameters for stopping power experiments by using various configurations of different targets, plasma parameters, and ion beams. These experiments aim to enhance our understanding of ion stopping in plasma and the validity of different stopping power models in various regimes. With an increase in experimental data, new advanced theoretical models, approaches, and corrections are likely to emerge.

This thesis research has established a fundamental understanding of ion stopping in plasma, emphasizing the importance of theoretical models, experimental accuracy, and the impact of plasma parameters. The future of research in plasma physics looks promising, with potential breakthroughs in theoretical modeling, experimental methodologies, applications in fusion and astrophysics, and technological advancements. As the field progresses, it will continue to play a pivotal role in the advancement of plasma physics, fusion energy research, and our understanding of the universe.

Bibliography

Abu-Shawareb, H. et al. (Feb. 2024). "Achievement of Target Gain Larger than Unity in an Inertial Fusion Experiment". In: *Physical Review Letters* 132.6, p. 065102. ISSN: 0031-9007. DOI: 10.1103/PhysRevLett.132.065102.

Allen, Michael P. and Dominic J. Tildesley (June 2017). *Computer Simulation of Liquids*. Oxford University PressOxford, pp. 1–626. ISBN: 0198803192. DOI: 10.1093/oso/9780198803195.001.0001.

Alton, G D, R A Sparrow, and R E Olson (Apr. 1992). "Plasma as a high-charge-state projectile stripping medium". In: *Physical Review A* 45.8, pp. 5957–5963. ISSN: 1050-2947. DOI: 10.1103/PhysRevA.45.5957.

Apiñaniz, J. I. et al. (Mar. 2021). "A quasi-monoenergetic short time duration compact proton source for probing high energy density states of matter". In: *Scientific Reports* 11.1, p. 6881. ISSN: 2045-2322. DOI: 10.1038/s41598-021-86234-x.

Atzeni, Stefano and Jürgen Meyer-ter-Vehn (June 2004). *The Physics of Inertial Fusion*. Oxford University Press. ISBN: 9780198562641. DOI: 10.1093/acprof:oso/9780198562641.001.0001.

Bagnoud, V. et al. (July 2010). "Commissioning and early experiments of the PHELIX facility". In: *Applied Physics B* 100.1, pp. 137–150. ISSN: 0946-2171. DOI: 10.1007/s00340-009-3855-7.

Balescu, R. (Jan. 1960). "Irreversible Processes in Ionized Gases". In: *The Physics of Fluids* 3.1, pp. 52–63. ISSN: 0031-9171. DOI: 10.1063/1.1706002.

Barkas, Walter H, John N Dyer, and Harry H Heckman (July 1963). "Resolution of the $\Sigma-$-Mass Anomaly". In: *Physical Review Letters* 11.1, pp. 26–28. ISSN: 0031-9007. DOI: 10.1103/PhysRevLett.11.26.

Barriga-Carrasco, Manuel D. (June 2010). "Full conserving dielectric function for plasmas at any degeneracy". In: *Laser and Particle Beams* 28.2, pp. 307–311. ISSN: 0263-0346. DOI: 10.1017/S0263034610000212.

Barriga-Carrasco, Manuel D. and Gilles Maynard (June 2005). "A 3D trajectory numerical simulation of the transport of energetic light ion beams in plasma targets". In: *Laser and Particle Beams* 23.2, pp. 211–217. ISSN: 0263-0346. DOI: 10.1017/S0263034605040097.

BAUER, D. (Oct. 2003). "Plasma formation through field ionization in intense laser–matter interaction". In: *Laser and Particle Beams* 21.4, pp. 489–495. ISSN: 0263-0346. DOI: 10.1017/S0263034603214026.

Belyaev, G. et al. (Mar. 1996). "Measurement of the Coulomb energy loss by fast protons in a plasma target". In: *Physical Review E* 53.3, pp. 2701–2707. ISSN: 1063-651X. DOI: 10.1103/PhysRevE.53.2701.

Berdermann, E et al. (May 2010). "Diamond detectors for hadron physics research". In: *Diamond and Related Materials* 19.5-6, pp. 358–367. ISSN: 09259635. DOI: 10.1016/j.diamond.2009.11.019.

Bethe, H. (Jan. 1930). "Zur Theorie des Durchgangs schneller Korpuskularstrahlen durch Materie". In: *Annalen der Physik* 397.3, pp. 325–400. ISSN: 0003-3804. DOI: 10.1002/andp.19303970303.

– (May 1932). "Bremsformel für Elektronen relativistischer Geschwindigkeit". In: *Zeitschrift für Physik* 76.5-6, pp. 293–299. ISSN: 1434-6001. DOI: 10.1007/BF01342532.

Bimbot, R. et al. (June 2005). "STOPPING OF IONS HEAVIER THAN HELIUM". In: *Journal of the International Commission on Radiation Units and Measurements* 5.1, p. 1. ISSN: 1742-3422. DOI: 10.1093/jicru/ndi001.

Bloch, F. (Jan. 1933). "Zur Bremsung rasch bewegter Teilchen beim Durchgang durch Materie". In: *Annalen der Physik* 408.3, pp. 285–320. ISSN: 0003-3804. DOI: `10.1002/andp.19334080303`.

Bohr, Niels (Jan. 1913). "II. On the theory of the decrease of velocity of moving electrified particles on passing through matter". In: *The London, Edinburgh, and Dublin Philosophical Magazine and Journal of Science*. Niels Bohr Collected Works 25.145. Ed. by Jens Thorsen, pp. 10–31. ISSN: 1941-5982. DOI: `10.1080/14786440108634305`.

Boine-Frankenheim, O. (May 1996). "Nonlinear stopping power of ions in plasmas". In: *Physics of Plasmas* 3.5, pp. 1585–1590. ISSN: 1070-664X. DOI: `10.1063/1.872017`.

Brack, Florian-Emanuel (Aug. 2022). "Dose formation using a pulsed high-field solenoid beamline for radiobiological in vivo studies at a laser-driven proton source". PhD thesis. Dresden: Technische Universität Dresden. URL: `https://nbn-resolving.org/urn:nbn:de:bsz:14-qucosa2-803750`.

Brack, Florian-Emanuel et al. (June 2020). "Spectral and spatial shaping of laser-driven proton beams using a pulsed high-field magnet beamline". In: *Scientific Reports* 10.1, p. 9118. ISSN: 2045-2322. DOI: `10.1038/s41598-020-65775-7`.

BROWN, L, D PRESTON, and R SINGLETONJR (May 2005). "Charged particle motion in a highly ionized plasma". In: *Physics Reports* 410.4, pp. 237–333. ISSN: 03701573. DOI: `10.1016/j.physrep.2005.01.001`.

Busold, S. et al. (Oct. 2013). "Focusing and transport of high-intensity multi-MeV proton bunches from a compact laser-driven source". In: *Physical Review Special Topics - Accelerators and Beams* 16.10, p. 101302. ISSN: 1098-4402. DOI: `10.1103/PhysRevSTAB.16.101302`.

Busold, S. et al. (Mar. 2014a). "Commissioning of a compact laser-based proton beam line for high intensity bunches around 10 MeV". In: *Physical Review Special Topics - Accelerators and Beams* 17.3, p. 031302. ISSN: 1098-4402. DOI: `10.1103/PhysRevSTAB.17.031302`.

Busold, S. et al. (Mar. 2014b). "Shaping laser accelerated ions for future applications – The LIGHT collaboration". In: *Nuclear Instruments and Methods in Physics Research Section A: Accelerators, Spectrometers, Detectors and Associated Equipment* 740, pp. 94–98. ISSN: 01689002. DOI: `10.1016/j.nima.2013.10.025`.

Busold, Simon (2014). "Construction and characterization of a laser-driven proton beamline at GSI". PhD thesis. Darmstadt: Technische Universität Darmstadt. URL: `http://tuprints.ulb.tu-darmstadt.de/3932/`.

Busold, Simon et al. (July 2015). "Towards highest peak intensities for ultra-short MeV-range ion bunches". In: *Scientific Reports* 5.1, p. 12459. ISSN: 2045-2322. DOI: `10.1038/srep12459`.

Callahan-Miller, Debra A. and Max Tabak (May 2000). "Progress in target physics and design for heavy ion fusion". In: *Physics of Plasmas* 7.5, pp. 2083–2091. ISSN: 1070-664X. DOI: `10.1063/1.874031`.

Casas, David, Manuel D. Barriga-Carrasco, and Juan Rubio (Sept. 2013). "Evaluation of slowing down of proton and deuteron beams in CH$_2$, LiH, and Al partially ionized plasmas". In: *Physical Review E* 88.3, p. 033102. ISSN: 1539-3755. DOI: `10.1103/PhysRevE.88.033102`.

Cayzac, W. et al. (Nov. 2015). "Predictions for the energy loss of light ions in laser-generated plasmas at low and medium velocities". In: *Physical Review E* 92.5, p. 053109. ISSN: 1539-3755. DOI: `10.1103/PhysRevE.92.053109`.

Cayzac, W. et al. (June 2017). "Experimental discrimination of ion stopping models near the Bragg peak in highly ionized matter". In: *Nature Communications* 8.1, p. 15693. ISSN: 2041-1723. DOI: `10.1038/ncomms15693`.

Cayzac, Witold et al. (Apr. 2013). "A spectrometer on chemical vapour deposition-diamond basis for the measurement of the charge-state distribution of heavy ions in a laser-generated plasma". In: *Review of Scientific Instruments* 84.4, p. 043301. ISSN: 0034-6748. DOI: `10.1063/1.4798539`.

Chen, S. N. et al. (Oct. 2018). "Experimental evidence for the enhanced and reduced stopping regimes for protons propagating through hot plasmas". In: *Scientific Reports* 8.1, p. 14586. ISSN: 2045-2322. DOI: `10.1038/s41598-018-32726-2`.

Chen, Y-J (Apr. 2003). *Final Focus Spot Size in a Solenoid Focusing System*. Tech. rep. Livermore, CA: Lawrence Livermore National Laboratory (LLNL). DOI: `10.2172/15003857`.

Chiadroni, E et al. (2018). "Overview of plasma lens experiments and recent results at SPARC_LAB". In: *Nuclear Instruments and Methods in Physics Research Section A: Accelerators, Spectrometers, Detectors and Associated Equipment* 909, pp. 16–20. ISSN: 0168-9002. DOI: `https://doi.org/10.1016/j.nima.2018.02.014`.

Chung, H.-K. et al. (Dec. 2005). "FLYCHK: Generalized population kinetics and spectral model for rapid spectroscopic analysis for all elements". In: *High Energy Density Physics* 1.1, pp. 3–12. ISSN: 15741818. DOI: `10.1016/j.hedp.2005.07.001`.

Couillaud, C. et al. (Feb. 1994). "Ionization and stopping of heavy ions in dense laser-ablated plasmas". In: *Physical Review E* 49.2, pp. 1545–1562. ISSN: 1063-651X. DOI: `10.1103/PhysRevE.49.1545`.

Cowan, T. E. et al. (May 2004). "Ultralow Emittance, Multi-MeV Proton Beams from a Laser Virtual-Cathode Plasma Accelerator". In: *Physical Review Letters* 92.20, p. 204801. ISSN: 0031-9007. DOI: `10.1103/PhysRevLett.92.204801`.

D'Avanzo, J., I. Hofmann, and M. Lontano (Oct. 1998). "Charge dependence of nonlinear stopping power". In: *Nuclear Instruments and Methods in Physics Research Section A: Accelerators, Spectrometers, Detectors and Associated Equipment* 415.3, pp. 632–636. ISSN: 01689002. DOI: `10.1016/S0168-9002(98)00437-9`.

Deutsch, C et al. (2010). "Ion Stopping in Dense Plasma Target for High Energy Density Physics". In: *The Open Plasma Physics Journal* 3, pp. 88–115. URL: `https://benthamopen.com/ABSTRACT/TOPPJ-3-88`.

Dietrich, K-G et al. (Dec. 1990). "Energy loss of heavy ions in a dense hydrogen plasma". In: *Zeitschrift für Physik D Atoms, Molecules and Clusters* 16.4, pp. 229–230. ISSN: 0178-7683. DOI: `10.1007/BF01437524`.

Dietrich, K.-G. et al. (Dec. 1992). "Charge state of fast heavy ions in a hydrogen plasma". In: *Physical Review Letters* 69.25, pp. 3623–3626. ISSN: 0031-9007. DOI: `10.1103/PhysRevLett.69.3623`.

Ding, Johannes (2018). "Generation, Handling and Transport of Laser-Driven Heavy Ion Beams". PhD thesis. Technische Universität Darmstadt. URL: `http://tuprints.ulb.tu-darmstadt.de/8214/`.

Drake, R. Paul (2006). *High-Energy-Density Physics*. Ed. by Lee Davison and Yasuyuki Horie. Shock Wave and High Pressure Phenomena. Springer Berlin Heidelberg. ISBN: 978-3-540-29314-9. DOI: `10.1007/3-540-29315-9`.

Dromey, B. et al. (Feb. 2016). "Picosecond metrology of laser-driven proton bursts". In: *Nature Communications* 7.1, p. 10642. ISSN: 2041-1723. DOI: `10.1038/ncomms10642`.

Edie, D.J. et al. (Nov. 2013). "α -particle stopping and electron-ion energy relaxation in highly compressed ICF fuel". In: *EPJ Web of Conferences* 59. Ed. by P. Mora, K. A. Tanaka, and E. Moses, p. 05018. ISSN: 2100-014X. DOI: `10.1051/epjconf/20135905018`.

Edwards, D. A. and M. J. Syphers (Jan. 1993). *An Introduction to the Physics of High Energy Accelerators*. Wiley. ISBN: 9780471551638. DOI: `10.1002/9783527617272`.

Fast Timing BC-418, BC-420, BC-422, BC-422Q | Luxium Solutions (2024). URL: `https://www.luxiumsolutions.com/radiation-detection-scintillators/plastic-scintillators/fast-timing-bc-418-bc-420-bc-422-bc-422q` (visited on 04/12/2024).

Fernández, J.C. et al. (May 2014). "Fast ignition with laser-driven proton and ion beams". In: *Nuclear Fusion* 54.5, p. 054006. ISSN: 0029-5515. DOI: `10.1088/0029-5515/54/5/054006`.

Ferrari, Attilio (Sept. 1998). "MODELING EXTRAGALACTIC JETS". In: *Annual Review of Astronomy and Astrophysics* 36.1, pp. 539–598. ISSN: 0066-4146. DOI: `10.1146/annurev.astro.36.1.539`.

Flierl, H.-P et al. (Oct. 1998). "The energy loss of alpha particles traversing a hydrogen plasma". In: *Nuclear Instruments and Methods in Physics Research Section A: Accelerators, Spectrometers, Detectors and Associated Equipment* 415.3, pp. 637–641. ISSN: 01689002. DOI: `10.1016/S0168-9002(98)00438-0`.

Frank, A. et al. (Mar. 2013). "Energy Loss and Charge Transfer of Argon in a Laser-Generated Carbon Plasma". In: *Physical Review Letters* 110.11, p. 115001. ISSN: 0031-9007. DOI: `10.1103/PhysRevLett.110.115001`.

Frank, Alexander (Jan. 2012). "Energieverlust und Umladung von schweren Ionen in lasererzeugten Plasmen". PhD thesis. Darmstadt: Technische Universität Darmstadt. URL: `http://tuprints.ulb.tu-darmstadt.de/2871/`.

Frenje, J. A. et al. (Nov. 2015). "Measurements of Ion Stopping Around the Bragg Peak in High-Energy-Density Plasmas". In: *Physical Review Letters* 115.20, p. 205001. ISSN: 0031-9007. DOI: `10.1103/PhysRevLett.115.205001`.

Frenje, J. A. et al. (Jan. 2019). "Experimental Validation of Low- Z Ion-Stopping Formalisms around the Bragg Peak in High-Energy-Density Plasmas". In: *Physical Review Letters* 122.1, p. 015002. ISSN: 0031-9007. DOI: `10.1103/PhysRevLett.122.015002`.

Gafchromic™ HD-V2 films (2024). URL: `https://www.ashland.com/industries/medical/gafchromic-dosimetry-films/hdv2` (visited on 04/05/2024).

Gardes, D. et al. (Oct. 1992). "Stopping of multicharged ions in dense and fully ionized hydrogen". In: *Physical Review A* 46.8, pp. 5101–5111. ISSN: 1050-2947. DOI: `10.1103/PhysRevA.46.5101`.

Gericke, D. O. and M. Schlanges (July 1999). "Beam-plasma coupling effects on the stopping power of dense plasmas". In: *Physical Review E* 60.1, pp. 904–910. ISSN: 1063-651X. DOI: `10.1103/PhysRevE.60.904`.

– (Mar. 2003). "Energy deposition of heavy ions in the regime of strong beam-plasma correlations". In: *Physical Review E* 67.3, p. 037401. ISSN: 1063-651X. DOI: `10.1103/PhysRevE.67.037401`.

Gericke, D. O., M. Schlanges, and Th Bornath (Feb. 2002). "Stopping power of nonideal, partially ionized plasmas". In: *Physical Review E* 65.3, p. 036406. ISSN: 1063-651X. DOI: `10.1103/PhysRevE.65.036406`.

Gericke, D.O, M Schlanges, and W.D Kraeft (Nov. 1996). "Stopping power of a quantum plasma — T-matrix approximation and dynamical screening". In: *Physics Letters A* 222.4, pp. 241–245. ISSN: 03759601. DOI: `10.1016/0375-9601(96)00654-8`.

GERICKE, D.O. (July 2002). "Stopping power for strong beam–plasma coupling". In: *Laser and Particle Beams* 20.3, pp. 471–474. ISSN: 0263-0346. DOI: `10.1017/S0263034602203225`.

Gibbon, Paul (Sept. 2005). *Short Pulse Laser Interactions with Matter*. PUBLISHED BY IMPERIAL COLLEGE PRESS and DISTRIBUTED BY WORLD SCIENTIFIC PUBLISHING CO., pp. 1–312. ISBN: 978-1-86094-135-1. DOI: `10.1142/p116`.

Gould, Harvey A. and Hugh E. DeWitt (Mar. 1967). "Convergent Kinetic Equation for a Classical Plasma". In: *Physical Review* 155.1, pp. 68–74. ISSN: 0031-899X. DOI: `10.1103/PhysRev.155.68`.

Grimm, Sarah Jane (2023). "Interferometric Measurement of the Free Electron Density in a Laser-Generated Plasma for Verifying Hydro-Simulations". MA thesis. Technische Universität Darmstadt.

Gus'kov, S. Yu. et al. (Sept. 2009). "A method for calculating the effective charge of ions decelerated in a hot dense plasma". In: *Plasma Physics Reports* 35.9, pp. 709–718. ISSN: 1063-780X. DOI: `10.1134/S1063780X09090013`.

Haan, Steven W. et al. (June 1995). "Design and modeling of ignition targets for the National Ignition Facility". In: *Physics of Plasmas* 2.6, pp. 2480–2487. ISSN: 1070-664X. DOI: `10.1063/1.871209`.

Häuser, Jürgen (1989). "Eigenschaften von Spiralresonatoren". PhD thesis. Universität Frankfurt.

Hayes, A. C. et al. (Apr. 2020). "Plasma stopping-power measurements reveal transition from non-degenerate to degenerate plasmas". In: *Nature Physics* 16.4, pp. 432–437. ISSN: 1745-2473. DOI: 10.1038/s41567-020-0790-3.

Hegelich, M et al. (Aug. 2002). "MeV Ion Jets from Short-Pulse-Laser Interaction with Thin Foils". In: *Physical Review Letters* 89.8, p. 085002. ISSN: 0031-9007. DOI: 10.1103/PhysRevLett.89.085002.

Hicks, D. G. et al. (Dec. 2000). "Charged-particle acceleration and energy loss in laser-produced plasmas". In: *Physics of Plasmas* 7.12, pp. 5106–5117. ISSN: 1070-664X. DOI: 10.1063/1.1320467.

Higginson, A. et al. (Feb. 2018). "Near-100 MeV protons via a laser-driven transparency-enhanced hybrid acceleration scheme". In: *Nature Communications* 9.1, p. 724. ISSN: 2041-1723. DOI: 10.1038/s41467-018-03063-9.

Hoffmann, D. H. H. et al. (Aug. 1990). "Energy loss of heavy ions in a plasma target". In: *Physical Review A* 42.4, pp. 2313–2321. ISSN: 1050-2947. DOI: 10.1103/PhysRevA.42.2313.

Hofmann, Ingo (Jan. 2018). "Review of accelerator driven heavy ion nuclear fusion". In: *Matter and Radiation at Extremes* 3.1, pp. 1–11. ISSN: 2468-2047. DOI: 10.1016/j.mre.2017.12.001.

Humphries, S. (Dec. 1980). "Intense pulsed ion beams for fusion applications". In: *Nuclear Fusion* 20.12, pp. 1549–1612. ISSN: 0029-5515. DOI: 10.1088/0029-5515/20/12/006.

Hurricane, O. A. et al. (Feb. 2014). "Fuel gain exceeding unity in an inertially confined fusion implosion". In: *Nature* 506.7488, pp. 343–348. ISSN: 0028-0836. DOI: 10.1038/nature13008.

Hurricane, O. A. et al. (May 2019). "Approaching a burning plasma on the NIF". In: *Physics of Plasmas* 26.5. ISSN: 1070-664X. DOI: 10.1063/1.5087256.

Ikegami, Masahiro et al. (June 2009). "Radial focusing and energy compression of a laser-produced proton beam by a synchronous rf field". In: *Physical Review Special Topics - Accelerators and Beams* 12.6, p. 063501. ISSN: 10984402. DOI: 10.1103/PHYSREVSTAB.12.063501/FIGURES/4/MEDIUM.

Jacoby, J. et al. (Feb. 1995). "Stopping of Heavy Ions in a Hydrogen Plasma". In: *Physical Review Letters* 74.9, pp. 1550–1553. ISSN: 0031-9007. DOI: 10.1103/PhysRevLett.74.1550.

Jahn, D. et al. (Sept. 2018). "Chemical-vapor deposited ultra-fast diamond detectors for temporal measurements of ion bunches". In: *Review of Scientific Instruments* 89.9. ISSN: 0034-6748. DOI: 10.1063/1.5048667.

Jahn, D. et al. (Jan. 2019). "Focusing of multi-MeV, subnanosecond proton bunches from a laser-driven source". In: *Physical Review Accelerators and Beams* 22.1, p. 011301. ISSN: 2469-9888. DOI: 10.1103/PhysRevAccelBeams.22.011301.

Kim, I. Jong et al. (July 2016). "Radiation pressure acceleration of protons to 93 MeV with circularly polarized petawatt laser pulses". In: *Physics of Plasmas* 23.7. ISSN: 1070-664X. DOI: 10.1063/1.4958654.

Kreussler, S., C. Varelas, and Werner Brandt (Jan. 1981). "Target dependence of effective projectile charge in stopping powers". In: *Physical Review B* 23.1, pp. 82–84. ISSN: 0163-1829. DOI: 10.1103/PhysRevB.23.82.

Kroll, Florian (Jan. 2019). "The study and development of pulsed high-field magnets for application in laser-plasma physics". PhD thesis. Technische Universität Dresden. URL: https://nbn-resolving.org/urn:nbn:de:bsz:d120-qucosa2-322841.

Kroll, Florian et al. (Mar. 2022). "Tumour irradiation in mice with a laser-accelerated proton beam". In: *Nature Physics* 18.3, pp. 316–322. ISSN: 1745-2473. DOI: 10.1038/s41567-022-01520-3.

Kumar, Vinit (Aug. 2009). "Understanding the focusing of charged particle beams in a solenoid magnetic field". In: *American Journal of Physics* 77.8, pp. 737–741. ISSN: 0002-9505. DOI: 10.1119/1.3129242.

Lahmann, B. et al. (Sept. 2023). "Measuring stopping power in warm dense matter plasmas at OMEGA". In: *Plasma Physics and Controlled Fusion* 65.9, p. 095002. ISSN: 0741-3335. DOI: 10.1088/1361-6587/ace4f2.

Lamour, E. et al. (Oct. 2015). "Extension of charge-state-distribution calculations for ion-solid collisions towards low velocities and many-electron ions". In: *Physical Review A* 92.4, p. 042703. ISSN: 1050-2947. DOI: 10.1103/PhysRevA.92.042703.

Lenard, Andrew (July 1960). "On Bogoliubov's kinetic equation for a spatially homogeneous plasma". In: *Annals of Physics* 10.3, pp. 390–400. ISSN: 00034916. DOI: 10.1016/0003-4916(60)90003-8.

Li, Chi-Kang and Richard D Petrasso (May 1993a). "Charged-particle stopping powers in inertial confinement fusion plasmas". In: *Physical Review Letters* 70.20, pp. 3059–3062. ISSN: 0031-9007. DOI: 10.1103/PhysRevLett.70.3059.

– (May 1993b). "Fokker-Planck equation for moderately coupled plasmas". In: *Physical Review Letters* 70.20, pp. 3063–3066. ISSN: 0031-9007. DOI: 10.1103/PhysRevLett.70.3063.

Lindhard, J. and M. Scharff (Oct. 1961). "Energy Dissipation by Ions in the kev Region". In: *Physical Review* 124.1, pp. 128–130. ISSN: 0031-899X. DOI: 10.1103/PhysRev.124.128.

Lindhard, Jens (Jan. 1976). "The Barkas effect - or Z13, Z14-corrections to stopping of swift charged particles". In: *Nuclear Instruments and Methods* 132.C, pp. 1–5. ISSN: 0029554X. DOI: 10.1016/0029-554X(76)90702-3.

Lindl, John (Nov. 1995). "Development of the indirect-drive approach to inertial confinement fusion and the target physics basis for ignition and gain". In: *Physics of Plasmas* 2.11, pp. 3933–4024. ISSN: 1070-664X. DOI: 10.1063/1.871025.

Loisch, G. et al. (May 2015). "Hydrogen plasma dynamics in the spherical theta pinch plasma target for heavy ion stripping". In: *Physics of Plasmas* 22.5, p. 053502. ISSN: 1070-664X. DOI: 10.1063/1.4919851.

Macchi, Andrea (2013). *A Superintense Laser-Plasma Interaction Theory Primer*. SpringerBriefs in Physics. Dordrecht: Springer Netherlands. ISBN: 978-94-007-6124-7. DOI: 10.1007/978-94-007-6125-4.

Mal, K. et al. (Dec. 2022). "Study and improvements of a radially coupled coaxial Fast Faraday cup design toward lower intensity beams". In: *AIP Advances* 12.12, p. 125223. ISSN: 2158-3226. DOI: 10.1063/5.0131890.

Malko, Sophia et al. (May 2022). "Proton stopping measurements at low velocity in warm dense carbon". In: *Nature Communications* 13.1, p. 2893. ISSN: 2041-1723. DOI: 10.1038/s41467-022-30472-8.

Maynard, G. and C. Deutsch (1985). "Born random phase approximation for ion stopping in an arbitrarily degenerate electron fluid". In: *Journal de Physique* 46.7, pp. 1113–1122. ISSN: 0302-0738. DOI: 10.1051/jphys:0198500460701113000.

Maynard, Gilles, Marin Chabot, and Daniel Gardès (Apr. 2000). "Density effect and charge dependent stopping theories for heavy ions in the intermediate velocity regime". In: *Nuclear Instruments and Methods in Physics Research Section B: Beam Interactions with Materials and Atoms* 164-165, pp. 139–146. ISSN: 0168583X. DOI: 10.1016/S0168-583X(99)01006-X.

Maynard, Gilles et al. (Apr. 2001). "Diffusion-transport cross section and stopping power of swift heavy ions". In: *Physical Review A* 63.5, p. 052903. ISSN: 1050-2947. DOI: 10.1103/PhysRevA.63.052903.

McKenna, Paul et al. (Jan. 2013). *Laser-Plasma Interactions and Applications*. Ed. by Paul McKenna et al. Scottish Graduate Series. Heidelberg: Springer International Publishing, pp. 1–471. ISBN: 978-3-319-00037-4. DOI: 10.1007/978-3-319-00038-1.

McLaughlin, William L. et al. (May 1996). "Radiochromic Solid-State Polymerization Reaction". In: *ACS Symposium Series*. Vol. 620, pp. 152–166. DOI: 10.1021/bk-1996-0620.ch011.

Metternich, Martin (2023). "Shaping of laser-accelerated ion beams for applications in high energy density physics". PhD thesis. Darmstadt: Technische Universität Darmstadt. DOI: https://doi.org/10.26083/tuprints-00024395.

Metternich, Martin et al. (Nov. 2022). "Analyzing the filamentation of MeV-range proton bunches in a laser-driven ion beamline and optimizing their peak intensity". In: *Physical Review Accelerators and Beams* 25.11, p. 111301. ISSN: 2469-9888. DOI: 10.1103/PhysRevAccelBeams.25.111301.

Miller, George H, Edward I Moses, and Craig R Wuest (Dec. 2004). "The National Ignition Facility: enabling fusion ignition for the 21st century". In: *Nuclear Fusion* 44.12, S228–S238. ISSN: 0029-5515. DOI: 10.1088/0029-5515/44/12/S14.

Morales, Roberto (Sept. 2022). "Comparing different charge-state models with experimental data of ion beams penetrating fully and partially ionized plasmas". In: *Physics of Plasmas* 29.9. ISSN: 1070-664X. DOI: 10.1063/5.0107331.

Morawetz, K. and G. Röpke (Oct. 1996). "Stopping power in nonideal and strongly coupled plasmas". In: *Physical Review E* 54.4, pp. 4134–4146. ISSN: 1063-651X. DOI: 10.1103/PhysRevE.54.4134.

Mulser, Peter and Dieter Bauer (2010). *High Power Laser-Matter Interaction*. Vol. 238. Springer Tracts in Modern Physics. Berlin, Heidelberg: Springer Berlin Heidelberg. ISBN: 978-3-540-50669-0. DOI: 10.1007/978-3-540-46065-7.

Nardi, E., Y. Maron, and D.H.H. Hoffmann (June 2009). "Dynamic screening and charge state of fast ions in plasma and solids". In: *Laser and Particle Beams* 27.2, pp. 355–361. ISSN: 0263-0346. DOI: 10.1017/S0263034609000469.

Nardi, E. and Z. Zinamon (Oct. 1982). "Charge State and Slowing of Fast Ions in a Plasma". In: *Physical Review Letters* 49.17, pp. 1251–1254. ISSN: 0031-9007. DOI: 10.1103/PhysRevLett.49.1251.

Nazary, Haress et al. (June 2024). "Towards ion stopping power experiments with the laser-driven LIGHT beamline". In: *Journal of Plasma Physics* 90.3, p. 905900302. ISSN: 0022-3778. DOI: 10.1017/S0022377824000576.

Northcliffe, L. C. (Dec. 1960). "Energy Loss and Effective Charge of Heavy Ions in Aluminum". In: *Physical Review* 120.5, pp. 1744–1757. ISSN: 0031-899X. DOI: 10.1103/PhysRev.120.1744.

NUCKOLLS, JOHN et al. (Sept. 1972). "Laser Compression of Matter to Super-High Densities: Thermonuclear (CTR) Applications". In: *Nature* 239.5368, pp. 139–142. ISSN: 0028-0836. DOI: 10.1038/239139a0.

Ortner, Alex (Sept. 2015). "Energieverlust und Ladungsverteilung von Calciumionen in dichtem, schwach gekoppeltem Kohlenstoffplasma". PhD thesis. Technische Universität Darmstadt. URL: https://tuprints.ulb.tu-darmstadt.de/id/eprint/4967.

Panofsky, W. K. H. and W. R. Baker (May 1950). "A Focusing Device for the External 350-Mev Proton Beam of the 184-Inch Cyclotron at Berkeley". In: *Review of Scientific Instruments* 21.5, pp. 445–447. ISSN: 0034-6748. DOI: 10.1063/1.1745611.

Paul, Helmut (June 2006). "A comparison of recent stopping power tables for light and medium-heavy ions with experimental data, and applications to radiotherapy dosimetry". In: *Nuclear Instruments and Methods in Physics Research Section B: Beam Interactions with Materials and Atoms* 247.2, pp. 166–172. ISSN: 0168583X. DOI: 10.1016/j.nimb.2006.01.059.

Peter, Thomas and Jürgen Meyer-ter-Vehn (Feb. 1991a). "Energy loss of heavy ions in dense plasma. I. Linear and nonlinear Vlasov theory for the stopping power". In: *Physical Review A* 43.4, pp. 1998–2014. ISSN: 1050-2947. DOI: 10.1103/PhysRevA.43.1998.

– (Feb. 1991b). "Energy loss of heavy ions in dense plasma. II. Nonequilibrium charge states and stopping powers". In: *Physical Review A* 43.4, pp. 2015–2030. ISSN: 1050-2947. DOI: 10.1103/PhysRevA.43.2015.

Piel, Alexander (2017). *Plasma Physics*. Graduate Texts in Physics. Cham: Springer International Publishing. ISBN: 978-3-319-63425-8. DOI: 10.1007/978-3-319-63427-2.

Pompili, R. et al. (Mar. 2017). "Experimental characterization of active plasma lensing for electron beams". In: *Applied Physics Letters* 110.10. ISSN: 0003-6951. DOI: 10.1063/1.4977894.

Poth, Helmut (Nov. 1990). "Electron cooling: Theory, experiment, application". In: *Physics Reports* 196.3-4, pp. 135–297. ISSN: 03701573. DOI: 10.1016/0370-1573(90)90040-9.

Ramis, R., J. Meyer-ter-Vehn, and J. Ramírez (June 2009). "MULTI2D – a computer code for two-dimensional radiation hydrodynamics". In: *Computer Physics Communications* 180.6, pp. 977–994. ISSN: 00104655. DOI: 10.1016/j.cpc.2008.12.033.

Ren, Jieru et al. (Oct. 2020). "Observation of a high degree of stopping for laser-accelerated intense proton beams in dense ionized matter". In: *Nature Communications* 11.1, p. 5157. ISSN: 2041-1723. DOI: 10.1038/s41467-020-18986-5.

Rösch, Thomas F. et al. (June 2020). "A feasibility study of zebrafish embryo irradiation with laser-accelerated protons". In: *Review of Scientific Instruments* 91.6. ISSN: 0034-6748. DOI: 10.1063/5.0008512.

Rosen, Mordecai D. (May 1999). "The physics issues that determine inertial confinement fusion target gain and driver requirements: A tutorial". In: *Physics of Plasmas* 6.5, pp. 1690–1699. ISSN: 1070-664X. DOI: 10.1063/1.873427.

Roth, M. et al. (Apr. 2000). "Energy loss of heavy ions in laser-produced plasmas". In: *Europhysics Letters (EPL)* 50.1, pp. 28–34. ISSN: 0295-5075. DOI: 10.1209/epl/i2000-00230-6.

Roth, M. et al. (Jan. 2001). "Fast Ignition by Intense Laser-Accelerated Proton Beams". In: *Physical Review Letters* 86.3, pp. 436–439. ISSN: 0031-9007. DOI: 10.1103/PhysRevLett.86.436.

Rozet, J.P., C. Stéphan, and D. Vernhet (Feb. 1996). "ETACHA: a program for calculating charge states at GANIL energies". In: *Nuclear Instruments and Methods in Physics Research Section B: Beam Interactions with Materials and Atoms* 107.1-4, pp. 67–70. ISSN: 0168583X. DOI: 10.1016/0168-583X(95)00800-4.

Saha, Megh Nad (Oct. 1920). "LIII. Ionization in the solar chromosphere". In: *The London, Edinburgh, and Dublin Philosophical Magazine and Journal of Science* 40.238, pp. 472–488. ISSN: 1941-5982. DOI: 10.1080/14786441008636148.

Sakumi, A. et al. (May 2001). "Energy dependence of the stopping power of MeV 16O ions in a laser-produced plasma". In: *Nuclear Instruments and Methods in Physics Research Section A: Accelerators, Spectrometers, Detectors and Associated Equipment* 464.1-3, pp. 231–236. ISSN: 01689002. DOI: 10.1016/S0168-9002(01)00039-0.

Schiwietz, G. and P.L Grande (Apr. 2001). "Improved charge-state formulas". In: *Nuclear Instruments and Methods in Physics Research Section B: Beam Interactions with Materials and Atoms* 175-177, pp. 125–131. ISSN: 0168583X. DOI: 10.1016/S0168-583X(00)00583-8.

Schmitz, Benedikt, Martin Metternich, and Oliver Boine-Frankenheim (Sept. 2022). "Automated reconstruction of the initial distribution of laser accelerated ion beams from radiochromic film (RCF) stacks". In: *Review of Scientific Instruments* 93.9. ISSN: 0034-6748. DOI: 10.1063/5.0094105.

Sentoku, Y and A.J. Kemp (July 2008). "Numerical methods for particle simulations at extreme densities and temperatures: Weighted particles, relativistic collisions and reduced currents". In: *Journal of Computational Physics* 227.14, pp. 6846–6861. ISSN: 00219991. DOI: 10.1016/j.jcp.2008.03.043.

SHEVELKO, Viacheslav P. et al. (Dec. 2010). "Atomic Charge-Changing Processes in Plasmas". In: *Plasma and Fusion Research* 5.0, S2012–S2012. ISSN: 1880-6821. DOI: 10.1585/pfr.5.S2012.

Shima, K. et al. (Apr. 1989). "Z oscillation of mean charges of energetic ions emerging from a carbon foil: Correlation with the shell structure of ions". In: *Physical Review A* 39.8, pp. 4316–4318. ISSN: 0556-2791. DOI: 10.1103/PhysRevA.39.4316.

Sigmund, Peter (2004). *Stopping of Heavy Ions*. Ed. by Peter Sigmund. Vol. 204. Springer Tracts in Modern Physics. Berlin, Heidelberg: Springer Berlin Heidelberg. ISBN: 978-3-540-22273-6. DOI: 10.1007/b98483.

Sigmund, Peter and Andreas Schinner (Oct. 2002). "Binary theory of electronic stopping". In: *Nuclear Instruments and Methods in Physics Research Section B: Beam Interactions with Materials and Atoms* 195.1-2, pp. 64–90. ISSN: 0168583X. DOI: 10.1016/S0168-583X(01)01162-4.

– (Dec. 2003). "Anatomy of the Barkas effect". In: *Nuclear Instruments and Methods in Physics Research Section B: Beam Interactions with Materials and Atoms* 212.1-4, pp. 110–117. ISSN: 0168583X. DOI: 10.1016/S0168-583X(03)01485-X.

Singh, R. et al. (Oct. 2021). "Comparison of Feschenko BSM and Fast Faraday Cup with Low Energy Ion Beams". In: *Proc. IBIC'21*. JACOW Publishing, Geneva, Switzerland, pp. 407–411. ISBN: 978-3-95450-230-1. DOI: 10.18429/JACOW-IBIC2021-WEPP16.

Singleton, Robert L. (May 2008). "Calculating the charged particle stopping power exactly to leading and next-to-leading order". In: *Journal of Physics: Conference Series* 112.2, p. 022034. ISSN: 1742-6596. DOI: 10.1088/1742-6596/112/2/022034.

Spitzer Jr., Lyman (1956). *Physics of Fully Ionized Gases*. Vol. 3. Interscience tracts on physics and astronomy. New York: Interscience Publishers. ISBN: 9780486449821.

Stewart, John C. and Jr. Pyatt, Kedar D. (June 1966). "Lowering of Ionization Potentials in Plasmas". In: *The Astrophysical Journal* 144, p. 1203. ISSN: 0004-637X. DOI: 10.1086/148714.

Tabak, Max et al. (May 1994). "Ignition and high gain with ultrapowerful lasers*". In: *Physics of Plasmas* 1.5, pp. 1626–1634. ISSN: 1070-664X. DOI: 10.1063/1.870664.

Tauschwitz, An. et al. (Mar. 2013). "2D radiation-hydrodynamics modeling of laser-plasma targets for ion stopping measurements". In: *High Energy Density Physics* 9.1, pp. 158–166. ISSN: 15741818. DOI: 10.1016/j.hedp.2012.12.004.

Teng, J. et al. (Nov. 2013). "Beam collimation and energy spectrum compression of laser-accelerated proton beams using solenoid field and RF cavity". In: *Nuclear Instruments and Methods in Physics Research Section A: Accelerators, Spectrometers, Detectors and Associated Equipment* 729, pp. 399–403. ISSN: 01689002. DOI: 10.1016/j.nima.2013.07.048.

Wagner, F. et al. (May 2016). "Maximum Proton Energy above 85 MeV from the Relativistic Interaction of Laser Pulses with Micrometer Thick CH_2 Targets". In: *Physical Review Letters* 116.20, p. 205002. ISSN: 0031-9007. DOI: 10.1103/PhysRevLett.116.205002.

Wamers, Felix (2006). "Entwicklung eines Detektors für gepulste Schwerionenstrahlen". Diploma thesis. Technische Universität Darmstadt.

White, A. J. and L. A. Collins (July 2020). "Fast and Universal Kohn-Sham Density Functional Theory Algorithm for Warm Dense Matter to Hot Dense Plasma". In: *Physical Review Letters* 125.5, p. 055002. ISSN: 0031-9007. DOI: 10.1103/PhysRevLett.125.055002.

Wilks, S. C. et al. (Feb. 2001). "Energetic proton generation in ultra-intense laser–solid interactions". In: *Physics of Plasmas* 8.2, pp. 542–549. ISSN: 1070-664X. DOI: 10.1063/1.1333697.

Winkler, T. et al. (Nov. 1997). "Electron cooling of highly charged ions in the ESR". In: *Nuclear Physics A* 626.1-2, pp. 485–489. ISSN: 03759474. DOI: 10.1016/S0375-9474(97)00572-1.

Yan, Yang et al. (Dec. 2023). "Design and simulation of a radius-varying active plasma lens for focusing laser-accelerated protons". In: *Nuclear Instruments and Methods in Physics Research Section A: Accelerators, Spectrometers, Detectors and Associated Equipment* 1057, p. 168737. ISSN: 01689002. DOI: 10.1016/j.nima.2023.168737.

Zaghloul, Mofreh R, Mohamed A Bourham, and J Michael Doster (Apr. 2000). "A simple formulation and solution strategy of the Saha equation for ideal and nonideal plasmas". In: *Journal of Physics D: Applied Physics* 33.8, pp. 977–984. ISSN: 0022-3727. DOI: 10.1088/0022-3727/33/8/314.

Zhu, J. G. et al. (Dec. 2020). "Demonstration of tailored energy deposition in a laser proton accelerator". In: *Physical Review Accelerators and Beams* 23.12, p. 121304. ISSN: 2469-9888. DOI: 10.1103/PhysRevAccelBeams.23.121304.

Ziegler, J. F. (Feb. 1999). "Stopping of energetic light ions in elemental matter". In: *Journal of Applied Physics* 85.3, pp. 1249–1272. ISSN: 0021-8979. DOI: 10.1063/1.369844.

Ziegler, James F. and Jochen P. Biersack (1985). "The Stopping and Range of Ions in Matter". In: *Treatise on Heavy-Ion Science*. Boston, MA: Springer US, pp. 93–129. DOI: `10.1007/978-1-4615-8103-1_3`.

Ziegler, Tim et al. (July 2024). "Laser-driven high-energy proton beams from cascaded acceleration regimes". In: *Nature Physics* 20.7, pp. 1211–1216. ISSN: 1745-2473. DOI: `10.1038/s41567-024-02505-0`.

Zimmerman, George B. (Nov. 1997). "Monte Carlo methods in ICF". In: *The 13th international conference on laser interactions and related plasma phenomena*. ASCE, pp. 23–41. ISBN: 1-56396-696-4. DOI: `10.1063/1.53528`.

Zwicknagel, G., Q. Spreiter, and C. Toepffer (1997). "Stopping of ions and local electron densities at strong coupling". In: *Hyperfine Interactions* 108.1, pp. 131–139. ISSN: 1572-9540. DOI: `https://doi.org/10.1023/A:1012690108267`.

Zwicknagel, Günter, Christian Toepffer, and Paul-Gerhard Reinhard (Feb. 1999). "Stopping of heavy ions in plasmas at strong coupling". In: *Physics Reports* 309.3, pp. 117–208. ISSN: 03701573. DOI: `10.1016/S0370-1573(98)00056-8`.

Zylstra, A B et al. (Jan. 2022a). "Burning plasma achieved in inertial fusion". In: *Nature* 601.7894, pp. 542–548. ISSN: 0028-0836. DOI: `10.1038/s41586-021-04281-w`.

Zylstra, A B et al. (Aug. 2022b). "Experimental achievement and signatures of ignition at the National Ignition Facility". In: *Physical Review E* 106.2, p. 025202. ISSN: 2470-0045. DOI: `10.1103/PhysRevE.106.025202`.

Zylstra, A. B. and O. A. Hurricane (June 2019a). "On alpha-particle transport in inertial fusion". In: *Physics of Plasmas* 26.6. ISSN: 1070-664X. DOI: `10.1063/1.5101074`.

Zylstra, A. B. et al. (May 2015). "Measurement of Charged-Particle Stopping in Warm Dense Plasma". In: *Physical Review Letters* 114.21, p. 215002. ISSN: 0031-9007. DOI: `10.1103/PhysRevLett.114.215002`.

Zylstra, A. B. et al. (Dec. 2019b). "Modified parameterization of the Li-Petrasso charged-particle stopping power theory". In: *Physics of Plasmas* 26.12. ISSN: 1070-664X. DOI: `10.1063/1.5114637`.

Zylstra, A.B. et al. (June 2020). "Platform development for dE/dx measurements on short-pulse laser facilities". In: *High Energy Density Physics* 35.August 2019, p. 100731. ISSN: 15741818. DOI: `10.1016/j.hedp.2019.100731`.

Acknowledgments

Mein besonderer Dank gilt meinem Doktorvater Prof. Markus Roth, der mich in seine Arbeitsgruppe aufnahm und mir die Chance gegeben hat, an dem spannenden LIGHT Projekt zu arbeiten.

Ebenso danke ich dem Koreferent dieser Arbeit, Prof. Vincent Bagnoud für seine Unterstützung und die wertvollen Ratschläge, die zum Gelingen dieser Arbeit beigetragen haben.

Ich bin Dennis Schumacher, Abel Blažević und Martin Metternich besonders dankbar. Ihre Bereitschaft zu ausgiebigen Diskussionen und Experimenten hat nicht nur zur wissenschaftlichen Qualität meiner Arbeit beigetragen, sondern auch viel Spaß gemacht. Natürlich bedanke ich mich auch für das mehrfache Korrekturlesen meiner Arbeit.

Ich danke Christian Brabetz, Florian Kroll, Florian Brack und Joshua Schilz. Sie haben durch ihre technische Unterstützung und Bereitstellung von Equipment einen wesentlichen Anteil am Erfolg unserer experimentellen Arbeiten.
Mein Dank gilt auch dem PHELIX Laser-Team, das stets für den Betrieb des Lasers gesorgt hat. Weiterhin danke ich Torsten Abel, Bettina Lommel und Jutta Steiner für die sorgfältige Herstellung der Targets. Ein großer Dank geht an Mladen Kis und Michael Träger, die die Diamantdetektoren mit großer Expertise gefertigt haben. Ein großer Dank geht an Rahul Singh für seine Unterstüzung mit verschiedenen Strahldiagnostiken.

Ich möchte Sarah Grimm, Finn Neufeld und Kenneth Jähner danken, die durch ihre exzellenten Master- und Bachelorarbeiten meine Lasten erleichtert haben.

Besondere Anerkennung verdienen auch Dirk Reemts und Albert Quandt für den Aufbau des nhelix Hauptverstärkers und der Pulsed-Power-Technik.

Ich danke Diana Lang, die mit ihrer organisatorischen Unterstützung alle administrativen Prozesse erleichtert hat. Ebenso bin ich meinen Bürokollegen Pascal Boller und Simon Röder für die stets gute Laune, den Spaß und die inspirierenden Diskussionen sehr dankbar.

Ein besonderer Dank gebührt auch meinen Freunden und Studienkollegen, die mich bereits seit Beginn meines Studiums begleiten. Ihre Unterstützung, sei es beim Feiern oder beim Lernen, hat mich stets motiviert und inspiriert.

Ein tief empfundener Dank gebührt meinen Eltern und Brüdern für ihre unermüdliche Unterstützung und Ermutigung in jeder Phase meines Studiums.

Zuletzt, aber nicht weniger wichtig, möchte ich meiner Freundin Laura Rumpf danken, deren tägliche Unterstützung, Ermutigung und unerschütterliche Anwesenheit an meiner Seite unverzichtbar waren.

Ihr habt alle in verschiedener Weise zu dieser Arbeit beigetragen, und dafür bin ich euch zutiefst dankbar.

Education

PhD (Physics)

Since 06/2020	**Technische Universität Darmstadt**

Thesis: Towards Ion Stopping Power Experiments with the Laser-Driven LIGHT Beamline

Publications:

- M. Metternich, H. Nazary et al. (2022): Analyzing the filamentation of MeV-range proton bunches in a laser-driven ion beamline and optimizing their peak intensity. Physical Review Accelerators and Beams, **25**(11):111301.

- H. Nazary et al. (2024): Towards stopping power experiments with LIGHT. Journal of Plasma Physics, **90**(3):905900302.

MSc (Physics)

04/2017 - 03/2020	**Technische Universität Darmstadt**

Thesis: Plasmacharakterisierung für Energieverlustmessungen mit laserbeschleunigten Ionen
Final grade: 1.57

BSc (Physics)

10/2013 - 11/2016	**Technische Universität Darmstadt**

Thesis: Konstruktion einer gepulsten Faserverstärkerstufe zur Ionenstrahlkühlung
Final grade: 2.41

Abitur (University Entrance Qualification)

06/2013	**Taunusgymnasium Königstein**

Final grade: 1.5